FINE SAND IN MOTION:
the influence of interstitial air

Tess Homan

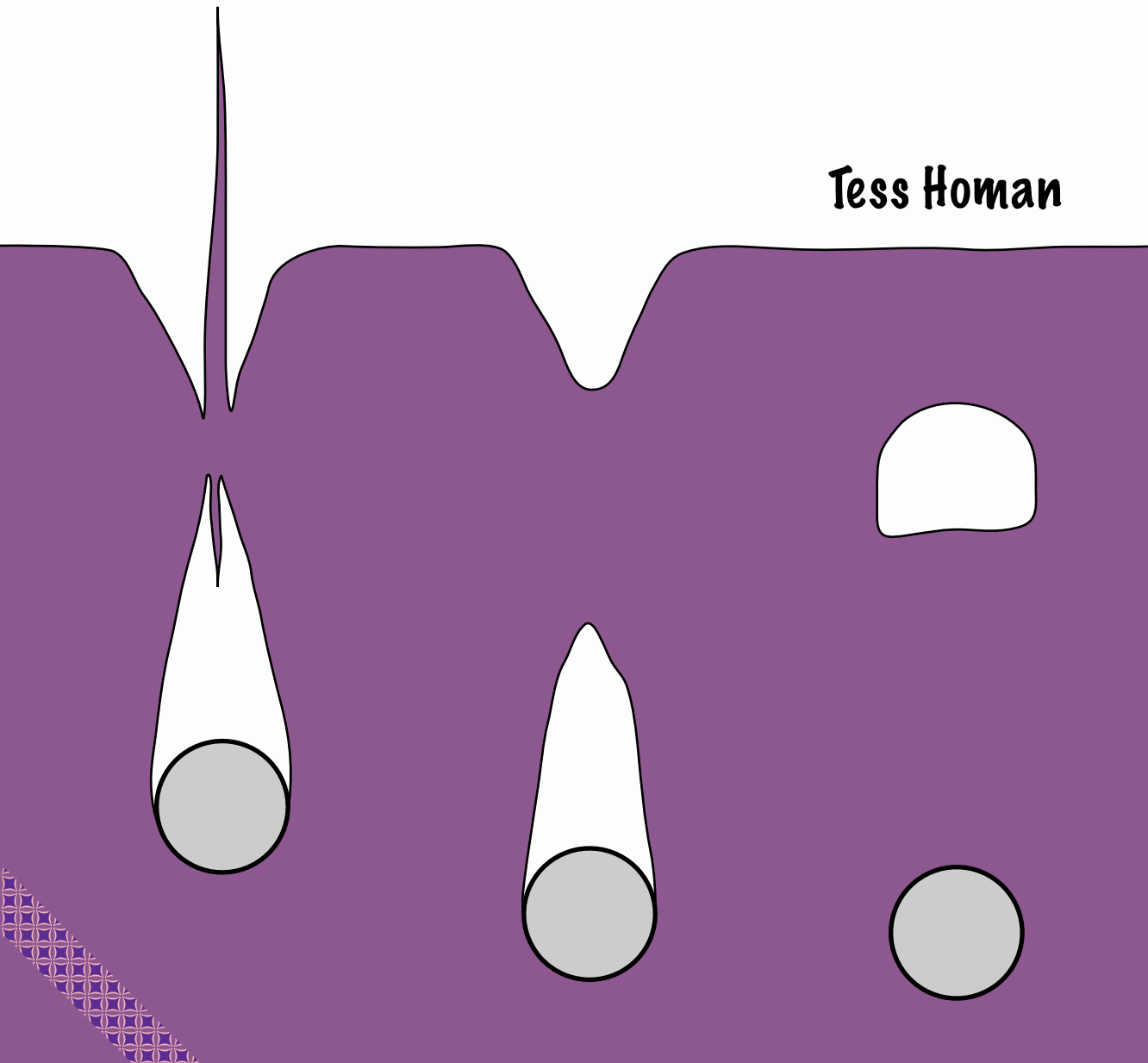

FINE SAND IN MOTION:
the influence of interstitial air

Tess Homan

Samenstelling promotiecommissie:

Prof. dr. Gerard van der Steenhoven (voorzitter)	Universiteit Twente
Prof. dr. Devaraj van der Meer (promotor)	Universiteit Twente
Prof. dr. Detlef Lohse (co-promotor)	Universiteit Twente
Prof. dr. Harold Zandvliet	Universiteit Twente
Prof. dr. Stefan Luding	Universiteit Twente
Prof. dr. Rob Mudde	Technische Universiteit Delft
Dr. Sylvain Joubaud	École normale supérieure de Lyon

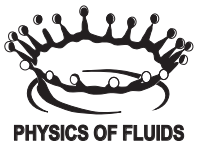

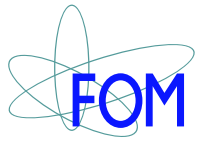

The work in this thesis was carried out at the Physics of Fluids group of the Faculty of Science and Technology of the University of Twente. It is part of the research program of the Foundation for Fundamental Research on Matter (FOM), which is financially supported by the Netherlands Organization for Scientific Research (NWO).

Nederlandse titel:
Fijn zand in beweging: De invloed van de lucht tussen de zandkorrels

Cover illustration:
Impression of a ball impacting on soft sand.

Publisher:
Tess Homan, Physics of Fluids, University of Twente,
P.O. Box 217, 7500 AE Enschede, The Netherlands
pof.tnw.utwente.nl

Print: Gildeprint Drukkerijen, Enschede

ISBN: 978-90-365-0650-2
DOI: 10.3990/1.9789036506502

FINE SAND IN MOTION:
THE INFLUENCE OF INTERSTITIAL AIR

PROEFSCHRIFT

ter verkrijging van
de graad van doctor aan de Universiteit Twente,
op gezag van de rector magnificus,
Prof. dr. H. Brinksma,
volgens besluit van het College voor Promoties
in het openbaar te verdedigen
op woensdag 25 september 2013 om 14.45 uur

door

Tessa Anne Maria Homan
geboren op 4 oktober 1986
te Oldenzaal

Dit proefschrift is goedgekeurd door de promotor:

Prof. dr. Devaraj van der Meer

en de co-promotor:

Prof. dr. rer. nat. Detlef Lohse

Sand is a granular material, and therefore it consists of individual grains arranged in a packing. The pores in-between the grains are usually filled with a fluid, in this case air. Now, is this interstitial air able to influence the behavior of the sand bed as a whole? When a ball impacts on fine, very loose sand, the interstitial air causes a pronounced change. If the bed is loose enough the ball is able to penetrate the sand and surprisingly, the final depth decreases if there is less air present in-between the grains. While the ball penetrates the bed, sand around the ball is compactified and the air in this region is compressed. Since air needs a finite amount of time to flow away it is temporarily trapped and will locally increase the pressure. If an object moves through the bed very slowly, air has ample time to move out of this compactified region and this quasi-static situation should be similar to that without air. The drag force experienced by the object for very low penetration velocities is indeed equal to the measured force at reduced ambient pressure, and much larger than the force needed to push the ball at higher velocities. The pressurized trapped air around the ball effectively reduces the drag of the sand.

Contents

1 Introduction **1**

1.1 Air and sand . . . 1
1.2 Granular matter . . . 1
1.3 Air flow around a single grain . . . 3
1.4 Influence of interstitial air . . . 5
1.5 Guide through this thesis . . . 8

2 High-speed X-ray imaging of a ball impacting on loose sand **15**

2.1 Introduction . . . 16
2.2 Experimental setup . . . 17
2.3 Cavity reconstruction . . . 18
2.4 Rising air bubble . . . 27
2.5 Local packing fraction . . . 30
2.6 Conclusion . . . 33

3 Collapsing granular beds: The role of interstitial air **39**

3.1 Introduction . . . 39
3.2 Experiment . . . 40
3.3 Model . . . 44
3.4 Conclusion . . . 47
3.5 Appendix: Derivation of the model. . . . 51

4 Air entrapment during the impact of a ball on sand **57**

4.1 Introduction . . . 57
4.2 Experimental setup . . . 59
4.3 Initial pressure change . . . 59
4.4 Equilibrium state . . . 64
4.5 Volume of trapped air . . . 65
4.6 Conclusion . . . 66

5 Long time-scale relaxations of the interstitial air in a granular bed 71
5.1 Introduction . . . 71
5.2 Experimental setup . . . 72
5.3 Constant flow . . . 74
5.4 Relaxation . . . 75
5.5 Comparison . . . 82
5.6 Conclusion . . . 88

6 Force measurements during impact with an instrumented particle 91
6.1 Introduction . . . 92
6.2 Experimental setup . . . 92
6.3 Measurement signal . . . 95
6.4 Model . . . 100
6.5 Conclusion . . . 101

7 Drag reduction due to interstitial air in a granular bed 105
7.1 Introduction . . . 105
7.2 Experimental setup . . . 107
7.3 Measurement signal . . . 107
7.4 Impact velocity . . . 112
7.5 Low ambient pressure . . . 112
7.6 Conclusion . . . 113

8 Conclusions and Outlook 117
8.1 Conclusions . . . 117
8.2 Outlook . . . 121

Summary 127

Samenvatting 129

Acknowledgements 135

About the author 139

1 Introduction

1.1 Air and sand

The interplay between air and sand is surprisingly rich. Take for example sand dunes: Huge sand dunes are formed and moved around due to transport and deposition of individual grains by the strong desert winds, see figure 1.1. Besides the large sand dunes the picture also shows beautiful smaller patterns like the sand ripples which are created by the airflow as well [1–3]. Thus, on a large scale it is very clear that air is able to influence matter like sand. Strong winds and strong airflows pick up and move grains, but at what scale does the influence of air become negligible? For what grain size or for which flow rates does air no longer have the power to influence the large scale sand bed dynamics? In this thesis we investigate situations in which we have a small airflow and we deal with interstitial air, in-between the grains, in a sand bed.

1.2 Granular matter

First we focus on the properties of sand and other granular materials. Granular materials consist of a collection of individual particles or grains. These particles are larger than 1 μm such that Brownian motion and temperature effects can be ignored. The collective behavior of granular materials are very diverse and depend

Figure 1.1: The influence of air on sand. Sand dunes formed by the wind in Death Valley with a smaller scale surface instability, sand ripples.

on properties like particle density and the amount of applied shear. Under shear the granular material starts to flow and behave almost liquid-like. Adding lots of energy to the system (for example by shaking a granular mixture) can bring the granular material into a gaseous state. But in most stationary situations granular materials closely resemble a solid [4, 5].

The difference between the behavior of granular materials in either of the three phases and their regular counterparts (ordinary solids, liquids, and gases) originate from a few core properties of the particle-particle interaction. Grains only interact when they touch, and then the forces are repulsive: There are no water-bridges as would arise in wet granular material or van der Waals interactions that would be present in very fine powders. During these collisions energy is dissipated which leads to a system that is always far from equilibrium. This, for example, results in clustering in granular flows, which is an effect not seen in normal flowing liquids [6, 7]. In denser systems the packing of the particles is crucial to the response of the system to external perturbations, and may even lead to a complete arrest of all motion known as jamming [8–18]. This packing greatly depends on the size and shapes of the individual grains, the friction in-between the grains and the method used for the formation of the packing [17, 19–31]. In such a packing the forces are transmitted along force chains to the bottom and side walls of the

container. This complex inhomogeneous distribution causes long-range variations in properties like for instance the vertical pressure profile in a granular bed, which, in contrast to a liquid, is found to saturate for depths exceeding the container diameter [32–35].

1.3 Air flow around a single grain

To understand the influence of air on sand we start by looking at the interaction between an air flow and a single grain. To investigate in which flow regime we are we first look at the Reynolds number, which gives the ratio between viscous and inertial forces:

$$Re = \frac{\rho U L}{\mu}, \tag{1.1}$$

where ρ is the density of the air, U the flow velocity, L the typical system size and μ the dynamic viscosity of air.

Most airflows in our experiments arise from pressure differences created in or over the bed. The typical velocity of the air in-between the grains of our sand bed can then be calculated using Darcy's law. Darcy's equation relates the pressure difference ΔP over a porous medium with the flow velocity in the pores and the permeability of the bed κ [36]:

$$u = -\frac{\kappa}{\mu}\frac{\Delta P}{H}, \tag{1.2}$$

where H is the thickness of the slab porous material. To calculate the permeability we may use the empirical Carman-Kozeny relation [37]

$$\kappa = \frac{d^2(1-\phi)^3}{180\phi^2}, \tag{1.3}$$

where d is the grain size and ϕ the packing fraction of the sand, defined as the fraction of the total volume that is occupied by sand. Our sand particles have a typical size of 40 μm and the packing fraction of the bed is around 0.41 which leads to a bed permeability of around $10 \cdot 10^{-12}$ m^2.

The pressure difference over the sand (a sand bed of height $H = 40$ cm) measured during the experiments is of the order of 250 Pa. Using Darcy's law, the velocity of the air in these beds is around 0.3 mm/s.

Using this velocity in equation (1.1) with the grain diameter d as the typical size we find a Reynolds number of the order of 10^{-3}. This shows that we are in

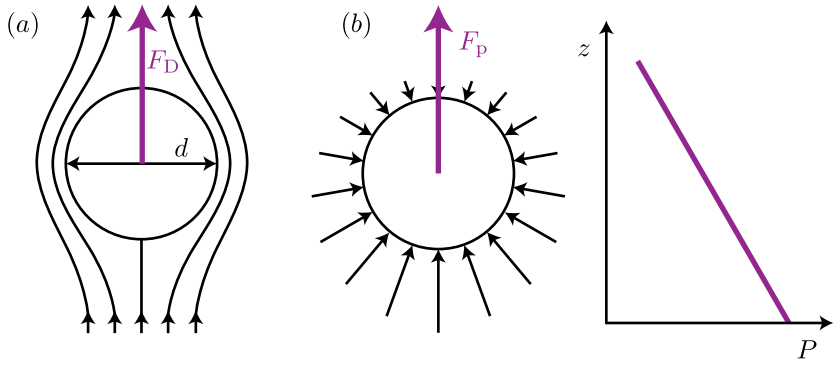

Figure 1.2: Forces acting on a single grain: (a) Flow field around a single particle, viscous effects lead to an upward Stokes drag force F_D (b) Pressure distribution on a single particle in a pressure gradient, which leads to a total upward force F_p.

the regime in which viscosity is dominant over inertial effects and the flow around the grain is laminar, confirming the applicability of Darcy's law.

One of the forces that acts on this single grain is the air drag. Since we are in a low Reynolds number regime the viscous drag is given by Stokes drag [38], see figure 1.2a

$$F_D = 3\pi\mu d u. \tag{1.4}$$

Assuming the same velocity as calculated above, the magnitude of the drag force on one grain is $\sim$4 pN.

A second mechanism by which air can have an influence on a sand grain is due to a pressure gradient, see figure 1.2b. If a pressure gradient over the sand bed is present a small (linear) pressure gradient over one grain exists. The sand bed has a height of around 10,000 grain diameters, therefore a pressure difference over the entire bed of 250 Pa gives a pressure difference of 25 mPa over 1 particle. The upward force due to this pressure difference

$$F_p = Ad\nabla P = \pi d^2 d\frac{dP}{dz} = \pi d^2 \Delta P, \tag{1.5}$$

is in this case equal to $\sim$100 pN, which is more than one order of magnitude larger than the Stokes drag force.

For the forces on the grains to actually be able to influence the movement of the particle, they must be of the order of gravity. The gravitational force on one particle is mg or

$$F_g = \frac{1}{6}\pi d^3 \rho_{\text{sand}} g, \tag{1.6}$$

where $\rho_{\text{sand}} \approx 2$ g/cm^3 is the density of the material compositing the grains and g is the acceleration due to gravity. The force of gravity that must be overcome to move a single grain is around $\sim$700 pN.

The flow inside the granular packing and thus the flow around a single particle is a low Reynolds-number flow, or creeping flow. If a single grains would be subjected to the average flow conditions that are present in the bed, the air would not move the particle, since both the drag force and pressure gradient force are smaller than the gravitational force. This is consistent with what is observed in the experiments: If such a pressure difference is applied over the sand we do not see movement of the bed as a whole. Of course, the real situation is much more complicated than this one grain example: We have an interconnected packing of grains and the pores in-between the grains are irregular and have a large size distribution. On top of that, in this thesis, we examine the sand bed after we have disturbed it by an external perturbation. Due to these effects, locally larger pressure changes and higher flow velocities are present. It is plausible that in these situations air is capable of moving the sand grains.

Another aspect to consider (especially for experiments at reduced ambient pressure) is the Knudsen number of the interstitial gas:

$$\text{Kn} \equiv \frac{\lambda}{L}, \tag{1.7}$$

where λ is the mean free path of the gas and L the typical length between collisions with the walls, in this case the pore size. If the pore size of the granular material becomes of the same order of the mean free path of the air, a continuum description of the gas is no longer valid. The pore sizes in our sand bed vary over a large size range, and it is therefore difficult to define an average pore size. We can however postulate that the pores must be of the same order as the size of the sand grains ~ 10 nm. The mean free path for air at atmospheric pressure is tens of nanometers, resulting in a Knudsen number of the order of 0.001, where air can be treated as a continuos medium. However, the mean free path increases for lower ambient pressures resulting in Knudsen numbers for our reduced pressure measurements (at 10-100 mbar) between 0.01 and 0.1. Here it is possible that the no-slip boundary condition breaks down, which would slightly increase the permeability [39–42].

1.4 Influence of interstitial air

In several phenomena the influence of air in-between the grains is reported. A very striking example is Faraday heaping, in which a layer of grains is vibrated

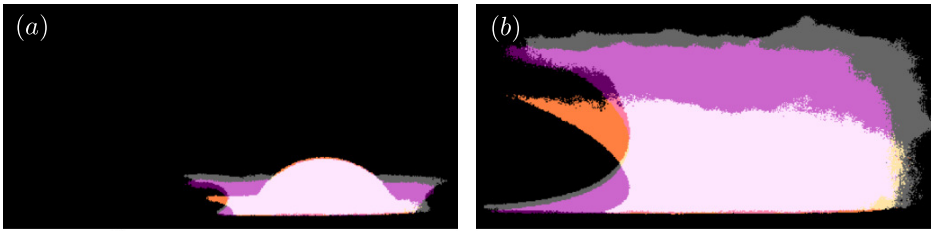

Figure 1.3: The splash created during an impact on sand [46]. The three different colors show the splash at 5 mbar (orange), 400 mbar (pink), and 1 bar (grey). (a) 5 ms after the initial contact between the ball and the sand it is visible that the splash at the higher ambient pressures is created earlier and the grains are ejected with a higher initial velocity. (b) At later times (20 ms after impact) the shape of the different splashes starts to vary: At higher ambient pressures the splash is more vertical than at lower pressures.

and heaps of grains form which, in time, merge into larger heaps [43]. Faraday suggested that air must play a key role in the formation of these heaps and this is indeed found to be the case [44, 45]. The air drag on the particles is asymmetric, promoting heap formation and both experiments at significantly reduced pressure and simulations without air show no heap formation at all.

The next example is closely related to the work described in this thesis. A metal ball impacts on a very loose sand bed and upon impact particles are ejected forming a thin, crown-shaped sheet, see figure 1.3 [46]. The figure is an overlay of three different experiments performed at ambient pressures of 5 mbar, 400 mbar and 1 bar. For higher ambient pressures the particles are ejected earlier and with a higher ejection velocity, as seen 5 ms after impact in figure 1.3a. At larger times (figure 1.3b) the shape of the splash is a lot more vertical for higher ambient air pressure, than for low pressures. This is at least in part due to suction of the air that flows after the ball into the cavity that is formed behind it.

This brings us to the last example of the influence of air. A ball impacting on loose sand is able to penetrate the bed and move downwards [47–52]. The final depth a ball reaches impacting from the same initial height depends on the ambient pressure inside the container, and surprisingly the ball travels deeper into the bed at atmospheric pressure than at low ambient pressures [51, 53]. Caballero *et al.* propose a mechanism where the airflow around the ball locally fluidizes the sand, effectively reducing the drag on the ball [51]. At lower air pressures this effect would become less pronounced and the higher drag decelerates the ball faster, bringing the ball to a stop higher in the bed. Royer *et al.* suggest that air trapped inside the sand introduces a cushioning effect, preventing the compaction of sand below the impacting sphere [50]. It is easier for the ball to move through the

unperturbed sand that is still in a very loose state, than through the layers of sand that are compactified in front of the ball. Since this mechanism only works when air is present in the sand pores, a reduction of the air pressure inside the setup reduces the effect and increases the drag that the ball experiences.

The impacting ball introduces a separate but equally important scale at which to investigate the system. The impact energy or velocity is usually described by the dimensionless Froude number. The Froude number is a ratio of inertial and gravitational forces

$$\mathrm{Fr} \equiv \frac{2v^2}{gD}, \tag{1.8}$$

where v is the velocity of the impacting ball, and D its diameter (in our case 16 mm). On this scale it is valid to neglect the air drag which makes it easy to calculate the impact velocity from the release height above the bed h: $v = \sqrt{2gh}$. This reduces the Froude number to

$$\mathrm{Fr} = \frac{4h}{D}. \tag{1.9}$$

A typical release height in our setup is 40 cm which gives an impact velocity of almost 3 m/s and a Froude number of 100.

The Reynolds number for the airflow around the impacting ball is of the order of 1000. On the length scale of the release height the air will not significantly alter the motion of the ball, but the air around the ball will be able to influence the sand grains as soon as it approaches the bed.

Apart from the fundamental interest of these issues, there are numerous situations in nature where sand (or other porous material like rock) is found with an interstitial fluid (such as air). Understanding the interaction between air and sand therefore has lots of possible applications. In enhanced oil recovery, oil is forced out of the earth by flooding it with water. The water will then replace the oil and push it up. But when a fluid with a lower viscosity (like water) displaces a large viscosity fluid (like oil) a Saffman-Taylor instability can form [54]. The interface between the two liquids starts to deform into a fingerlike structure and if the water filled fingers grow larger, water is pumped up in stead of oil. This makes it more difficult and less efficient to get all the oil out. The process would benefit from a better understanding of the interaction between fluids and granular matter.

A part of our drinking water supply is still cleaned naturally for example in the *waterleidingduinen* (the dunes in the Western part of the Netherlands). The water is filtered while it moves vertically downward through the soil and is pumped up from lower depths. The rate at which (rain) water is absorbed by a porous medium

like soil depends on the properties of the granular medium (the compactness, the permeability, and the composition of the soil) and on for instance the water content [55, 56]. Also these flows are described by Darcy's law, the relation describing the fluid flow through a sand bed, which is the object we study in this thesis.

1.5 Guide through this thesis

From all of the above it is clear that air indeed can have a significant influence on the dynamics of sand. In these particular problems, however, it remains unclear how the air is distributed in the sand, what the local air pressure buildup is, and what is the exact effect of the interstitial air on the drag experienced by penetrating objects?

In this thesis we investigate the influence of interstitial air in the granular impact experiment. Until now, the characteristics of the events below the surface had to be derived from what was visible above the sand. Of course it is not possible to "look" through a sand bed with visible light, as one would do for impacts on water, but X-rays are able to penetrate the sand. Experiments using high-speed X-ray imaging in a tomography setup of a ball impacting on sand are described in chapter 2. Thorough analysis results in a description of the cavity shape and the shape of the entrained air bubble, and we find the regions in which sand is being compacted after and during the experiment.

Another way of determining what happens inside the sand bed in a noninvasive way, is by measuring the pressure above and below the sand. Even though it is not a direct measure of the pressure distribution inside the sand it is possible to deduce the pressure profile starting from these measured pressures. In chapter 3 an initially loose sand bed is perturbed by a ball hitting the container wall. This shock collapses the sand bed, trapping air in the pores and thus increasing the pressure inside the bed, while the pressure above the bed is lowered due to the sudden volume increase. The newly formed pressure difference relaxes until the pressure in the entire container is equalized. A theoretical analysis indicates how all the experimental data can be collapsed and predicts the observed pressure changes accurately.

In the next chapter (chapter 4) we investigate the pressure signals above and below the bed during the impact events. We find that an increasing amount of air is being trapped inside the sand while the ball moves down. This continues until the air has time to diffuse out of the bed and an equilibrium is set up. The collapse of the cavity created behind the ball accounts for the rest of the pressure

changes and is clearly visible in the pressure signal.

The way a pressure difference decays in time is described by Darcy's law (chapter 5). The relaxation time of this exponential behavior depends on the compaction of the bed and also strongly on the ambient pressure. A comparison is made of the relaxation of pressure differences created in three different ways: By a constant airflow through the bed, through the shock experiments of chapter 3, and caused by the impact of a sphere as discussed in chapter 4. This analysis reveals how the excess air in the bed is distributed.

A last method to investigate what happens inside the sand bed is by measuring the forces that act on the ball at the impact and during the penetration of a granular bed. An instrumented particle, which measures the acceleration -and thus, through Newton's second law, the force- it experiences as a function of time, is used in chapter 6. The signal shows the effects on the ball by, for instance, the impact and the jet formation.

In the last chapter (chapter 7) we directly measure the forces that act on a ball while it penetrates the sand bed. For this, the ball is attached, via a load cell, to a linear motor which very controllably pushes the ball with a predetermined velocity to a certain depth. We find a clear dependance of the measured drag force on the intruder velocity: If air has ample time to move out of the way (for very low impact speeds) the measured drag is much higher than at larger velocities. Experiments at varying ambient pressures show a very pronounced drag reduction caused by the interstitial air.

References

[1] J. Duran, *Sand, Powders, and Grains: An introduction to the physics of granular materials*, Springer, New York (2000).

[2] J. Duran, *The physics of fine powders: plugging and surface instabilities*, C. R. Physique **3**, 217 (2002).

[3] F. Charru, B. Andreotti, and P. Claudin, in *Sand Ripples and Dunes*, , Annu. Rev. Fluid Mech. **45**, 469 (2013).

[4] H. Jaeger, S. Nagel, and R. Behringer, *Granular solids, liquids, and gases*, Rev. Mod. Phys. **68**, 1259 (1996).

[5] H. Jaeger, S. Nagel, and R. Behringer, *The physics of granular materials*, Phys. Today **49**, 32 (1996).

[6] D. van der Meer, K. van der Weele, P. Reimann, and D. Lohse, *Compartmentalized granular gases: Flux model results*, J. Stat. Mech. (2007).

[7] S. R. Waitukaitis, H. F. Gruetjen, J. R. Royer, and H. M. Jaeger, *Droplet and cluster formation in freely falling granular streams*, Phys. Rev. E **83**, 051302 (2011).

[8] M. Cates, J. Wittmer, J. Bouchaud, and P. Claudin, *Jamming and static stress transmission in granular materials*, Chaos **9**, 511 (1999).

[9] I. Albert, P. Tegzes, B. Kahng, R. Albert, J. Sample, M. Pfeifer, A. Barabasi, T. Vicsek, and P. Schiffer, *Jamming and fluctuations in granular drag*, Phys. Rev. Lett. **84**, 5122 (2000).

[10] A. Coniglio and M. Nicodemi, *The jamming transition of granular media*, J. Phys. Cond. Matt. **12**, 6601 (2000).

[11] G. D'Anna and G. Gremaud, *The jamming route to the glass state in weakly perturbed granular media*, Nature **413**, 407 (2001).

[12] E. Corwin, H. Jaeger, and S. Nagel, *Structural signature of jamming in granular media*, Nature **435**, 1075 (2005).

[13] G. Caballero, E. Kolb, A. Lindner, J. Lanuza, and E. Clement, *Experimental investigation of granular dynamics close to the jamming transition*, J. Phys. Cond. Matt. **17**, S2503 (2005).

[14] W. G. Ellenbroek, E. Somfai, M. van Hecke, and W. van Saarloos, *Critical scaling in linear response of frictionless granular packings near jamming*, Phys. Rev. Lett. **97**, 258001 (2006).

[15] A. R. Abate and D. J. Durian, *Approach to jamming in an air-fluidized granular bed*, Phys. Rev. E **74**, 031308 (2006).

[16] B. Chakraborty and B. Behringer, *Jamming of granular matter*, Encyclopedia of Complexity and Systems Science 4997 (2009).

[17] B. P. Tighe, J. H. Snoeijer, T. J. H. Vlugt, and M. van Hecke, *The force network ensemble for granular packings*, Soft Matt. **6**, 2908 (2010).

[18] M. P. Ciamarra, M. Nicodemi, and A. Coniglio, *Recent results on the jamming phase diagram*, Soft Matt. **6**, 2871 (2010).

[19] A. Mehta, *Real sandpiles - dilatancy, hysteresis and cooperative dynamics*, Physica A **186**, 121 (1992).

[20] J. Wittmer, P. Claudin, M. Cates, and J. Bouchaud, *An explanation for the central stress minimum in sand piles*, Nature **382**, 336 (1996).

[21] C. Moukarzel, *Isostaticity in granular matter*, Gran. Matt. **3**, 41 (2001).

[22] J. Socolar, D. Schaeffer, and P. Claudin, *Directed force chain networks and stress response in static granular materials*, Eur. Phys. J. E **7**, 353 (2002).

[23] S. Edwards and D. Grinev, *Statistical mechanics of granular materials: Stress propagation and distribution of contact forces*, Gran. Matt. **4**, 147 (2003).

[24] J. Snoeijer, T. Vlugt, W. Ellenbroek, M. van Hecke, and J. van Leeuwen, *Ensemble theory for force networks in hyperstatic granular matter*, Phys. Rev. E **70**, 061306 (2004).

[25] J. Snoeijer, T. Vlugt, M. van Hecke, and W. van Saarloos, *Force network ensemble: A new approach to static granular matter*, Phys. Rev. Lett. **92**, 054302 (2004).

[26] T. Majmudar and R. Behringer, *Contact force measurements and stress-induced anisotropy in granular materials*, Nature **435**, 1079 (2005).

[27] C. Goldenberg and I. Goldhirsch, *Friction enhances elasticity in granular solids*, Nature **435**, 188 (2005).

[28] I. Zuriguel, T. Mullin, and J. M. Rotter, *Effect of particle shape on the stress dip under a sandpile*, Phys. Rev. Lett. **98**, 028001 (2007).

[29] C. Goldenberg and I. Goldhirsch, *Effects of friction and disorder on the quasistatic response of granular solids to a localized force*, Phys. Rev. E **77**, 041303 (2008).

[30] Y. Fukumoto, H. Sakaguchi, and A. Murakami, *The role of rolling friction in granular packing*, Gran. Matt. **15**, 175 (2013).

[31] S. Papanikolaou, C. S. O'Hern, and M. D. Shattuck, *Isostaticity at Frictional Jamming*, Phys. Rev. Lett. **110**, 198002 (2013).

[32] B. Miller, C. O'Hern, and R. Behringer, *Stress fluctuations for continuously sheared granular materials*, Phys. Rev. Lett. **77**, 3110 (1996).

[33] A. Drescher and G. de Josselin de Jong, *Photoelastic verification of a mechanical model for flow of a granular material*, J. Mech. Phys. Solids **20**, 337 (1972).

[34] H. Janssen, *Versuche über Getreidedruck in Silozellen*, Z. Ver. Dt. Ing. **39**, 1045 (1895).

[35] U. M. B. Marconi, A. Petri, and A. Vulpiani, *Janssen's law and stress fluctuations in confined dry granular materials*, Phys. A **280**, 279 (2000).

[36] H. Darcy, *Les Fontaines Publiques de la Ville de Dijon*, Victor Dalmont, Paris (1856).

[37] P. Carman, *Flow of gases through porous media*, Butterworths Scientific, London (1956).

[38] P. K. Kundu, I. Cohen, and D. Dowling, *Fluid Mechanics (5th edition)*, Elsevier Academic Press (2011).

[39] M. Knudsen, *Die Gesetze der Molekularströmung und der inneren Reibungsströmung der Gase durch Röhren*, Ann. der Phys. **333**, 75 (1909).

[40] M. Kaviany, *Heat transfer in porous media*, Handbook of heat transfer, chapter 9, McGraw-Hill, New York (1998).

[41] E. S. Huetter, N. I. Koemle, G. Kargl, and E. Kaufmann, *Determination of the effective thermal conductivity of granular materials under varying pressure conditions*, J. Geophys. Res. **113**, E12004 (2008).

[42] A. S. Ziarani and R. Aguilera, *Knudsen's permeability correction for tight porous media*, Transp. Porous Med. **91**, 239 (2012).

[43] M. Faraday, *On a peculiar class of acoustical ïňĄgures; and on certain forms assumed by groups of particles upon vibrating elastic surfaces*, Philos. Trans. R. Soc. London **52**, 299 (1831).

[44] H. Pak, E. van Doorn, and R. Behringer, *Effects of ambient gases on granular-materials under vertical vibration*, Phys. Rev. Lett. **74**, 4643 (1995).

[45] H. J. van Gerner, M. A. van der Hoef, D. van der Meer, and K. van der Weele, *Interplay of air and sand: Faraday heaping unravelled*, Phys. Rev. E **76**, 051305 (2007).

[46] G. A. Caballero-Robledo, K. P. D. Kelly, T. A. M. Homan, J. H. Weijs, D. van der Meer, and D. Lohse, *Suction of splash after impact on dry quick sand*, Granular Matter **14**, 179 (2012).

[47] S. Thoroddsen and A. Shen, *Granular jets*, Phys. Fluids **13**, 4 (2001).

[48] D. Lohse, R. Bergmann, R. Mikkelsen, C. Zeilstra, D. van der Meer, M. Versluis, K. van der Weele, M. van der Hoef, and H. Kuipers, *Impact on soft sand: Void collapse and jet formation*, Phys. Rev. Lett. **93**, 198003 (2004).

[49] D. Lohse, R. Rauhe, R. Bergmann, and D. van der Meer, *Creating a dry variety of quicksand*, Nature **432**, 689 (2004).

[50] J. Royer, E. Corwin, A. Flior, M. Cordero, M. Rivers, P. Eng, and H. Jaeger, *Formation of granular jets observed by high-speed X-ray radiography*, Nature Phys. **1**, 164 (2005).

[51] G. Caballero, R. Bergmann, D. van der Meer, A. Prosperetti, and D. Lohse, *Role of air in granular jet formation*, Phys. Rev. Lett. **99**, 018001 (2007).

[52] S. von Kann, S. Joubaud, G. A. Caballero-Robledo, D. Lohse, and D. van der Meer, *Effect of finite container size on granular jet formation*, Phys. Rev. E **81**, 041306 (2010).

[53] J. R. Royer, E. I. Corwin, P. J. Eng, and H. M. Jaeger, *Gas-mediated impact dynamics in fine-grained granular materials*, Phys. Rev. Lett. **99**, 038003 (2007).

[54] P. G. Saffman and G. Taylor, *The penetration of a fluid into a porous medium or Hele-Shaw cell containing a more viscous liquid*, Proc. R. Soc. Lond. A **245**, 312 (1958).

[55] G. Delon, D. Terwagne, S. Dorbolo, N. Vandewalle, and H. Caps, *Impact of liquid droplets on granular media*, Phys. Rev. E **84**, 046320 (2011).

[56] J. O. Marston, I. U. Vakarelski, and S. T. Thoroddsen, *Sphere impact and penetration into wet sand*, Phys. Rev. E **86**, 020301 (2012).

2

High-speed X-ray imaging of a ball impacting on loose sand *

When a ball is dropped in fine, very loose sand, a splash and subsequently a jet are observed above the bed, followed by a granular eruption. To directly and quantitatively determine what happens inside the sand bed, high-speed X-ray tomography measurements are carried out in a unique custom-made setup that allows for imaging of a large sand bed. They reveal the formation of an air cavity behind the penetrating ball, which collapses and produces a jet. Below the pinch-off a bubble is entrained which rises to the surface, the shape and rising velocity of the bubble are consistent with bubbles rising in continuously fluidized beds. In addition, we measure the packing fraction variation, minute changes in the X-ray signal, throughout the bed. We find a compressed area of sand in front and next to the ball while the ball is moving down, a strongly compacted region at the pinch-off height, and a relatively loosely packed center in the wake of the rising bubble.

*To be submitted as: Tess Homan, Rob Mudde, Detlef Lohse, and Devaraj van der Meer, "High-speed X-ray imaging of a ball impacting on loose sand".

2.1 Introduction

When an object impacts on a deep layer of water a splash is formed and a few milliseconds later a jet shoots out of the water. Upon impact of a steel ball on a bed of fine, very loose sand under certain conditions similar phenomena are visible above the surface [1–5]. Here we address the following question: What are the mechanisms that drive the events visible above the surface?

Because of the transparent nature of water it is possible to directly observe what happens below the surface [6–9]. While the intruder moves through the water layer, an air cavity is formed. The walls of the cavity move toward each other due to hydrostatic pressure. At the moment the cavity walls collide two jets are formed, one going up and one going down. The cavity that remains below the pinch-off point moves down with the intruder, detaches, and then slowly rises to the surface. Since the phenomena above the surface in water and sand appear to be very similar, the question that arises is: What happens below the surface of the granular bed and to what extent is this similar to the sequence of events in water?

To answer these questions we must "look" inside the sand bed. Previously, this has been done with a parallel X-ray beam by Royer *et al.* [4, 10]. From these experiments it was concluded that in the granular case there is cavity formation and a pinch-off as well. However, due to restrictions on the X-ray apparatus used, these experiments were conducted in a miniature setup much smaller than the setups used in [2, 3, 5, 11] which can lead to unwelcome boundary effects [12]. For the same reason, the silica particles (sand) of [2, 3, 5, 11] were substituted by Boron Carbide particles.

In this chapter we describe impact experiments done in a custom-made high-speed X-ray tomography setup which is large enough to allow for the direct study of the experiments described in [2–5, 11], *i.e.*, in the original size and using the same silica sand bed. In the next section the experimental setup will be introduced, whereafter we describe three different ways to analyze the data. First the air-cavity and jet formation will be reconstructed in 'Cavity reconstruction'. In the 'Rising air bubble' section we will take a close look into the shape and rising mechanism of the air bubble. Last, in 'Local packing fraction', the density changes of the sand around the ball and the air-cavity are explored.

2.2 Experimental setup

A cylindrical container that is 1 m high and with an inner diameter of 15 cm is filled with sand until a certain height H (see figure 2.1). The bottom of the container consists of a porous material to allow for fluidization of the sand and the container is fully closed. An electromagnet is suspended from a rod, such that a metal ball (diameter $d = 3$ cm) can be released from different heights. Before every experiment the sand is fluidized to destroy the existing network of contact forces, and subsequently the airflow is turned off slowly to allow the sand to settle into a very loose state. The height of the sand bed above the plate after fluidization (H) and the release height (h) are measured. The size distribution of the individual sand grains ($\rho = 2.21 \pm 0.04$ g/cm^3) is between 20 μm and 40 μm and the average packing fraction after fluidization is 0.41.

The container is placed in an unique custom-built X-ray setup [13–15] (also shown in figure 2.1), which consist of three powerful X-ray sources (*Yxlon*, 4 Amp.) with three arrays of detectors placed in a triangular configuration. A single detector bank consists of two horizontal rows (spaced 40 mm apart) of 32 detectors that are positioned on an arc such that the distance between de source and the detectors is constant at 1386 mm. Each detector consists of an $CdWO_4$ scintillation crystal ($10 \times 10 \times 10$ mm) coupled to a photo diode and the data is collected with a sampling frequency of 2500 Hz. Two sets of experiments were carried out. One with the container in the center of the X-ray setup and measurements are taken by all three detector banks, and a second set of experiments where the container is placed close to one of the sources (distance 275 mm) for enhanced spatial resolution and measurements are taken from only one detector bank.

Each detector measures the attenuation of the X-rays on the path between the source and the detector. The attenuation of single wavelength X-rays are described by the Lambert-Beer law [14, 15], which states that there is a logarithmic dependence between the number of registered photons per second and the absorption coefficient of the specific material times the path length. In this problem the only parameters that change are the path length through sand and the path length through air, where the latter can be neglected in this setup due to the very low absorption of X-rays by air.

Every single detector is calibrated such that it gives the length of prepared sand on the path between the source and the detector, l_s. As a first point in the calibration we used a fully fluidized bed. Note that because the container has a circular cross-section the length of the path through the sand varies for different detectors. Next, we place a rectangular container filled with air inside the bed in the path of the rays, and again prepare the bed. This changes the amount of sand

in-between the X-ray source and the detectors. The boxes are made of very thin plastic to minimize their influence on the X-ray signal. When the exact position of the containers is known it is possible to calculate the equivalent path length (*i.e.*, the length of the path the X-ray travels through the sand, as calculated from the measured signal) for each detector.

2.3 Cavity reconstruction

How can we reconstruct what happens inside the sand when a ball impacts? With the setup described above we measure the response of the bed in one horizontal cross-section as a function of time. Because we are interested in the complete cavity shape within the bed, the experiment will have to be repeated while measuring at different heights, z. The results can later be stitched together. This method requires that the experiment is very reproducible. To check this we first examine the center detector signals for several repetitions of the experiment at an average depth within the sand while the ball penetrates the bed.

2.3.1 Center detector

The signals of the center detector for different experiments at a fixed height are shown in figure 2.2a. On the vertical axis the change Δl of the equivalent path length (*i.e.*, compared to the situation before impact) is plotted during the impact. When the ball passes through the measurement plane the signal of the central detectors drops due to the higher absorption coefficient for X-rays of metal compared to sand. This leads to an increase of Δl (I). Immediately after the ball passes, the signal Δl becomes negative (II), indicating that in the path of the ray there is less sand than would fit in the container, *e.g.*, as would happen when an air cavity has formed in the wake of the ball. This implies that there is more air in the sand at this height, but it does not reveal how this air is distributed. The bed may have become very loose such that the air is evenly distributed, or the air may be concentrated in the center as an air cavity. Some time later a negative peak again suggests the presence of air (III).

The different lines show four different realizations of the experiments all recorded at the same measurement plane in the sand. Two of them are measured with the upper detector row and two of them with the lower array of detectors. The first part is very reproducible, which can be concluded from the fact that the equivalent path lengths and the duration of the peaks are equal. The second part, 200 ms to 400 ms after impact, is less reproducible. The measured values are

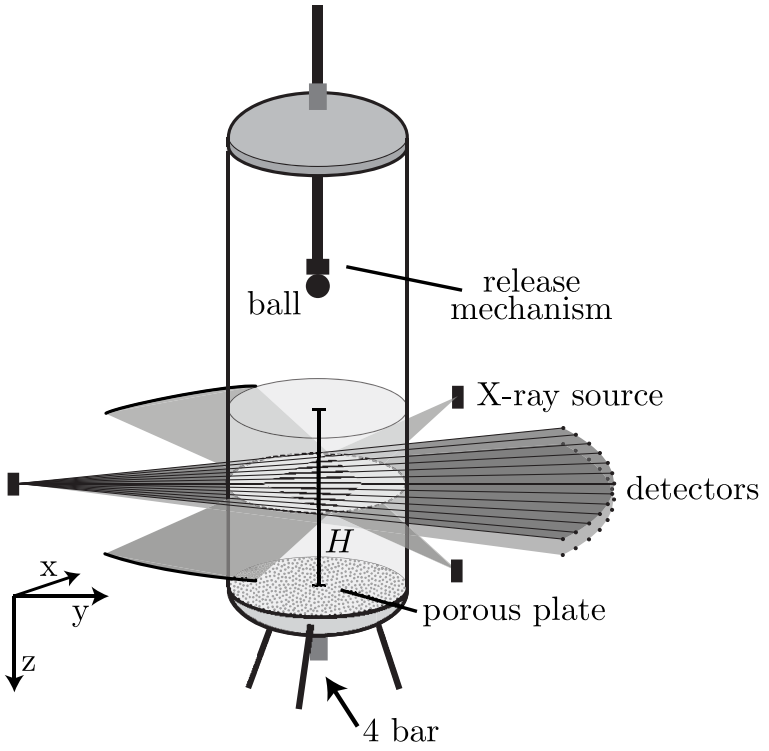

Figure 2.1: Schematic of the setup used in the X-ray experiments. The setup consists of a container filled with very fine sand. Near the bottom a porous plate is mounted such that air can be blown in, fluidizing the sand. A ball is dropped from various heights using an electromagnet into a loosely settled bed. The setup is placed in a custom-made tomographical X-ray device consisting of 3 X-ray sources and 6 arrays of 32 detectors: Opposite to each X-ray source two arrays of detectors are placed in one detector bank (only one bank is shown).

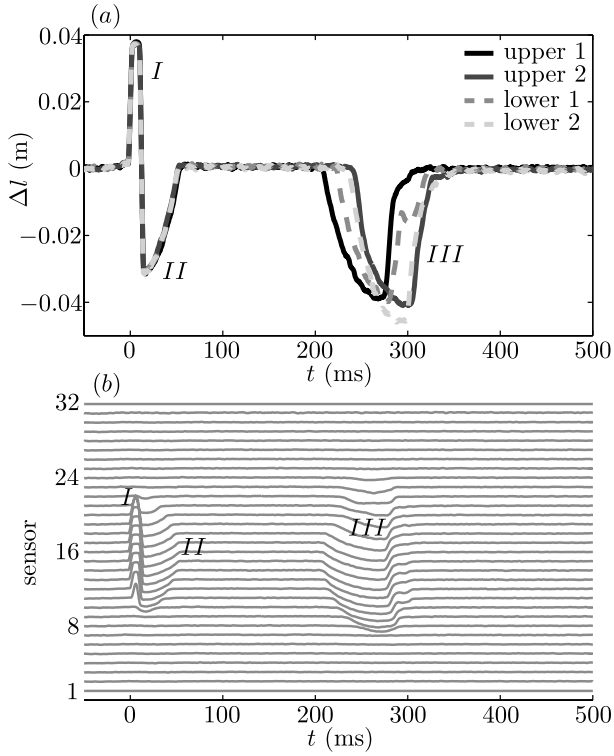

Figure 2.2: (a) The measured signal of the center detector as a function of time for four different realizations of an impact experiment using the same measurement height (z=8 cm below the surface). Two of the measurements are recorded with the upper detector bank and two measurements with the lower detector bank. When the ball passes through a ray the signal becomes higher, whereas an air cavity accounts for a lower signal. The first part of the signal, which corresponds to the passing of the ball (I), cavity creation, and cavity collapse (II), is very reproducible. The second part of the signal, corresponding to the rising air bubble (III), shows poor reproducibility. (b) The measured signals of all the sensors of one detector array measured in a single experiment at one fixed height, z. The number of detectors that see the ball (I) or the air cavities (II and III) provides an estimate of the size of the object. Similar-sized objects that are visible in the signal for longer time move with a lower velocity through the measurement plane.

similar, but the shape and timing of the peak are very different among different experiments. From this we can deduce that it must be possible to accurately reconstruct the impact within the sand bed, up to a certain amount of time after the ball has impacted ($t \leq 200$ ms). This timespan must at least be sufficient to image the formation of the jet, judging from the time scale ($t < 100$ ms) on which the latter forms.

2.3.2 Cavity size and shape

Since data is available from an entire array of detectors it is possible to obtain information about sizes and positions. The signals from the different detectors of one of the arrays are plotted above each other in figure 2.2b. The number of sensors that detect the ball (the positive part of the signal) reflect the width of the ball. The negative signals are concentrated in the center of the container indicating that the additional air exists in the form of an air cavity rather than somehow dispersed through the sand bed. These negative signals are found immediately after the ball passes (II) showing that the air cavity is attached to the ball. Since a similar number of detectors "see" both the cavity and the ball, the air cavity must have a width similar to that of the ball. The second air cavity (III), the signals of which arrive at the detectors after a considerable delay, is visible in more sensors than the ball, demonstrating a larger size of this second cavity, which can be interpreted as a detached air bubble rising through the sand bed. Note that an object moving at a lower velocity will have a longer X-ray signal duration because it is longer in field of view of the detector. The fact that the signal duration of the air bubble is longer than that of the air cavity doesn't mean that the air bubble is bigger; the magnitude of the signal however does give information about the size.

In figure 2.3a-f the change in equivalent path length is plotted as a grey scale value (white for positive and black for negative Δl) for different times during the experiment. The pixels in each row indicate the signal of the different detectors at a single height, whereas the different rows correspond to experiments done at different depths in the bed. This gives a first indication of what happens inside the sand bed. As the ball moves through the sand an air cavity behind the ball is generated (a). This air cavity grows while the ball moves and then starts to collapse under the influence of the granular "hydrostatic pressure" in the bed (b, c). When the walls of the cavity touch (d), a jet shoots upward and an air bubble is entrained. The air bubble moves down with the ball and after it detaches it slowly rises to the surface (e, f). From this analysis it is clear that the events in $(a - d)$ are highly reproducible, whereas the randomness and irregularity in the last two plots (e, f) reflects that the rising of the air bubble is not reproducible at

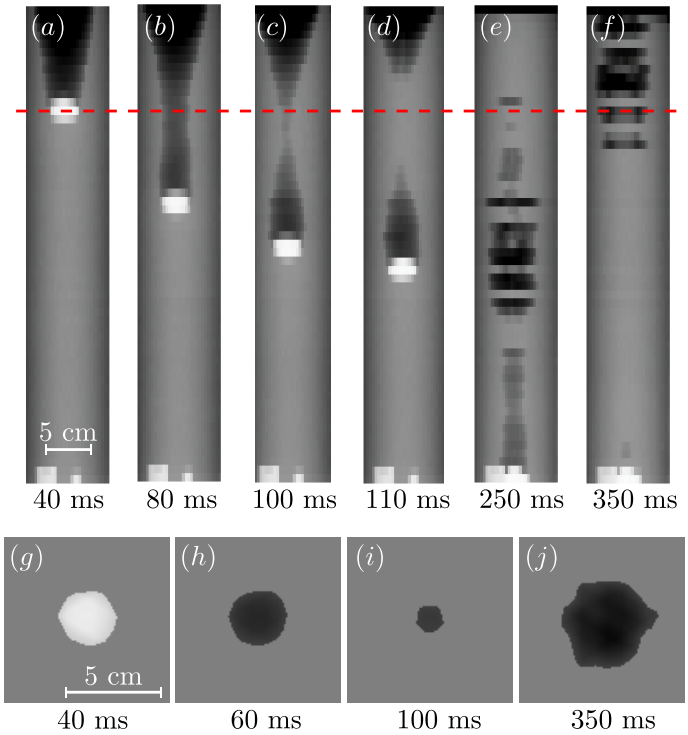

Figure 2.3: $(a-f)$ A series of plots at different times after the ball has impacted onto the sand bed at $t=0$. The grey-scale value represents the normalized signal. For each plot, the horizontal axis displays the signals of the different detectors and the vertical axis repetitions of the experiment with cross-sections taken at different depths in the bed. We clearly see the cavity first being formed and subsequently closing (a,b), the resulting pinch-off (c), the formation of the jet, and finally the entrapment of an air bubble in the sand (d). In the next plot (e) the air bubble detaches from the ball and slowly rises to the surface (f). $(g-j)$ Tomographic reconstruction of a single horizontal cross-section through the bed, see red dashed line in top figure, at 4 different times. From left to right: a measurement plane through the center of the ball (g), through the air cavity immediately behind the ball (h), the air cavity close to the collapse (i), and a cross-section through the rising air bubble (j).

all. The size of the latter varies considerably with height, indicating that in the different experiments to which they correspond the bubble detaches from the ball at different points in time, leaving empty gaps in the reconstruction. The critical question that remains is: To what extent are the cavities and resulting jets that are created axisymmetric? To obtain more insight into this issue, we will now look at the full tomographic information that is available from the setup.

2.3.3 Tomography

When the container is positioned in the center of the X-ray setup, a single horizontal cross-section can be imaged by three detector arrays spaced evenly around the contianer, allowing for tomographic measurements. Using tomography, we obtain the full 2D shape of the cross-section of the ball and the air-cavities. In figures 2.3g-j the tomographic reconstruction at a single height, for four different times during the experiment is shown. For the tomography the signals of all three detector banks are super-positioned on a square lattice of 140 by 140 pixels. By applying a threshold intensity value the cavity and the ball shape can be extracted. In the first image (g) the ball is visible, of which the size and shape are known. Indeed, within the limits of the reconstruction the ball is found to be round, and also the size is correctly estimated. In figure 2.3h a reconstruction of the air cavity just after the ball passed is provided. The air cavity is seen to have a similar degree of roundness as the ball, and has the same size as the ball, which is indeed what one would expect directly after the cavity is created. The second image of the air cavity (i) is taken just before the collapse, showing that the air cavity is still axisymmetric. The last reconstruction (j) is made at the time the bubble passes by. The bubble is not completely circular, and is rising slightly off-center. This is one of the origins of the poor reproducibility of the air bubble.

2.3.4 A single array

By moving the setup closer to one of the X-ray sources we are able to obtain a much higher spatial resolution. From the tomography analysis there are good indications that the cavity remains axisymmetric at least until the collapse. For such an axisymmetric cavity we can anticipate what the signals in the different detectors should look like, given the radius of the cross-section of the cavity. This is illustrated in the top half of figure 2.4a. To quantify the cavity shape as a function of time the cavity radius for every measurement (each height) needs to be determined at each point in time.

In figure 2.4b, for a given time and height, the measured equivalent path length

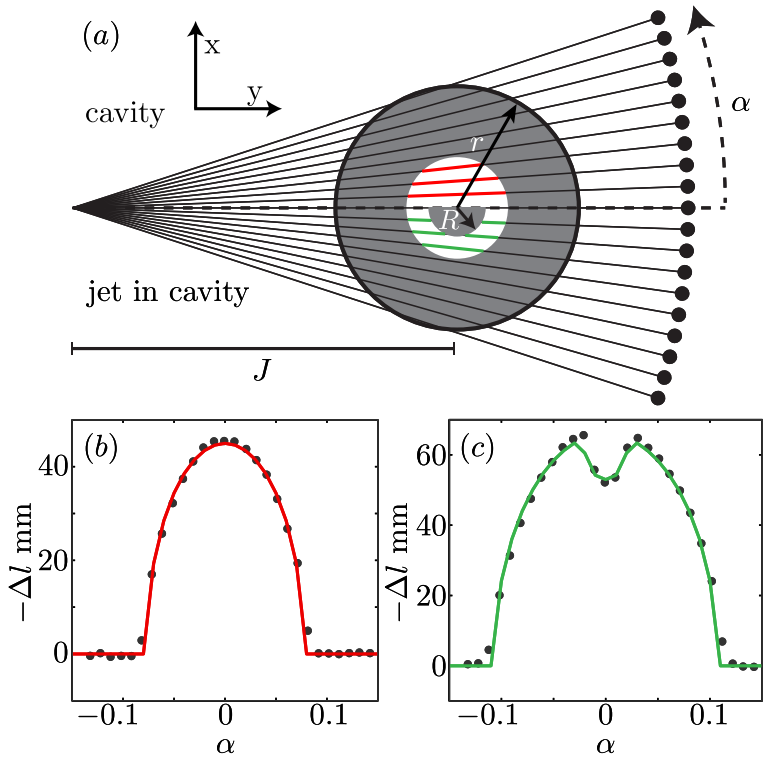

Figure 2.4: (a) Geometry of one horizontal cross-section of the bed. When the exact locations of the source and detectors with respect to the container are known it is possible to calculate the change of the equivalent path length Δl as a function of the angle α for both the case with a circular air cavity (upper half) and the situation in which a sand jet is present in the center of the air cavity (lower half). In (b,c) the equivalent path length Δl is plotted as a function of the angle α for two situations: (b) an air cavity in the sand bed and (c) a jet within the air cavity. Both signals are fitted to the theoretical case of a circular cavity and a circular jet.

is plotted as a function of the angle between the detector and the center detector when there is an air cavity present. This data can be fitted with the expectation for an axisymmetric air cavity in the center of the container, as shown in the top half of figure 2.4a. The equivalent path length of a circular cavity of radius r as a function of the angle α is calculated to be

$$\Delta l(r,\alpha) = -2\sqrt{\frac{(r^2 - J^2)\tan\alpha^2 + r^2}{\tan\alpha^2 + 1}}, \tag{2.1}$$

where J is the known distance between the X-ray source and the center of the container. This function is fitted to the obtained data to get the cavity radius r, red line in figure 2.4b.

After the collapse a jet occurs inside the air cavity in some of the cross-sections, as illustrated in the bottom half of figure 2.4a. This will change the signal as shown in figure 2.4c, where we observe a shape similar to that of figure 2.4b, but with a pronounced dimple in the center. To calculate both the cavity radius and the jet radius, equation (2.1) is adapted such that the change in equivalent path length is calculated through two concentric circles. The larger circle is filled with air and the smaller one filled with sand: $\Delta l(r,\alpha) - \Delta(R,\alpha)$, where R is the radius of the jet. A fit for both r and R is plotted as a green line in figure 2.4c.

This fitting procedure is repeated for every time step and every measurement height, such that we are able to reconstruct the full axisymmetric cavity- and jet-shape as a function of time. The result of this analysis is shown in figure 2.5. In blue the cavity radius as a function of height is represented in the figure at several times after impact. The exact position of the ball could be extracted from the original data by looking at the maximum (see figure 2.2). The ball is plotted in figure 2.5 in red. Despite its small scale we were also able to reconstruct the jet that is created during the collapse. The last plot of figure 2.5 shows the jet in purple.

2.3.5 Cavity collapse

With the analysis described above the cavity radius is extracted as a function of time. It is now possible to take a closer look at the dynamics of the cavity collapse, both at and below the closure depth.

Collapsing air bubbles in incompressible liquids have been studied both theoretically and experimentally. Theory has shown that the time evolution of the cavity radius asymptotically and slowly converges to a power law with exponent $1/2$. More specifically, the local slope $\alpha = d\ln r/d\ln t$ has been shown to satisfy

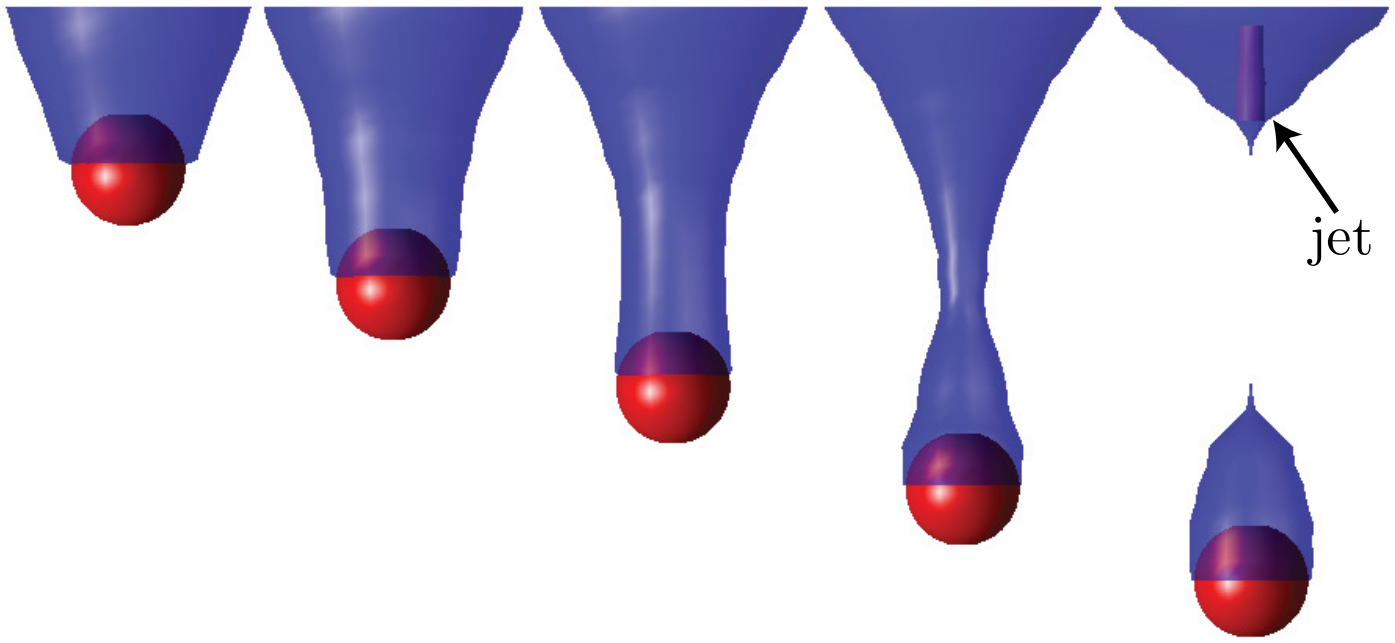

Figure 2.5: Several snapshots of the results from the analysis described in section 'Cavity reconstruction'. To obtain these images the equivalent path lengths measured in the X-ray setup are fitted to theoretical cavity shapes. Stitching together the experiments executed at different heights results in the blue air cavity. The ball position is also measured from the data and the ball is added to the images in red. For the last image the jet recreated from the data is visible in purple. The plots represent the situation 40, 60, 80, 100, and 120 ms after the impact.

$\alpha \approx 1/2 + 1/[4\sqrt{-\ln(t_c - t)}]$ [16–19]. In experiments and numerics this leads to behavior that over several decades is very hard to distinguish from a power law [18, 20], with a measured exponent that is slightly larger than $1/2$.

Is the behavior similar for a granular pinch-off, and what is the underlying mechanism? In figure 2.6a the cavity radius is plotted as a function of time on a double logarithmic scale, with the time given relative to the closing of the void at t_c, *i.e.*, $t_c - t$.

The behavior is clearly consistent with a power law during the collapse of the cavity. The best fit exponent (green line) gives $r \sim (t_c - t)^{0.66}$, but due to limited resolution close to pinch-off we are not able to quantitatively compare with values found by Gekle *et al.* [18] for the void collapse in water. However, values for the exponent as high as 0.66 have also been found in the liquid impact experiment [20] which suggests that the mechanism of cavity collapse in a granular bed is quite similar to that in liquids. More specifically, our findings are consistent with the model of radial cavity collapse initiated by a hydrostatic (or lithostatic) driving pressure and continued by the inertia of the medium, as was already suggested in [2].

The final question we address is: How does the cavity collapse away from the point of first closure. To answer this question, in figure 2.6b we plot the absolute value of the radial closing velocity $|\dot{r}|$ as a function of the depth z, estimated in two ways. The first method we use is a global one in which we divide the maximum cavity radius by the time interval from the time this maximum is reached to cavity closure (squares in figure 2.6b). The second one is local and makes use of power-law fits of the type $r(t) = a(t_c - t)^b$ for every depth z from which the velocity $\dot{r}$ at a fixed distance $r_0 = 20$ mm is calculated as $\dot{r} = a(b-1)(t_c - t)^{b-1} = a(b-1)[r_0/a]^{(b-1)/b}$ (triangles). Both methods are consistent, but the second provides slightly larger values for $|\dot{r}|$ since the velocity diverges towards $r = 0$. In any case, clearly, the results of both methods show that $|\dot{r}|$ increases slowly with depth. This implies that a second –deeper– pinch-off is capable of creating a jet that could be almost as strong and fast as the first pinch-off. This supports the view put forward in [12] that the thick-thin structure first reported in [4] is caused by a secondary jet catching up with the first. By bursting through the primary pinch-off region it is then assumed to create the thick part of the visible jet.

2.4 Rising air bubble

A remaining question regarding the impact events is the mechanism by which the detached air bubble moves towards the surface. An intuitive way of thinking

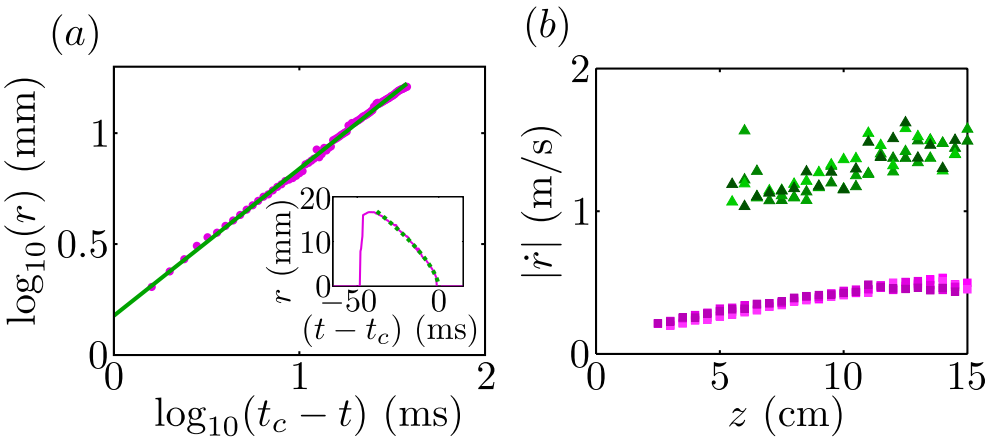

Figure 2.6: (a) Double logarithmic plot of the cavity radius as a function of time at z =8.0 cm below the surface, which is the closure depth. The cavity is created immediately after the ball has passed and in the beginning has roughly the same radius as the ball. As the cavity is collapsing, the signal decreases. The inset shows the same data in a linear plot. (b) Closing velocity $|\dot{r}|$ as a function of depth z, (i) estimated from dividing the distance and the duration of the collapse (starting from the maximum cavity radius, squares) and (ii) calculated from a power-law fit as in (a), evaluated at a radial distance of $r = 20$ mm from the symmetry axis (triangles).

about rising air bubbles in a granular medium is that the unsupported grains on top of the bubble "rain" down through the center into a pile at the bottom. This transport of material will give the bubble a net upward velocity. A second mechanism, often used for continuously fluidized beds, is closer to the rising of air bubbles in water. Material from the perimeter of the bubble is transported along the interface towards the bottom of the bubble, where a wake is formed.

In our experiment we do measure a rising bubble, but due to poor reproducibility of this part of the experiment we cannot stitch the different experiments at different heights together to obtain a spatial image (see figures 2.2 and 2.3). To reconstruct the bubble shape we therefore have to find a different method to analyze the data. Because the bubble is moving in the vertical direction, in due time the entire bubble will pass any horizontal cross section. This means that if the velocity of the bubble is known it is also possible to retrieve the shape of the bubble from a single experiment done at one height, such that we don't have to worry about reproducibility.

As shown in figure 2.1 we record the data with two detector arrays simultaneously. In a single experiment the air bubble will pass the two measurement planes that go from the X-ray source to the upper and lower array of detectors. The distance between these two planes in the center of the container is 4 mm. By determining the time difference of the front and back of the bubble passing the two measurement planes we obtain the speed of the front and back of the bubble. The difference in velocity between the front and the back is found to be small enough such that we can assume that the bubble rises with a constant speed. Comparing measurements at different heights, we find no clear trend of the bubble velocity as a function of height, which is at least partially due to the poor reproducibility of the experiment in this regime. We find that all bubble rise velocities are around 0.3 ± 0.1 m/s.

When the time axes are rescaled with the constant bubble speed we get a bubble shape as shown in figure 2.7. In the horizontal direction the information from the different detectors is displayed. The colors represent the depth of the bubble perpendicular to the plane of view. The bubble is spherical cap shaped, like a bubble rising in a fluid, or in a continuously fluidized bed. The bottom of the bubble is concave, which is consistent with either a pile or a wake.

In 1963 Davidson and Harrison [21] presented a relation for the rising velocity of a single bubble in a fluidized bed: $u_b = 0.71\sqrt{g d_{\mathrm{eq}}}$, where d_{eq} is the equivalent bubble diameter $d_{\mathrm{eq}} = (\frac{6}{\pi} V_b)^{\frac{1}{3}}$ with V_b the bubble volume. Now that we have the shape of the bubble we can estimate the velocity using this model which gives a value of 0.44 m/s. This is close to our experimental value, which is slightly lower.

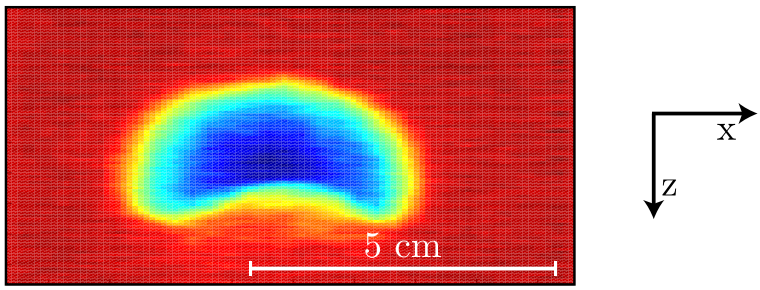

Figure 2.7: The shape of the rising air bubble. This shape is obtained by recording the radius of the air bubble that passes by in time at a single height. Plotting the signal from the different detectors gives the complete shape. The color indicates the width of the bubble perpendicular to the paper, dark blue is a width of 4.5 cm.

This stands to reason, since our bubble is not rising in a continuously fluidized bed and thus a lower velocity is expected.

We are not able to see if there is a rain of particles within the bubble, since we measure the average signal over a line instead of locally, and the density of the “rain" would be very low. However, the shape of the bubble and the rising velocity are close to bubbles rising in a continuously fluidized bed, suggesting that the rise mechanism will be similar as well.

The shape of our measured bubble is similar to the air bubble measured by Royer *et al.* in [4] although they have a different explanation for the shape. They attribute the concave bottom of the bubble to an impinging second jet, that grows to meet the first jet. We however find that the rise velocity is consistent with a rising air bubble, that will finally erupt at the surface, rather than overtaking the primary jet.

2.5 Local packing fraction

Until now we have assumed that the packing fraction of the bed does not change significantly. This assumption was necessary to calculate the air path lengths in the bed. By simply observing the experiment it is obvious that the packing fraction must change, since when we compare the bed height before and after impact we find that it has lowered [5]. From the initial very loose state that is created by the fluidization procedure we end up with a more compactified bed. We want to determine the corresponding change in the packing fraction, and we want to discover how the compactification is distributed throughout the bed.

The experiment provides the equivalent path length of the X-rays through the sand, l_s. Whenever a given X-ray does not encounter an air cavity in its path the change in this path length (Δl) before and after the experiment can, in first order, be related to a change in packing fraction by:

$$\frac{\Delta\phi}{\phi_{\text{before}}} = \frac{\Delta l}{l_{s,\text{before}}} \tag{2.2}$$

where $\Delta\phi$ needs to be interpreted as the average packing fraction changes along the path. Note that the values for $\Delta\phi$ given in this section correspond to much smaller Δl than those discussed in the previous section.

2.5.1 Packing fraction after the experiment

The local packing fraction after the experiment in the entire sand bed, calculated with equation (2.2), is shown in figure 2.8a. These measurements were taken several seconds after the ball has come to a halt, which assures that there are no air-cavities or bubbles left, and that only packing fraction variations are detected. Note that the packing fraction before the experiment was equal to 0.41, uniformly throughout the container. This means that the bed is compactified during the experiment.

We see a clear compacted region (pink area) next to where the ball has stopped. The packing fraction above the ball (in the center of the plot) is relatively low, and is the lowest just on top of the ball. The packing fraction below the ball slowly decreases with depth back to a value of 0.41. Wherefrom do these packing fraction variations originate, and what do they teach us about the events below the surface?

2.5.2 Time resolved packing fraction

To understand the packing fraction of the sand around the ball after the experiment we need to look into the local compaction while the ball is moving through the sand. To determine what happens with the sand just in front of the ball we zoom in on the signal before the ball passes by at a given height. This gives the bed density underneath the moving ball. To obtain sufficient data the signals of 20 different experiments at 10 different heights are averaged. The moment the ball passes by is used to synchronize the signals in time. To smoothen the signal a central scheme is used where the trend of the 10 previous points is extrapolated beyond the central point. In figure 2.8b the result of this analysis is shown. The blue curve ($\alpha = 0°$) passes through the center of the ball and therefore detects

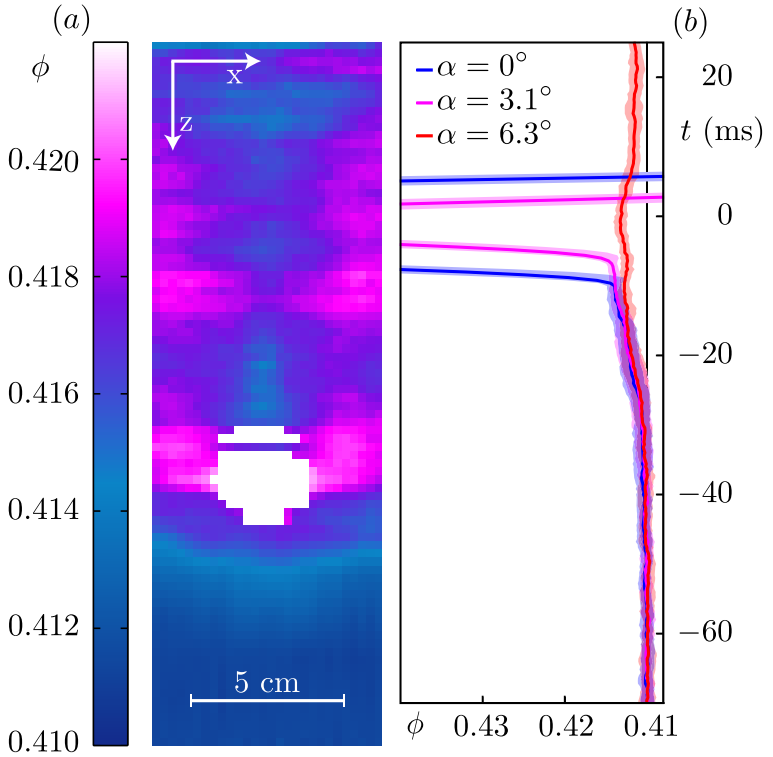

Figure 2.8: (a) A representation of the packing fraction of the bed after the experiment. The data is taken several seconds after the impact events have terminated, assuring that there are no air pockets left in the sand. The color indicates the packing fraction (ϕ). The sand next to the ball is quite compacted, whereas the vertical strip above the ball is relatively loose. The compaction below the ball decreases with depth. (b) The averaged packing fraction plotted as a function of time. To obtain the curves the signal of 20 different experiments is averaged. The three different curves give the signal from three different detectors, *i.e.*, for three different values of α. The transparent area around the curves indicates the statistical error. All three signals show a clear increase in packing fraction just before the ball the ball blocks out most X-rays.

the ball first. The other two curves show the signal through the side of the ball ($\alpha = 3.1°$) and completely beside the ball ($\alpha = 6.3°$). All three curves show a clear increase of the signal before the front of the ball passes. This shows that there is a compaction of the sand just before the ball arrives. Or, there is a compacted region being pushed in front of the ball. From the red curve ($\alpha = 6.3°$) we deduce that there is also compaction next to the ball. This compacted region is still present after the experiment is finished, as can be seen in figure 2.8a.

2.5.3 Packing fraction during penetration

The density differences of the sand during the experiment are very small, but it is possible to detect them if the signal is averaged over a sufficiently large time-window (see figure 2.8b). To image the packing fraction variations during the penetration around the ball we switch to the frame of reference of the ball such that we are able to do a time averaging. The result of this procedure is shown in figure 2.9. The red area below and next to the ball indicates a compacted region, just as we saw in the previous section. In time we see that the compacted region below the ball (yellow area) grows downwards relative to the ball. These results agree with data obtained by Royer *et al.* in [10], who see a growing compactified region in front of the ball, but most clearly for a case at low ambient pressure. The measurements provided here are sensitive enough to measure this effect at atmospheric pressure. In addition to what happens below the ball, we can also investigate the compaction above the ball. First the air cavity is visible (blue) and when the cavity collapses a growing red area indicates a compacted region next to the pinch-off. The data in figure 2.8a (taken after the experiment was done) shows a relatively uncompacted area in the center above the ball. This must be connected to the rising bubble rearranging the sand particles in its path. It suggest that the sand at the bottom of the bubble is deposited loosely, pointing to a slow and unpressurized mechanism.

2.6 Conclusion

Using a custom-made high-speed X-ray tomography setup we measured the events that occur below the surface when a ball impacts on a bed of fine, very loose sand. We were able to reconstruct the air cavity until and beyond the collapse by stitching together measurements done at different depths. From the cavity reconstruction we learned that the phenomena below the surface are similar to the events that occur during and after an impact in water: A cavity is formed

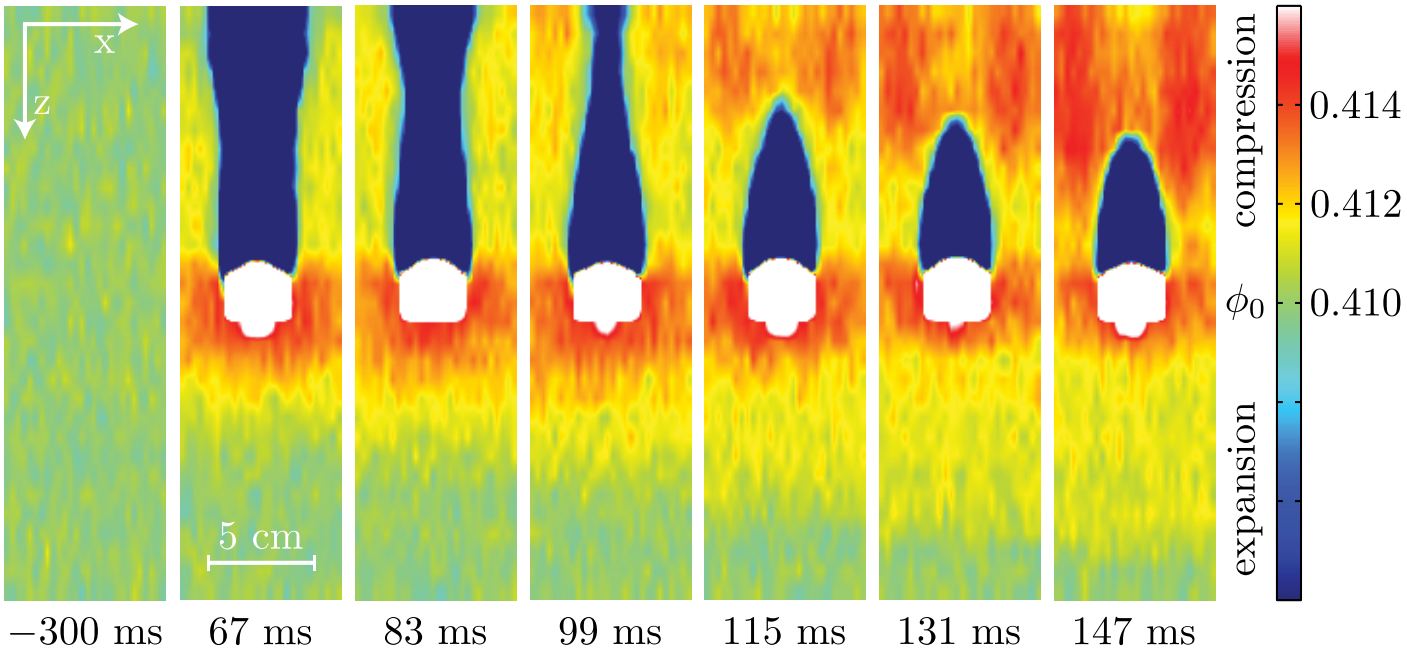

Figure 2.9: The packing fraction around the ball at several times during impact. To obtain these images we move along with the ball and averaged the signals around it. The first image shows the bed before impact (average packing fraction of 0.41). In the other frames we can see a compacted region to the sides and in front of the ball (red), a growing compactified region (yellow) and a strong compression above the ball where the air cavity pinches off.

behind the penetrating ball, the cavity collapses, creating a jet and entraining an air-bubble. Even the power law behavior with which the cavity collapses is consistent with pinch-offs that happen in liquids. Using the signal of a single experiment done at one height we were able to retrieve the shape of the rising air bubble. The shape of the bubble and the rising velocity is very similar to bubbles rising in a continuously fluidized bed.

During the experiment the sand bed is compactified. Even though the change in the signal caused by the compaction is very small compared to that from the air cavities, we were able to measure sand that is compressed in front and to the side of the ball while the ball moves through the bed. This compacted area grows in time and had a size of 2 ball diameters when the ball came to rest. The compaction does decrease with increasing distance from the ball, and is most pronounced in the center of of the container, below the ball. During the cavity collapse the sand at the collapse height is also greatly compressed. In the last step (the rising of the air bubble) the sand has time to rearrange itself. With the deposition of sand at the bottom of the bubble we end up with a relatively loose center and compacted sides. Just above the position where the ball stops we have the area with the lowest compaction. This is where the air bubble pinches off the ball, giving rise the an area depleted of sand grains.

References

[1] S. Thoroddsen and A. Shen, *Granular jets*, Phys. Fluids **13**, 4 (2001).

[2] D. Lohse, R. Bergmann, R. Mikkelsen, C. Zeilstra, D. van der Meer, M. Versluis, K. van der Weele, M. van der Hoef, and H. Kuipers, *Impact on soft sand: Void collapse and jet formation*, Phys. Rev. Lett. **93**, 198003 (2004).

[3] D. Lohse, R. Rauhe, R. Bergmann, and D. van der Meer, *Creating a dry variety of quicksand*, Nature **432**, 689 (2004).

[4] J. Royer, E. Corwin, A. Flior, M. Cordero, M. Rivers, P. Eng, and H. Jaeger, *Formation of granular jets observed by high-speed X-ray radiography*, Nature Phys. **1**, 164 (2005).

[5] G. Caballero, R. Bergmann, D. van der Meer, A. Prosperetti, and D. Lohse, *Role of air in granular jet formation*, Phys. Rev. Lett. **99**, 018001 (2007).

[6] A. Worhtington, *A Study of Splashes*, Longman and green, London (1908).

[7] H. Oguz and A. Prosperetti, *Bubble entrainment by the impact of drops on liquid surfaces*, J. Fluid Mech. **219**, 143 (1990).

[8] D. Lohse, *Bubble puzzles*, Phys. Today **56**, 36 (2003).

[9] R. Bergmann, D. van der Meer, S. Gekle, A. van der Bos, and D. Lohse, *Controlled impact of a disk on a water surface: Cavity dynamics*, J. Fluid Mech. **633**, 381 (2009).

[10] J. R. Royer, B. Conyers, E. I. Corwin, P. J. Eng, and H. M. Jaeger, *The role of interstitial gas in determining the impact response of granular beds*, Europhys. Lett. **93**, 28008 (2011).

[11] J. R. Royer, E. I. Corwin, B. Conyers, A. Flior, M. L. Rivers, P. J. Eng, and H. M. Jaeger, *Birth and growth of a granular jet*, Phys. Rev. E **78**, 011305 (2008).

[12] S. von Kann, S. Joubaud, G. A. Caballero-Robledo, D. Lohse, and D. van der Meer, *Effect of finite container size on granular jet formation*, Phys. Rev. E **81**, 041306 (2010).

[13] R. F. Mudde, J. Alles, and T. H. J. J. van der Hagen, *Feasibility study of a time-resolving X-ray tomographic system*, Meas. Sci. Technol. **19**, 085501 (2008).

[14] R. F. Mudde, *Time-resolved X-ray tomography of a fluidized bed*, Powder Technol. **199**, 55 (2010).

[15] R. F. Mudde, *Double X-ray tomography of a bubbling fluidized bed*, Ind. Eng. Chem. Res. **49**, 5061 (2010).

[16] J. Eggers, M. A. Fontelos, D. Leppinen, and J. H. Snoeijer, *Theory of the collapsing axisymmetric cavity*, Phys. Rev. Lett. **98**, 094502 (2007).

[17] J. M. Gordillo and M. Pérez-Saborid, *Axisymmetric breakup of bubbles at high Reynolds numbers*, J. Fluid Mech. **562**, 303 (2006).

[18] S. Gekle, J. H. Snoeijer, D. Lohse, and D. van der Meer, *Approach to universality in axisymmetric bubble pinch-off*, Phys. Rev. E **80**, 036305 (2009).

[19] V. Duclaux, F. Caille, C. Duez, C. Ybert, L. Bocquet, and C. Clanet, *Dynamics of transient cavities*, J. Fluid Mech. **591**, 1 (2007).

[20] R. Bergmann, D. van der Meer, M. Stijnman, M. Sandtke, A. Prosperetti, and D. Lohse, *Giant bubble pinch-off*, Phys. Rev. Lett. **96**, 154505 (2006).

[21] J. Davidson and D. Harrison, *Fluidized Particles*, Cambridge University Press (1963).

3

Collapsing granular beds: The role of interstitial air *

A pre-fluidized sand bed consisting of fine particles compactifies when it is subjected to a shock. We find that the response depends on both the shock strength and the ambient pressure where, counterintuitively, the bed height decreases less at lower ambient pressures. We investigate what happens to the interstitial air during compaction by measuring the pressure changes above and below the bed: The top pressure decreases abruptly, on the time scale of the compaction, whereas that below the bed slowly rises to a maximum. Subsequently both slowly relax to ambient values. A one-dimensional diffusion model using only the change in bed height and the ambient pressure as an input, accurately predicts the measured pressure variations.

3.1 Introduction

The presence of an interstitial fluid (*e.g.*, air) in a granular medium consisting of small grains (diameter $d < 1$ mm) is known to have significant influence on the dynamics. Well-known examples are the Brazil nut effect, in which air may cause

*To be submitted as: Tess Homan, Christa Gjaltema, and Devaraj van der Meer, "Collapsing granular beds: The role of interstitial air".

an intruder to rise instead of sink [1], Faraday-heaping, where the presence of air leads to the formation of heaps in a vibrated layer of grains [2–5], and inverse Chladni patterns, where air drag pushes small particles on a resonating plate to the antinodes rather than to the nodal lines where the larger grains aggregate [2, 6, 7].

A particularly intriguing example is the impact of an object on a pre-fluidized bed of fine sand where the presence of air has a profound influence on the splash shape and jet formation. Royer *et al.* found that the jet was suppressed significantly at lower ambient pressures [8], which Caballero *et al.* traced back to an increase of the drag [9]. Also, suction of air behind the object pulls the splash inwards which significantly alters its shape [10]. How the air affects this experiment is not yet understood, largely due to the complexity of the impact process.

We therefore turn to the role of air in a less complex experiment, namely the compaction of the sand bed after being subjected to a shock. Previous compaction research focused on the density change as a function of the number of compaction pulses, generally applied by a shaker [11–17]. Here the experiments are almost exclusively carried out under vacuum, to minimize cohesion forces and to avoid the influence of the interstitial fluid[†]. It was found that compaction decreases with the amount of taps, eventually leading to a static state in which the bed no longer compactifies.

In this chapter we study the influence of the air during a single compaction event of an initially loosely packed sand bed. In a very loose packing the grains have just enough contacts to form a stable configuration, but the slightest shock will destroy this fragile state and compactify the system. If the grains are sufficiently small –as is the case in our experiment– the role played by the interstitial air is crucial. We focus on the air phase: The pressures above and below the bed are measured during and after the collapse and subsequently connected to a one-dimensional diffusion model to understand the behavior of the air inside the sand.

3.2 Experiment

The common way to compactify a sand bed is by tapping or shaking the bed. We choose to apply a shock in a controlled way using a metal ball that is connected to a string forming a pendulum, which is attached close to a container filled with sand (see figure 3.1a). By releasing the ball a certain distance (d) from the container wall, the impact strength can be varied.

[†]In the work of Ribière [17] an open container is used and air might play a role, they do however not go into the details of the air influence

The container ($14 \times 14 \times 100$ cm^3) is filled up to height $H = 40$ cm with sand. The sand is polydisperse with sizes ranging from $20 - 60$ μm and a sphericity between 0.2 and 0.6. Pressurized air is blown into the container from below to fluidize the bed. Subsequently, this airflow is very slowly turned off, resulting in a packing fraction of the bed of around 0.41. Using a vacuum pump the pressure P_0 inside the container can be lowered, which is done by slowly pumping out air from above and below the bed, such that the packing of the sand bed is unchanged [9].

The pendulum's mass equals 520 g and is released from a maximum distance of $d = 32$ cm. For every release distance the impact velocity of the ball is measured which ranges from 0.14 to 0.77 m/s leading to an impulse imparted on the container between 0.073 and 0.40 Ns. The velocity with which the shock travels through the sand is of the order of 100 m/s, therefore it would take approximately 1 ms for the shock to reach the other side of the container [18]. As soon as the ball hits the container wall the sand bed starts to collapse, and the level is monitored during the experiment using a high speed camera.

The bed level decreases almost linear with time and takes a typical time of 30 ms to reach its final height H, see figure 3.2a. The collapse time is much larger than the time it takes for the information to travel through the bed, so we can assume a homogeneous bed collapse. For higher impact speeds there are small, damped oscillations visible around this final height, probably caused by a vibration of the whole container after the impact. Larger impact strengths of the ball result, naturally, in a larger drop of the bed (blue filled circles in figure 3.2c) and also the bed height decreases faster (figure 3.2a), indicating a more violent collapse.

During and after the impact the pressure above and below the bed are measured. Both high-speed, differential pressure sensors (SENSIRION SPD600) compare the pressure in the closed off parts of container above or below the bed with an external reservoir that is brought to the same initial ambient pressure (P_0) and then sealed.

As soon as the ball hits the container wall the pressure ΔP_1 above the bed decreases sharply, as indicated by any of the orange lines in figure 3.3a. This happens on a time scale of 30 ms, comparable to the time the bed needs to collapse. The pressure ΔP_2 below the bed (blue lines) increases much slower. After the initial pressure drop (ΔP_1) and rise (ΔP_2) the pressure differences relax back to zero. The different lines in figure 3.3a represent measurements done for various impact strengths. The extrema of both the pressure above and below the bed increase linearly with the height change ΔH –and therefore also with d– whereas the relaxation of total pressure difference over the bed is independent

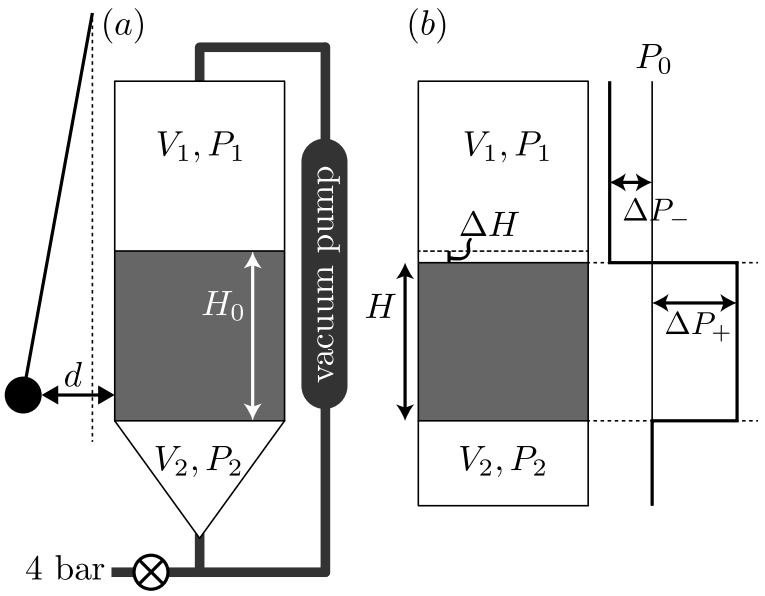

Figure 3.1: (a) Schematic view of the setup used in the experiments. A container filled with sand is fluidized by pressurized dry air from below (4 bar). When the airflow is turned off slowly, the sand settles towards a height H_0. A metal ball attached to a wire is released a distance d from the container, hitting the container wall and collapsing the fragile sand bed. Meanwhile the pressure above (P_1) and below (P_2) the bed are measured with respect to the ambient pressure P_0, which can be lowered using a vacuum pump. (b) To model the effect of the compaction, as an initial condition the sand bed is collapsed over a distance ΔH to a height H, causing a pressure drop above the bed (ΔP_-) and an increase of the air pressure within the bed (ΔP_+). The air in the bed will relax until there is no remaining pressure difference in the setup.

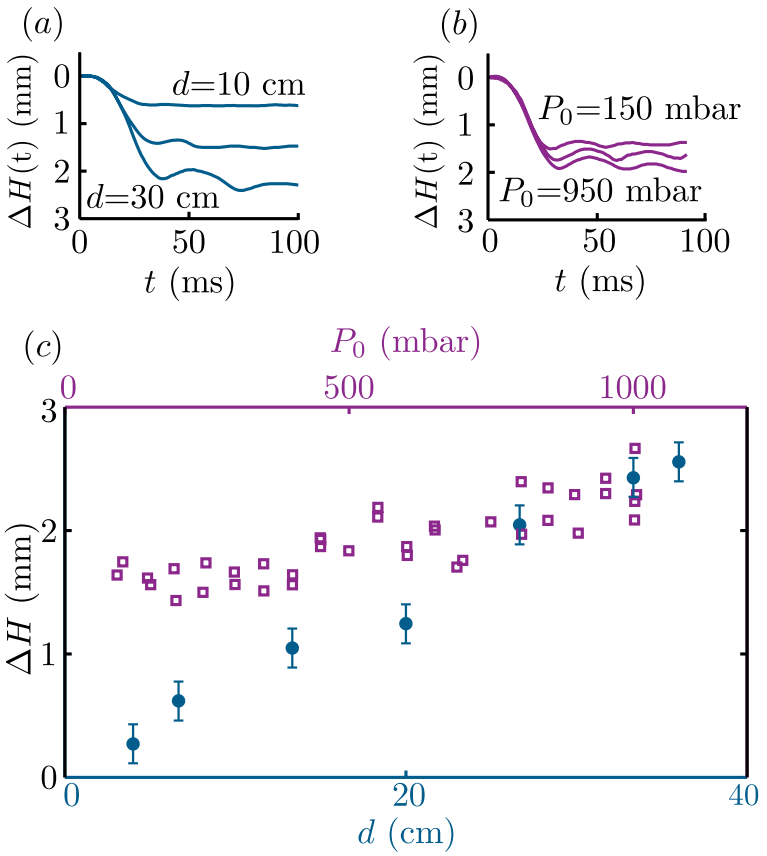

Figure 3.2: (a) The change in bed height $\Delta h(t)$ as a function of time for three different release distances of the ball: $d = 10$ cm, $d = 20$ cm and $d = 30$ cm. Stronger impacts (larger d) result in a more densely packed bed and also in a higher collapse speed (the maximum slope), indicating a more violent collapse. Oscillations are visible for higher impact speeds, caused by a small vibration of the entire container. (b) The bed compaction for experiments with the same release distance ($d = 30$ cm) but at different ambient pressures ($P_0 = 150$, 350, and 950 mbar). The compaction decreases slightly for lower ambient pressures, whereas the collapse speed is constant in this case. (c) The final bed height change ΔH versus d and P_0: ΔH increases linearly with the release distance d of the impacting object (blue (bottom) axis and symbols), whereas the bed compaction is slightly less for lower ambient air pressures P_0 in the container (purple (top) axis and symbols).

of the impact speed. The inset in figure 3.3a shows the signal above the bed just after a strong impact ($d = 30$ cm). There are clear fluctuations visible that correlate with the oscillations of the container and the sand bed height.

In the second set of experiments the impact strength is kept at the constant, high value of $d = 30$ cm, but the container is brought to lower ambient pressures. The change in bed height is plotted as a function of ambient pressure in figure 3.2c (purple squares). From this we find that the bed collapses slightly less for lower ambient pressures, while the collapse speed is independent of the pressure, as can clearly be seen from figure 3.2b.

The magnitude of the differential pressure signals (both above and below the bed) decreases significantly for lower ambient pressures: The pressure drop above the bed is less, and also the maximum pressure reached below the bed decreases. A big difference with results obtained from varying the shock strength lies in the time constant of the relaxation: In figure 3.3b a log-lin plot of the total pressure difference $\Delta P \equiv \Delta P_2 - \Delta P_1$ over the bed for measurements performed at different ambient pressures is shown. Over a fairly large time interval the signals are linear, indicating an exponential decay. The line bends at the end because the container is never perfectly airtight, causing a slight increase in the container pressure during the experiment. In addition the sensors are leaking air into the reservoir due to the measurement method, which also contributes to this effect. The slope decreases when lowering the ambient pressure, indicating a higher relaxation time constant.

3.3 Model

We will now analyze the above results with a model which is based on Darcy's law: The starting point is a sand bed of height H_0 with a certain initial packing fraction ϕ_0. During the very fast collapse of the bed over a distance ΔH to a new height H and packing fraction ϕ the air has no time to leave the bed and is therefore trapped within the sand. From the experiments we learn that this is a good assumption, because the bed collapses in typically 30 ms, whereas other pressure variations occur in the time scale of seconds. When the bed collapses the packing fraction of the sand increases, and the pressure of the air within the sand has to rise to a value ΔP_+, since it is confined to a smaller volume. As a consequence, since the volume above the sand increases it drops to a value ΔP_-. Quantitatively, since the interstitial volume decreases from $(1-\phi_0)H_0A$ to $(1-\phi)HA$ and the total volume occupied by the sand particles remains the same

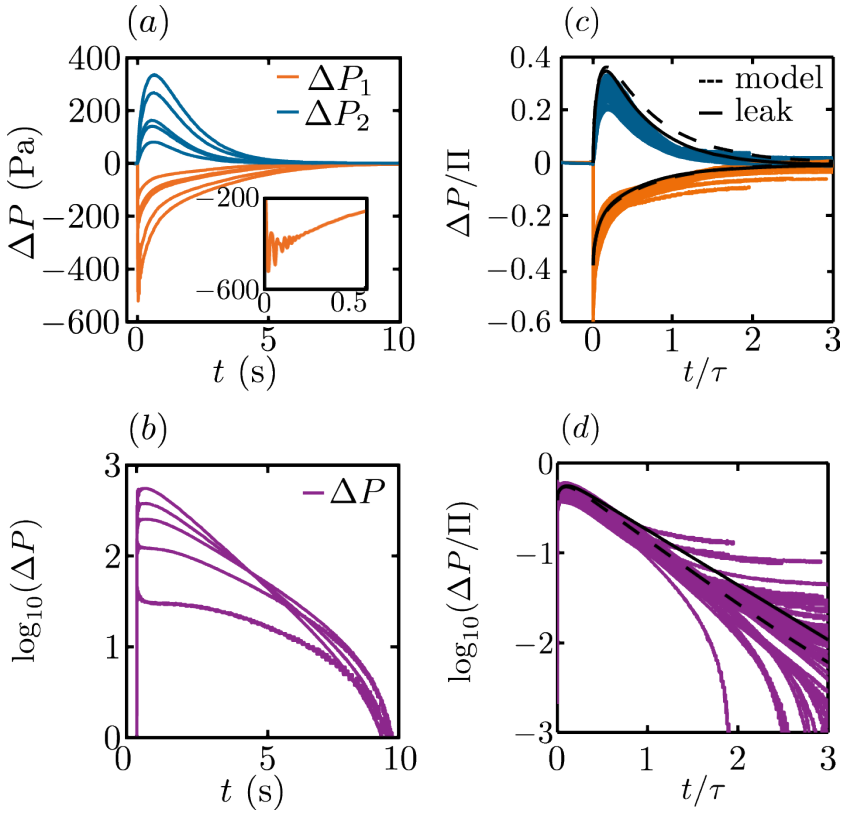

Figure 3.3: (a) The orange curves show the pressure change ΔP_1 in the container above the bed as a function of time for different values of the release distance ($d = 10$, 15, 20, 25, and 30 cm). After a rapid decrease ΔP_1 exponentially relaxes back to zero. The blue lines represent the pressure ΔP_2 below the bed for the same values of d. First, air flows in from the collapsed bed, it reaches a maximum and subsequently relaxes back to zero. Inset: When zooming in on ΔP_1 for $d = 30$ cm we see oscillations upon impact, that correlate with those in figure 3.2a. (b) The logarithm of the pressure difference $\Delta P = \Delta P_2 - \Delta P_1$ over the entire bed for different ambient pressures ($P_0 = 200$, 400, 600, 800 and 1000 mbar). There is an intermediate exponential decay where the relaxation time increases for lower ambient pressure (see text). (c) Dimensionless pressure change $\Delta P_{1,2}/\Pi$ as a function of dimensionless time t/τ including all curves in (a, b). The data collapses nicely onto a single curve. The dashed and solid black lines represents the dimensionless model without and with corrections for the sensor leak respectively. There is a very good agreement without any free parameter. (d) This figure shows the logarithm of the dimensionless pressure difference $(\Delta P_2 - \Delta P_1)/\Pi$ versus t/τ, again in comparison to the model.

($\phi_0 H_0 A = \phi H A$), ΔP_+ and ΔP_- are (to linear order in ΔH)

$$\Delta P_+ = P_0 \frac{\Delta H}{(1-\phi)H}\,; \quad \Delta P_- = -P_0 \frac{A\Delta H}{V_1}\,, \tag{3.1}$$

where V_1 is the volume above the collapsed sand bed. In the non-changing volume below the bed the pressure remains initially ambient. These initial conditions are illustrated in figure 3.1b.

The factor that limits the dynamics is the slow flow of the air inside the sand bed, which we assume to be governed by Darcy's law $\vec{q} = -(\kappa/\mu)\nabla P$, where $\vec{q}$ is the volume flux, $\kappa \approx 5.5 \cdot 10^{-12}$ m^2 is the (measured) permeability of the sand bed [‡] and $\mu = 1.98 \cdot 10^{-5}$ Pa·s is the dynamic viscosity of air. Combining Darcy's law with the ideal gas law and linearizing around P_0 leads to a diffusion equation for the pressure difference ΔP_s inside the sand

$$\frac{\partial \Delta P_s}{\partial t} = D\,\nabla^2(\Delta P_s)\,, \tag{3.2}$$

where the diffusion coefficient is given by $D = \kappa P_0/(\mu(1-\phi))$. We assume the surface of the bed remains flat during the collapse and neglect the effect of the walls of the container such that this problem can be described by a one-dimensional form of equation (3.2) for $\Delta P_s(z,t)$.

This equation needs to be supplemented by mass conservation in the top and bottom part of the container (with volume V_2)

$$\begin{aligned} \frac{d\Delta P_1}{dt} &= -\frac{A}{V_1}\frac{\kappa P_0}{\mu}\left.\frac{\partial \Delta P_s}{\partial z}\right|_{z=H}\,, \\ \frac{d\Delta P_2}{dt} &= \frac{A}{V_2}\frac{\kappa P_0}{\mu}\left.\frac{\partial \Delta P_s}{\partial z}\right|_{z=0}\,, \end{aligned} \tag{3.3}$$

together with the initial conditions from equation (3.1): $\Delta P_1(0) = \Delta P_-$, $\Delta P_s(z,0) = \Delta P_+$, and $\Delta P_2(0) = 0$.

As is shown in the appendix 3.5, this initial boundary value problem can be non-dimensionalized using the bed height $\zeta \equiv H$, the diffusion time $\tau \equiv H^2/D$ and the initial pressure in the sand bed $\Pi \equiv \Delta P_+$ as the typical length, time and pressure scale respectively, leaving us with a problem that contains two parameters only:

$$\alpha \equiv \frac{(1-\phi)AH}{V_1} \approx 0.39\,; \quad \beta \equiv \frac{V_1}{V_2} \approx 4.0\,, \tag{3.4}$$

[‡]The bed permeability (κ) could be estimated using the Carman-Kozeny relation, but was also obtained directly in the current experimental setup by measuring the pressure drop over the bed while a constant flow rate was applied through it.

which are the ratio of the interstitial volume within the collapsed sand bed to that above it and the ratio of the volumes above and below the bed respectively. Most importantly, since $\Delta H \lessapprox 4$ mm is much smaller than $H = H_0 - \Delta H \approx 400$ mm, both α and β are fixed, such that there is no free parameter in this problem.

Now, first we rescale the experiments of figures 3.3a and b using the pressure and time scales τ and Π, the result of which is plotted in figure 3.3c. Indeed all measurements (for various shock strengths and different ambient pressures) collapse onto a single master curve. The variation largely originates from the difficult measurement of ΔH where the height decrease of the entire bed has to be estimated from its decrease along one of the side walls. In addition, given that for every experiment the sand bed has to be prepared separately, slight deviations in the final state cause part of the variation. Curves that don't tend to zero but to a constant correspond to experiments at very low ambient pressure, where likely some air was leaking into the container during the measurements.

In figure 3.3d it can be observed that also the decay behavior of figure 3.3c is neatly collapsed. This can be traced back to the diffusion time $\tau = H^2/D = (1-\phi)\mu H^2/(\kappa P_0)$, which increases inversely proportional to the ambient pressure P_0 in the container.

Secondly we numerically solve the dimensionless initial boundary value problem corresponding to equations (3.1)-(3.3) and compare it to the experiments. This leads to the black dashed line in figure 3.3c. Both above and below the bed the agreement is quite good. Especially the starting value ΔP_- of ΔP_1 and the maximum in ΔP_2 are nicely predicted. The time scale of the relaxation below the bed however seems to be slightly underestimated by the model (figure 3.3c). This can be traced back to the fact that the sensors are leaky [§]. This leak is readily incorporated into the model by adjusting the mass balance of equations (3.3), leading to a much better agreement, solid line in figure 3.3c.

3.4 Conclusion

We studied the response of a sand bed during a single compaction event. We found that applying a stronger shock (larger velocity of impacting object) compactifies the bed more and faster. The collapse of the bed decreases the pressure above the bed almost instantly whereafter, on a much larger time scale, the air slowly flows

[§]According to the manufacturer the sensors leak 150 ml/min at full scale due to the measurement method, which uses a flow rate measurement to obtain the pressure drop over a capillary. This method is faster and more accurate than others, but introduces a small leak. The incorporation of this leak into the model is discussed in the supplementary material.

back through the bed into the upper container. The pressure below the bed is initially unchanged, but excess pressure of the interstitial air inside the bed causes it to increase. After it reaches a maximum the pressure will decrease until there is no pressure change left in the bed. The magnitude of the pressure signals in the container increase linearly with the change in bed height caused by stronger shocks.

By varying the pressure of the air in the bed before the experiment we obtain a better understanding of the influence of air in this problem. Reducing the initial pressure decreases the measured pressure differences above and below the bed, and increases the time it takes for the buildup pressure difference to decay. All pressure observations are accounted for by a model based on Darcy's flow inside the sand bed.

We observed a small but measurable increase of compaction of the sand bed for increasing ambient air pressures, which is counter-intuitive: If pressure-driven forces in the air were counteracting compaction, then they would be increasing linearly with P_0, and thus lead to a compaction decrease in disagreement with what we measure. So how can the presence of air amplify the compaction process?

Part of the answer could lie in air working as a lubrication layer between the particles. Friction between the grains eventually stops the grains from falling down and helps it to form a new packing. In a tilt table experiment we have measured the angle θ at which the sand started to flow (angle of repose) at atmospheric pressure and at 100 mbar, both after the fluidization procedure. We measured $\theta = 15.8 \pm 0.9^\circ$ for 1 bar, and $\theta = 18.5 \pm 0.8^\circ$ for 100 mbar. For low ambient pressure the grains start to flow at a higher angle indicating a larger friction between the sand grains when there is very little air. This is in agreement with the larger collapse for high ambient pressures: If air reduces the friction between the grains, they will be slowed down less and therefore the bed will be more compactified when the grains have found their final position. The precise mechanism by which this happens remains to be elucidated.

References

[1] M. Mobius, X. Cheng, G. Karczmar, S. Nagel, and H. Jaeger, *Intruders in the dust: Air-driven granular size separation*, Phys. Rev. Lett. **93**, 198001 (2004).

[2] M. Faraday, *On a peculiar class of acoustical iňĄgures; and on certain forms assumed by groups of particles upon vibrating elastic surfaces*, Philos. Trans. R. Soc. London **52**, 299 (1831).

[3] H. Pak, E. van Doorn, and R. Behringer, *Effects of ambient gases on granular-materials under vertical vibration*, Phys. Rev. Lett. **74**, 4643 (1995).

[4] T. Shinbrot and F. Muzzio, *Reverse buoyancy in shaken granular beds*, Phys. Rev. Lett. **81**, 4365 (1998).

[5] H. J. van Gerner, M. A. van der Hoef, D. van der Meer, and K. van der Weele, *Interplay of air and sand: Faraday heaping unravelled*, Phys. Rev. E **76**, 051305 (2007).

[6] E. Chladni, *Die Akustik*, Breitkopf & Haertel, Leipzig (1802).

[7] H. J. van Gerner, K. van der Weele, M. A. van der Hoef, and D. van der Meer, *Air-induced inverse Chladni patterns*, J. Fluid Mech. **689**, 203 (2011).

[8] J. Royer, E. Corwin, A. Flior, M. Cordero, M. Rivers, P. Eng, and H. Jaeger, *Formation of granular jets observed by high-speed X-ray radiography*, Nature Phys. **1**, 164 (2005).

[9] G. Caballero, R. Bergmann, D. van der Meer, A. Prosperetti, and D. Lohse, *Role of air in granular jet formation*, Phys. Rev. Lett. **99**, 018001 (2007).

[10] G. A. Caballero-Robledo, K. P. D. Kelly, T. A. M. Homan, J. H. Weijs, D. van der Meer, and D. Lohse, *Suction of splash after impact on dry quick sand*, granular matter **14**, 179 (2012).

[11] J. B. Knight, C. G. Fandrich, C. N. Lau, H. M. Jaeger, and S. R. Nagel, *Density relaxation in a vibrated granular material*, Phys. Rev. E **51**, 3957 (1995).

[12] E. Nowak, J. Knight, M. Povinelli, H. Jaeger, and S. Nagel, *Reversibility and irreversibility in the packing of vibrated granular material*, Powder Technol. **94**, 79 (1997).

[13] T. Boutreux and P. deGennes, *Compaction of granular mixtures: A free volume model*, Physica A **244**, 59 (1997).

[14] E. Ben-Naim, J. Knight, E. Nowak, H. Jaeger, and S. Nagel, *Slow relaxation in granular compaction*, Physica D **123**, 380 (1998).

[15] S. Linz and A. Dohle, *Minimal relaxation law for compaction of tapped granular matter*, Phys. Rev. E **60**, 5737 (1999).

[16] P. Richard, M. Nicodemi, R. Delannay, P. Ribiere, and D. Bideau, *Slow relaxation and compaction of granular systems*, Nat. Mater. **4**, 121 (2005).

[17] P. Ribiere, P. Philippe, P. Richard, R. Delannay, and D. Bideau, *Slow compaction of granular systems*, J. Phys. Condens. Matter **17**, S2743 (2005).

[18] C. Liu and S. Nagel, *Sound in a granular material: Disorder and nonlinearity*, Phys. Rev. B **48**, 15646 (1993).

3.5 Appendix: Derivation of the model.

In this appendix we derive the model based on Darcy's law that has been used in the main text of chapter 3. In doing so we assume that the compaction of the bed will have occurred uniformly, leading to a uniform compression of the air within the pores between the sand grains and that as a result flow will take place in the vertical (z-)direction only.

3.5.1 Linearized porous media equation

For an infinitesimally small cube of sand of volume ($dV = dx\,dy\,dz$) the mass balance equation for a one-dimensional flow in the z-direction reads

$$\frac{dm}{dt} = \rho Q_z - \rho Q_{z+dz}\,, \tag{3.5}$$

where ρQ_z and ρQ_{z+dz} give the in- and outflow at the bottom and the top of the volume. Here, the air density ρ may vary with pressure. The in- and outflow can be calculated using Darcy's law, which describes the flow through a porous medium

$$\vec{Q} = -A\frac{\kappa}{\mu}\nabla P_s\,, \tag{3.6}$$

where A is the area perpendicular to the flow, in this case $dxdy$, κ is the permeability of the porous material, μ the viscosity of the flowing medium, in our case air, and P_s the pressure of the air in the control volume. Replacing the flows in equation (3.5) and expanding around z leads to

$$\frac{dm}{dt} = \frac{\kappa}{\mu}\frac{\partial}{\partial z}\left[\rho\frac{\partial P_s}{\partial z}\right] dV\,. \tag{3.7}$$

The volume of air in the cube depends on the packing fraction ϕ of the porous material. If we assume that the packing fraction is not changing we can rewrite the left had side of equation (3.5) as

$$\frac{dm}{dt} = (1-\phi)\,\frac{\partial \rho}{\partial t}\,dV\,. \tag{3.8}$$

From the ideal gas law we know that $\rho = P/(RT)$, such that we can replace the density in equations (3.7) and (3.8) with P. Assuming that the temperature T is constant, owing to the good thermal contact of the gas with the porous media which has a relatively large heat capacity, this then leads to

$$\frac{\partial P_s}{\partial t} = \frac{\kappa}{2\mu\,(1-\phi)}\frac{\partial^2 P_s^2}{\partial z^2}\,, \tag{3.9}$$

which is the well-known porous media equation in the limit we are discussing now. Writing P_s as a constant ambient pressure plus a small pressure difference ($P_s = P_0 + \Delta P_s$) and linearizing around P_0 leads to a diffusion equation for flow in a porous material

$$\frac{\partial \Delta P_s}{\partial t} = \frac{\kappa P_0}{\mu(1-\phi)} \frac{\partial^2 \Delta P_s}{\partial z^2}, \tag{3.10}$$

with diffusivity $D \equiv \kappa P_0/(\mu(1-\phi))$.

3.5.2 Initial conditions after bed collapse

The diffusion equation describes the dynamics of the air in the sand in the presence of pressure gradients. For the current problem these gradients arise from the collapse of the bed, as a result of which the pressure above the bed decreases and the pressure inside the bed increases. The volume occupied by the sand grains is constant which, if we assume the bed to compactify homogeneously, relates the packing fraction before (ϕ_0) and after the collapse (ϕ) as

$$\phi = \phi_0 \frac{H_0}{H} = \phi_0 \frac{H + \Delta H}{H}, \tag{3.11}$$

where H_0 and $H = H_0 - \Delta H$ are the bed height before and after collapse respectively. The interstitial volume changes from $(1-\phi_0)AH_0$ before to $(1-\phi)AH$ after collapse, with A the cross-sectional area of the container. Now, assuming that the collapse of the bed is so fast that air has no time to escape, the (isothermal) ideal gas law has to be satisfied before and after the collapse:

$$(1-\phi_0)AH_0P_0 = (1-\phi)AH(P_0 + \Delta P_+). \tag{3.12}$$

Combining relations (3.11) and (3.12), leads to an equation for the initial pressure rise ΔP_+ inside the bed:

$$\Delta P_+ = \frac{P_0 \Delta H}{(1-\phi)H} \tag{3.13}$$

Simultaneously, the pressure P_1 in the container volume V_1 above the bed will decrease by an amount ΔP_- due to an increase in the volume: $P_1V_1 = (P_1 + \Delta P_-)(V_1 + A\Delta H)$. Up to linear order in $\Delta H/H$ this leads to

$$\Delta P_- \approx -\frac{A\Delta H}{V_1} P_0, \tag{3.14}$$

where we have used that the volume of the top part of the container is of the order of the total volume of the sand bed ($V_1 \sim AH$). Finally, the pressure P_2 below the bed will not change during the collapse ($\Delta P = 0$). The initial conditions are illustrated in the right half of figure 3.1b.

3.5.3 Boundary conditions

Now that we have introduced a pressure difference in the setup, the pressure will be equalized by air moving from the sand bed into the top and bottom part of the container. Using Darcy's law (equation (3.6)), the time rate of change of the amount of air in the volume above the bed is proportional with the inflow

$$\frac{dm}{dt} = \rho Q = -\rho A \frac{\kappa}{\mu} \left. \frac{\partial P_s}{\partial z} \right|_{z=H}, \tag{3.15}$$

and proportional to the rate of change of the density given that the volume (V_1) stays constant

$$\frac{dm}{dt} = \frac{\partial}{\partial t}(\rho V) = V \frac{d\rho}{dt}. \tag{3.16}$$

Combining equations (3.15) and (3.16) with the isothermal ideal gas law $\rho = PRT$ and linearizing $P = P_0 + \Delta P$ around P_0 leads to the boundary condition at the top of the sand bed

$$\frac{d\Delta P_1}{dt} = -\frac{A}{V_1} \frac{\kappa P_0}{\mu} \left. \frac{\partial \Delta P_s}{\partial z} \right|_{z=H}. \tag{3.17}$$

For the container volume V_2 below the sand bed we find similarly that

$$\frac{d\Delta P_2}{dt} = \frac{A}{V_2} \frac{\kappa P_0}{\mu} \left. \frac{\partial \Delta P_s}{\partial z} \right|_{z=0}. \tag{3.18}$$

3.5.4 Non-dimensionalization

To non-dimensionalize the above set of equation we define a typical length, time and pressure scale as

$$\begin{aligned} \zeta &= H, \\ \tau &= \frac{H^2}{D} = \frac{\mu(1-\phi)H^2}{\kappa P_0}, \\ \Pi &= \Delta P_+ = \frac{P_0 \Delta H}{(1-\phi)H}, \end{aligned} \tag{3.19}$$

such that we can rewrite the boundary value problem consisting of equations (3.10), (3.13), (3.14), (3.17), and (3.18) in terms of the non-dimensional variables $\widetilde{z} = z/\zeta$, $\widetilde{t} = t/\tau$, and $\Delta\widetilde{P} = \Delta P/\Pi$. This leads to the following partial differential equation

$$\frac{\partial \Delta \widetilde{P}_s}{\partial \widetilde{t}} = \frac{\partial^2 \Delta \widetilde{P}_s}{\partial \widetilde{z}^2}, \tag{3.20}$$

together with the initial conditions

$$\begin{aligned} \Delta\widetilde{P}_s(z,0) &= 1, \\ \Delta\widetilde{P}_1(0) &\approx -\alpha, \\ \Delta\widetilde{P}_2(0) &= 0, \end{aligned} \tag{3.21}$$

and the boundary equations

$$\begin{aligned} \frac{d\Delta\widetilde{P}_1}{d\widetilde{t}} &= -\alpha \left.\frac{\partial\Delta\widetilde{P}_s}{\partial\widetilde{z}}\right|_{\widetilde{z}=1}, \\ \frac{d\Delta\widetilde{P}_2}{d\widetilde{t}} &= \alpha\beta \left.\frac{\partial\Delta\widetilde{P}_s}{\partial\widetilde{z}}\right|_{\widetilde{z}=0}. \end{aligned} \tag{3.22}$$

This set of equations contains two parameters only, α and β, which are the ratio of the free volume within the sand to V_1 and the ratio of the volumes above and below the bed respectively

$$\alpha = \frac{(1-\phi)AH}{V_1}\,; \quad \beta = \frac{V_1}{V_2}\,. \tag{3.23}$$

From the dimensions of the setup both are readily computed. Using $V_1 = 1.22 \cdot 10^{-2}$ m^3, $V_2 = 3.05 \cdot 10^{-3}$ m^3, $A = 2.03 \cdot 10^{-2}$ m^2, $H = 0.40$ m and $\phi = 0.42$ we find $\alpha = 0.39$ and $\beta = 4.0$. This fixes the (numerical) solution of the boundary value problem completely.

3.5.5 Corrections

The effect of the porous plate can be incorporated into the equations with the introduction of three additional dimensionless parameters, namely the dimensionless thickness of the plate $\widetilde{h}_p = h + p/H$, the ratio γ of the permeabilities of the sand and plate ($\gamma = \kappa/\kappa_p$), and the ratio δ of the porosities of sand and plate ($\delta = (1-\phi)/(1-\phi_p)$). For realistic values of the parameters this however leads to minor corrections in the numerical solution to the boundary value problem.

A more significant correction stems from the fact that the (SENSIRION SPD600) pressure sensors that were used are leaky due to the measurement method they are based on, which uses a flow rate measurement to obtain the pressure drop over a capillary. According to the manufacturer the sensors leak 150 ml/min ($= 2.5 \cdot 10^{-6}$ m^3/s at full scale (± 500 Pa)), which leads to a volume flow rate $Q_{\text{leak}} = -\sigma\Delta P_i$ with $\sigma = 5.0 \cdot 10^{-9}$ m^3/Pa·s for both the top ($i = 1$) and bottom

($i = 2$) part of the container. This leads to a modification of equation (3.15): $dm/dt = \rho Q + \rho Q_{\mathrm{leak}}$, the incorporation of which finally amounts to the addition of a term to both boundary conditions (3.17) and (3.18) which in dimensionless form reads

$$\frac{d\Delta\widetilde{P}_1}{d\widetilde{t}} = -\alpha \left.\frac{\partial\Delta\widetilde{P}_s}{\partial\widetilde{z}}\right|_{\widetilde{z}=1} - \lambda\Delta\widetilde{P}_1\,,$$
$$\frac{d\Delta\widetilde{P}_2}{d\widetilde{t}} = \alpha\beta \left.\frac{\partial\Delta\widetilde{P}_s}{\partial\widetilde{z}}\right|_{\widetilde{z}=0} - \lambda\beta\Delta\widetilde{P}_2\,, \tag{3.24}$$

with

$$\lambda = \frac{\tau P_0}{V_1}\,; \quad \sigma = \frac{\mu(1-\phi)H^2}{\kappa V_1}\,\sigma\,. \tag{3.25}$$

Again, λ is not a free parameter but is completely fixed by measurable properties of the experiment. Using $\kappa \approx 5.5 \cdot 10^{-12}$ m^2, $\mu = 1.98 \cdot 10^{-5}$ Pa·s, $H = 0.40$ m, $V_1 = 1.22 \cdot 10^{-2}$ m^3, and $\phi = 0.42$, we find $\lambda = 0.14$

4

Air entrapment during the impact of a ball on sand *

When a ball impacts on a very loose bed of sand a pressure difference over the bed is created. The pressure signal above the bed has a very characteristic shape with features corresponding to the creation of a cavity behind the ball and the collapse of this cavity. The initial decrease of the pressure during the creation of the cavity demonstrates that the sand in front of the ball must compactify while the low diffusive time scale traps the air in the bed. A plateau in the signal, during which the pressure does not change with time, indicates the existence of an equilibrium between the creation of the cavity and air diffusing around the ball back into the cavity. The amount of air that is being trapped in the bed during this initial phase increases with impact velocity and decreases with ambient pressure.

4.1 Introduction

Granular materials are found everywhere in nature and are of great importance in industrial applications. The transport of granular materials poses many problems because in some cases it behaves like a fluid, while in others it resembles a solid

*To be submitted as: Tess Homan, Sylvain Joubaud, Detlef Lohse, and Devaraj van der Meer, "Air entrapment during the impact of a ball on sand".

(*e.g.*, when sand jams in a funnel). To better understand its behavior much research has been done on granular flows [1–3]. A very important aspect in granular flows which is much less researched is the role of the interstitial fluid. A well-known example of such a problem is the brazil-nut effect, where, counter-intuitively, large grains end up on top of small grains when a mixture is shaken [4–7]. Here, the influence of air can be as big as to change the direction of motion of the large grains [5, 6].

Air plays a particularly important role during the impact of a solid object on a loosely packed granular bed, consisting of particles with a diameter ≤ 200 μm. In such a bed the events occurring after the object hits the sand are quite similar to what would happen in a liquid [8–14]. Behind the object an air cavity is created, which collapses due to gravity driven "hydrostatic" pressure. This focussing of energy leads to a vigorous jet shooting upward. The remainder of the cavity that was below the pinch-off slowly rises to the surface, similar to an air bubble in liquid, and causes an eruption.

The influence of air in this problem has been studied by Caballero *et al.* [15] and Royer *et al.* [16] by dropping a ball in sand at various ambient pressures. They found, among other things, a considerably smaller jet for lower pressures, which they were able to trace back to a considerable increase of the drag the ball experiences in that regime. In order to explain this behavior Caballero *et al.* postulated a mechanism where air is pushed in front of the moving ball creating an airflow which fluidizes the sand, reducing the drag on the ball and allowing for deeper penetration [15]. At lower ambient pressure this fluidization process is weaker, thus leading to an increase of the drag on the ball which is found to scale roughly as $P_0^{-1/2}$. Royer *et al.* found that interstitial air prevents compaction at higher pressures, resulting in a liquid-like (incompressible) behavior of the sand bed [16–19].

Experimentally measuring the airflow associated with the ball within the sand directly is barely feasible, so in this chapter we take a different approach and measure the airflow indirectly. We do this by conducting detailed pressure measurements below and above the sand bed performed during an impact event, under various ambient pressures and for various impact speeds. These pressure measurements will then be related to the airflow inside the sand bed, where we will concentrate on that stage of the process corresponding to the penetration of the ball into the bed.

4.2 Experimental setup

The setup, a container with a porous bottom plate, is filled with sand (grain size 20-60 μm) until height H=40 cm (see figure 4.1). Next, pressurized air is blown in from below which fluidizes the sand. By slowly turning off the air-flow the sand settles in a very loose packing (packing fraction ~ 0.41) [15]. Two differential pressure sensors (SENSIRION SPD600) are mounted at the top and bottom of the container and an external reservoir is placed in parallel with the container. With a vacuum pump the container and the reservoir are slowly brought to the desired ambient pressure and the valves are closed. A steel ball with a diameter D of 16 mm is dropped from a variable height h above the sand bed using a pneumatic release mechanism, changing the Froude number (Fr$= 2U^2/gD$, with U the impact velocity of the sphere) between 10 and 140. The pressure differences between the reservoir and the volumes above and below the bed are recorded during the fall and impact of the ball. At the same time the events above the surface are recorded using a high speed camera (PHOTRON Fastcam SA1.1) such that they can be related to the pressure signal and the exact moment of impact can be determined.

The inset in figure 4.2 shows, for a single measurement, the complete pressure signal above (purple line) and below (green line) the bed. Here we see that, with respect to the ambient pressure P_0, the pressure ΔP_{top} in the top of the container quickly drops immediately after impact (t=0) and then very slowly returns to 0 Pa. The pressure $\Delta P_{\mathrm{bottom}}$ *below* the bed only starts to slowly increase at $t \approx 60$ ms, reaches a maximum at $t \approx 2$s and after that relaxes back to zero again. For large time scales the global shape is very similar to the pressure signals we measured after collapsing a pre-fluidized sand bed by hitting the outside of the container in chapter 3 [20]. When we zoom in on the first 250 ms of the pressure signal above the bed however we observe a characteristic shape of the curve which we can relate to different stages during the impact. Upon impact of the ball, the pressure first decreases (I in figure 4.2), but surprisingly within 20 ms reaches a relatively flat region, a plateau, while the ball continues to move into the sand (II). After 50 ms there is a second, larger, pressure drop, which coincides with the cavity collapse and jet formation (III).

4.3 Initial pressure change

The main issue we need to address now is what precisely determines the shape of the pressure signal. To answer this question we first turn to establishing what

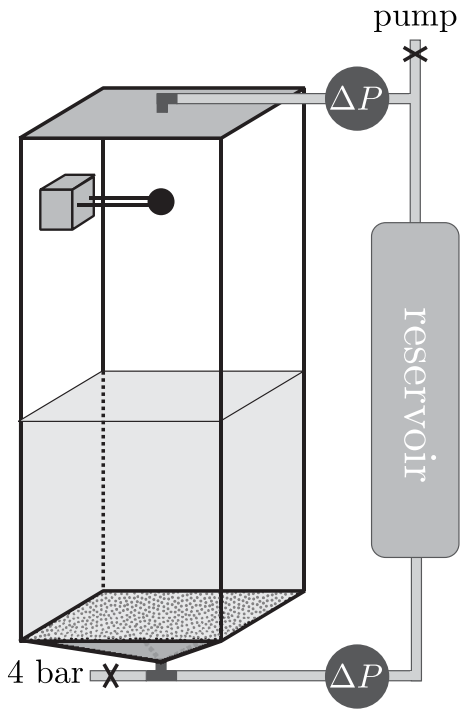

Figure 4.1: Experimental setup used in the impact experiments. The setup consists of a container ($14 \times 14 \times 100$ cm^3) filled with very fine sand. The bottom is made of a porous material allowing pressurized air to be blown into the container from below, while keeping the sand in. If this airflow is turned off, the sand settles in a very loose state with a height H above the porous plate. With a vacuum pump the whole system including an external reservoir can subsequently be brought to the desired ambient pressure. Using a pneumatic release mechanism a metal ball is dropped from a certain height above the sand. During the impact the pressure above and below the sand with respect to the reservoir is measured. The impact event is simultaneously recorded using a high speed camera

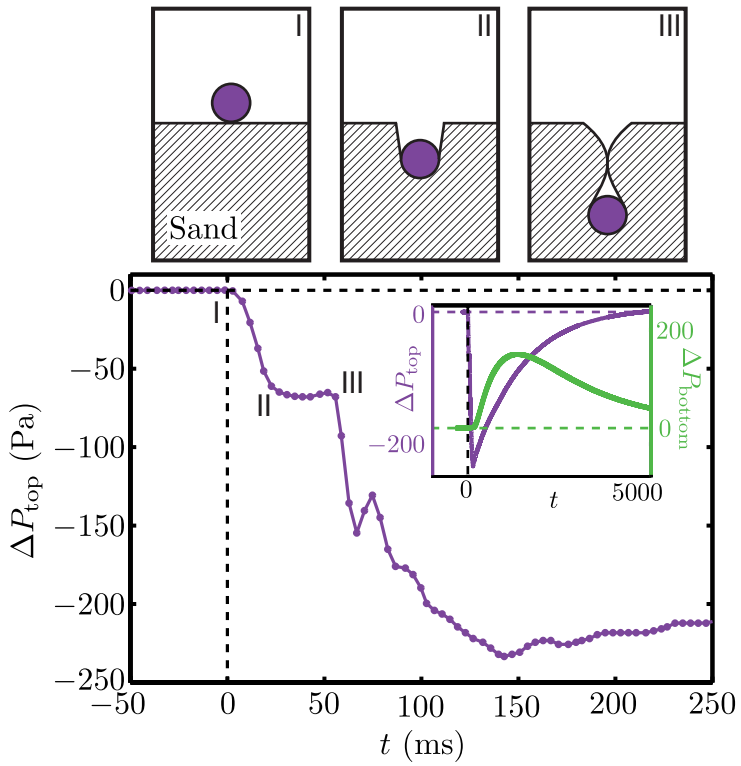

Figure 4.2: Pressure signal during impact. The plot shows the pressure signal above the bed ΔP_{top} at short time scales around the impact. The inset gives the whole signal above (purple line, left axis) and below $\Delta P_{\mathrm{bottom}}$ (green line, right axis) the bed. The three drawings provide a schematic view of the sand bed at times marked I, II, and III in the main graph.

mechanism actually causes the pressure to drop in the first place: If, upon impact, the sand bed would behave as an incompressible fluid, the volume of sand should remain constant in time. Conversely, this is necessarily also true for the volume of air within the (closed) upper container and as a result the pressure above the sand should remain unchanged. When, in contrast, the sand bed compresses, the volume above the sand becomes larger. However, this volume increase is compensated by the decrease of interstitial volume within the sand, and, as long as air is able to flow out of the sand freely, the pressure would still remain unchanged.

As a direct consequence the pressure above the bed can only change if air gets trapped inside the sand during the impact experiment, and is not able to escape fast enough on the relevant time scale. The way this entrapment is realized maybe either active, when the ball pushes air into the sand, or passive, when sand is compacted in the process and pressurizes the interstitial air inside the pores.

To get an estimate of the time scales and lengths over which air is trapped in a porous bed we use Darcy's law which governs the flow within the interstitial volume of the sand. Darcy's law relates the airflow through the sand (Q in m^3/s), the viscosity of the air (μ, Pa·s) and the pressure drop (ΔP, Pa) over a certain distance (L in m) by [21, 22]:

$$Q_D = -\frac{\kappa A}{\mu}\frac{\Delta P}{L}, \tag{4.1}$$

where κ is the permeability of the sand and A is the cross-sectional area (m^2) perpendicular to the flow. Combining Darcy's law and the isothermal ideal gas law we get the porous media equation (derived in chapter 3 [20]) from which we find the following diffusion time:

$$t = \frac{L^2 \mu}{\kappa P_0}, \tag{4.2}$$

where P_0 is the ambient pressure. At atmospheric pressure ($P_0 = 1$ bar), the time it would take for the air in the bed to move over a distance of one ball diameter is approximately 10 ms, and the time to cross the entire bed is 6000 ms. So air that is further away from the surface than one ball diameter will be "trapped" during 10 ms after the perturbation. Note that the upper and lower surface of the bed may not be the fastest way for air to move out of the sand, since the cavity also forms a direct connection to the upper container.

In figures 4.3a and b the measured pressure above the bed is shown for impacts at different Froude numbers (Fr) and ambient pressures (P_0). When, for constant P_0, the impact velocity is increased (higher Froude number; figure 4.3a) the

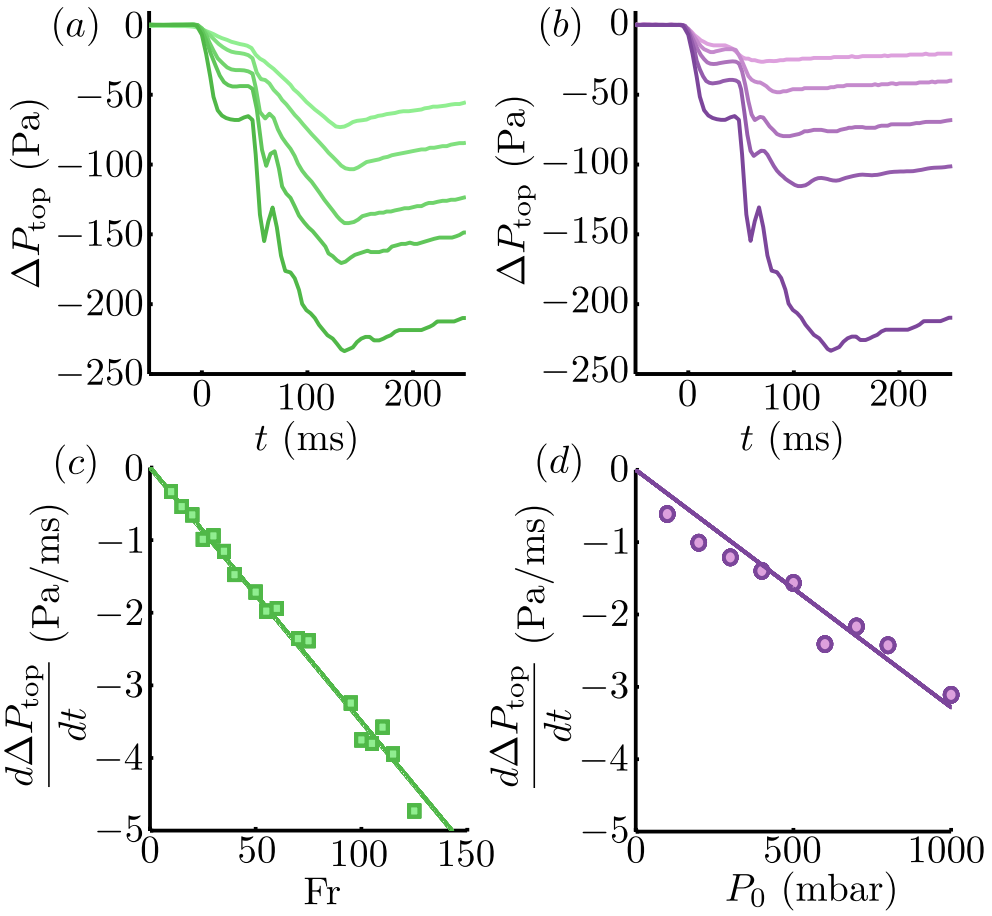

Figure 4.3: (a) The pressure ΔP_{top} measured above the bed for 5 different Froude numbers (Fr) at P_0 =1 bar: From top to bottom Fr=10, 20, 40, 60, and 100. Increasing the impact velocity, and thus the Froude number, results in a larger pressure difference. (b) The five different lines show the pressure signal as a function of time for different ambient pressures (P_0) for Fr=100: P_0 =100, 200, 400, 600, and 1000 mbar. The amplitude of the measured signal is higher for higher ambient pressures. (c,d) The rate of change $d\Delta P_{\mathrm{top}}/dt$ in the pressure above the bed until the plateau is reached (between point I to II in figure 4.2) is plotted as a function of the Froude number (Fr, (c)) and as a function of the ambient pressure (P_0, (d)).

pressure difference increases, leading to a larger pressure drop above the bed. Although the shape of the signal is similar, some differences can be seen. The initial slope of the signal is smaller for low impact speeds and also the onset of the plateau is less abrupt. Furthermore we notice that the "dimple" after the cavity collapse decreases and eventually disappears for low Froude numbers. Figure 4.3b shows signals for different ambient pressures. Again the shape is largely conserved while the magnitude of the signal increases with ambient pressure.

We now concentrate on the pressure drop associated with the penetration of the ball (points I to III in figure 4.2). The slope of the initial pressure decrease ($d\Delta P_{\mathrm{top}}/dt$) is plotted for experiments at different Froude numbers in figure 4.3c and for different ambient pressures in figure 4.3d. As a function of both variables it displays a linear behavior.

With these ingredients we are now able to start to interpret the pressure signal. Suppose that the first decrease in pressure (from I to II in figure 4.2) was purely due to an increase in volume of the upper container connected to the formation of a cylindrical cavity. This must mean that sand is compacted in front of the ball in order to create this extra space, trapping air inside the sand at a rate $dV/dt = \pi R^2 U$. This in turn would lead to a rate of pressure decrease $d\Delta P_{\mathrm{top}}/dt = -P_0/V_{\mathrm{top}}\pi R^2 U \propto R^2 P_0 U$. The linear dependence on P_0 is consistent with the experiment, but the proportionality to U is not: The experiments point to a U^2 relation which may be due to the ball actively pushing air into the sand or to the fact that the cavity expands differently in the radial direction for increasing U. Indeed, there is evidence for this from X-ray experiments (see chapter 2 [23] and [16]) and for the expansion of a water cavity it has been found that the maximal cavity radius scales as $R_{\mathrm{max}} \propto \mathrm{Fr}^{1/4}$ [24]. For our cavity in sand this would lead to $d\Delta P_{\mathrm{top}}/dt \propto R_{\mathrm{max}}^2 P_0 U \propto P_0 U^2$, which is indeed what we observe in figure 4.3c.

4.4 Equilibrium state

The second question we want to address is why there is a plateau in ΔP_{top} while the cavity is still expanding. To this end we look at the time it takes to reach the plateau, $\Delta t_{\mathrm{impact}}$. From the experiments we know that it takes typically 25 ms to reach the plateau and that this time increases for lower ambient pressures and low Froude numbers. This agrees with the diffusion time of air trapped in a compacted region below the ball. The air from this compacted region has to diffuse over a distance of approximately $L = \pi R_{\mathrm{ball}}$ to reach the air cavity, after which the pressure above the bed will increase (see figure 4.2II). We can get the

diffusion time from equation (4.2) which is around 25 ms for atmospheric pressure and increases to 250 ms for measurements done at 100 mbar, consistent with the experiments. So, after a certain time interval $\Delta t_{\mathrm{impact}}$ air is no longer trapped, and an equilibrium is established between air being trapped into the sand and air flowing around the ball into the cavity.

The plateau ends at an abrupt decrease of the pressure (figure 4.3a,b), which from the high-speed recordings is seen to correspond to the cavity collapse and the formation of the jet. The cavity closure is such a violent event that, due to shock waves, the fragile state of the pre-fluidized sand bed is destroyed and the whole bed collapses. As with the impact, this collapse happens so fast that air is trapped in the sand and is prevented from escaping the bed during the increase in the volume above the bed and thus leads to a decrease in the measured pressure [20]. The fact that the pressure below the bed starts increasing immediately with this event, points to a global rather than a local collapse: If the collapse would be local, air would still require in the order of 6000 ms to reach the bottom of the container, making it only possible for $\Delta P_{\mathrm{bottom}}$ to start increasing many seconds after the experiment has started. In contrast, in a global collapse of the entire bed the air pressure will rise everywhere, and air close to the bottom will flow out of the bed driven by this pressure difference.

The end of the plateau is found to be at approximately 55 ms after impact, independent of the ambient pressure and Froude number. This is again consistent with earlier, high-speed imaging measurements of the collapse time [15].

4.5 Volume of trapped air

The final quantity we want to discuss is the amount of air $\Delta V_{\mathrm{trapped}}$ that is trapped in the bed while the ball penetrates into the sand. At first, the trapped volume is increasing, but as soon as the plateau in ΔP_{top} is reached it remains constant, and is given by $\Delta V_{\mathrm{trapped}} = V_{\mathrm{top}} \cdot \Delta P_{\mathrm{plateau}}/P_0$. By measuring $\Delta P_{\mathrm{plateau}}$ we are able to plot $\Delta V_{\mathrm{trapped}}$ as a function of the ambient pressure and the Froude number in figure 4.4. $\Delta V_{\mathrm{trapped}}$ increases linearly with the Froude number, and it has a positive cut-off on the y-axis (figure 4.4a). For higher Froude numbers the ball is moving faster, such that the volume of the cavity that is created, and thus the amount of air that is being trapped before the equilibrating diffusive flow sets in, is larger. Even a ball that impacts with zero impact speed (Fr=0) sinks away into the loose sand, and is therefore capable of trapping air in the sand, consistent with the offset in figure 4.4a [12].

For lower ambient pressures the ball is slowed down more due to the larger

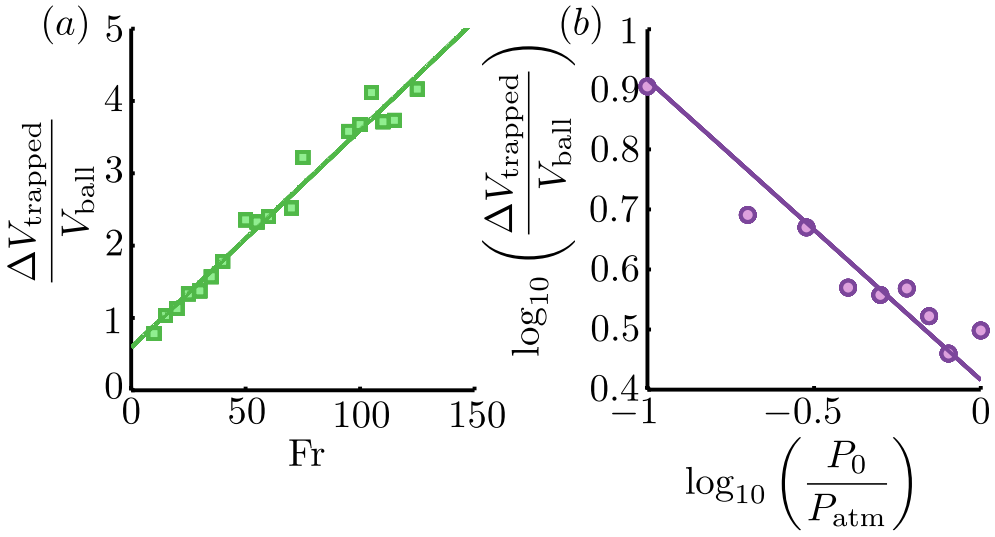

Figure 4.4: Volume of air that is trapped inside the sand during the impact as a function of the Froude number (a) and as a function of the ambient pressure (b). The fitted line in the log-log plot (b) has a slope of -1/2.

drag on the ball. A slower moving ball traps less air than a fast moving ball, as is seen in the experiments at different Froude numbers, but the time it takes air to move around the ball and set up the balancing flow is increased enormously. At 100 mbar the diffusion time is already 10 times longer than at atmospheric pressure. We therefore see that the amount of air that is trapped in the sand for an impact at different ambient pressures goes as $V_{\text{trapped}} \propto P_0^{-1/2}$, indicating a larger volume of air trapped for low ambient pressures. The mass of air that belongs to this V_{trapped} goes as $m_{\text{trapped}} \propto P_0^{1/2}$, which does decrease for low ambient pressures. So the amount of work that can be done by this trapped pressurized air is less for low ambient pressures.

4.6 Conclusion

In conclusion, we obtained insight into the amount of air trapped inside a sand bed by measuring the pressure changes above and below the sand bed. While the ball is moving through the sand it is creating a cavity behind it. During this period the pressure above the bed is decreasing due to an increase in volume, which can only happen if the sand in front of the ball is compacted. While the ball keeps

moving downward and the cavity is still growing the pressure stops decreasing and becomes constant, forming a plateau. This plateau occurs because there is a balance between the growth of the cavity and air flowing out of the bed. The start of this plateau depends on the ambient pressure, but for atmospheric pressure it is around 25 ms. This is the time air needs to diffuse around the ball into the cavity behind it, setting up this equilibrium. The amount of air that is trapped inside the bed during the impact depends on the impact velocity of the ball and on the ambient pressure. For low ambient pressures the volume of trapped air is larger than at atmospheric pressure, but the displaced mass is of course less since the density goes down with pressure. It is plausible that the air that is trapped in front of the ball during the impact is related to the drag increase measured at low ambient pressures by both Caballero *et al.* [15] and Royer *et al.* [16]. The exact mechanism by which the trapped volume of air is able to decrease the drag at atmospheric pressure remains an open question.

References

[1] H. Jaeger, S. Nagel, and R. Behringer, *Granular solids, liquids, and gases*, Rev. Mod. Phys. **68**, 1259 (1996).

[2] H. Jaeger, S. Nagel, and R. Behringer, *The physics of granular materials*, Phys. Today **49**, 32 (1996).

[3] H. Jaeger, *Sand, jams and jets*, Phys. World **18**, 34 (2005).

[4] M. Möbius, B. Lauderdale, S. Nagel, and H. Jaeger, *Brazil-nut effect - Size separation of granular particles*, Nature **414**, 270 (2001).

[5] X. Yan, Q. Shi, M. Hou, K. Lu, and C. K. Chan, *Effects of air on the segregation of particles in a shaken granular bed*, Phys. Rev. Lett. **91**, 014302 (2003).

[6] M. E. Möbius, X. Cheng, G. S. Karczmar, S. R. Nagel, and H. M. Jaeger, *Intruders in the dust: Air-driven granular size separation*, Phys. Rev. Lett. **93**, 198001 (2004).

[7] M. E. Möbius, X. Cheng, P. Eshuis, G. S. Karczmar, S. R. Nagel, and H. M. Jaeger, *Effect of air on granular size separation in a vibrated granular bed*, Phys. Rev. E **72**, 011304 (2005).

[8] A. Worhtington, *A Study of Splashes*, Longman and green, London (1908).

[9] H. Oguz and A. Prosperetti, *Bubble entrainment by the impact of drops on liquid surfaces*, J. Fluid Mech. **219**, 143 (1990).

[10] D. Lohse, *Bubble puzzles*, Phys. Today **56**, 36 (2003).

[11] S. Thoroddsen and A. Shen, *Granular jets*, Phys. Fluids **13**, 4 (2001).

[12] D. Lohse, R. Rauhe, R. Bergmann, and D. van der Meer, *Creating a dry variety of quicksand*, Nature **432**, 689 (2004).

[13] D. Lohse, R. Bergmann, R. Mikkelsen, C. Zeilstra, D. van der Meer, M. Versluis, K. van der Weele, M. van der Hoef, and H. Kuipers, *Impact on soft sand: Void collapse and jet formation*, Phys. Rev. Lett. **93**, 198003 (2004).

[14] S. von Kann, S. Joubaud, G. A. Caballero-Robledo, D. Lohse, and D. van der Meer, *Effect of finite container size on granular jet formation*, Phys. Rev. E **81**, 041306 (2010).

[15] G. Caballero, R. Bergmann, D. van der Meer, A. Prosperetti, and D. Lohse, *Role of air in granular jet formation*, Phys. Rev. Lett. **99**, 018001 (2007).

[16] J. R. Royer, E. I. Corwin, A. Flior, M.-L. Cordero, M. L. Rivers, P. J. Eng, and H. M. Jaeger, *Formation of granular jets observed by high-speed X-ray radiography*, Nat. Phys. **1**, 164 (2005).

[17] J. R. Royer, E. I. Corwin, P. J. Eng, and H. M. Jaeger, *Gas-mediated impact dynamics in fine-grained granular materials*, Phys. Rev. Lett. **99**, 038003 (2007).

[18] J. R. Royer, E. I. Corwin, B. Conyers, A. Flior, M. L. Rivers, P. J. Eng, and H. M. Jaeger, *Birth and growth of a granular jet*, Phys. Rev. E **78**, 011305 (2008).

[19] J. R. Royer, B. Conyers, E. I. Corwin, P. J. Eng, and H. M. Jaeger, *The role of interstitial gas in determining the impact response of granular beds*, Europhys. Lett. **93**, 28008 (2011).

[20] T. Homan, C. Gjaltema, and D. van der Meer, *Collapsing granular beds: The role of interstitial air*, chapter 3 of this thesis (2013).

[21] H. Darcy, *Les fontaines publiques de la ville de Dijon*, Victor Dalmont, Paris (1856).

[22] P. C. Carman, *Flow of gases through porous media*, Butterworths Scientific, London (1956).

[23] T. Homan, R. Mudde, D. Lohse, and D. van der Meer, *High-speed X-ray imaging of a ball impacting on loose sand*, chapter 2 of this thesis (2013).

[24] R. Bergmann, D. van der Meer, S. Gekle, A. van der Bos, and D. Lohse, *Controlled impact of a disk on a water surface: Cavity dynamics*, J. Fluid Mech. **633**, 381 (2009).

5

Long time-scale relaxations of the interstitial air in a granular bed *

A pressure difference over a porous medium relaxes exponentially according to Darcy's law. We calculate the permeability of a sand bed both from constant flow measurement and via the relaxation time. The sand bed is perturbed in three different ways and the long time-scale relaxation is compared. The details of this relaxation depend on the initial pressure profile. In this context, the three different perturbation methods vary in the degree of homogeneity: From a very homogeneous bed during the constant flow experiments, via a constant pressure profile in the shock experiments, to a very inhomogeneous pressure buildup during the granular impact.

5.1 Introduction

In 1856 the French hydraulic engineer Henry Darcy published his research on the flow through sand filters in *Les Fontaines Publiques de la Ville de Dijon* [1]. This work has been generalized into the famous *Darcy's law* which relates the flow through a porous medium with the pressure difference and the properties of

*To be submitted as: Tess Homan, Sylvain Joubaud, Detlef Lohse, and Devaraj van der Meer, "Long time-scale relaxations of the interstitial air in a granular bed".

the porous medium. Since the pores are very small the flow inside these pores is laminar and can be described by Poiseuille flow, but the path the fluid takes through the medium is very irregular which is where the porosity comes into play. A hundred years later Philip C. Carman published the relation between the permeability and the porosity of packed bed of granular particles, which led to the *Carman-Kozeny* relation [2].

Fluid flow through granular media is found extensively both in nature and industry. Where the aim of Darcy's research was to provide the inhabitants of Dijon with a dependable source of clean water by improving water filtration through vertical sand beds, filters are still of vital importance to our modern society. One example lies in the petrochemical industry where the multiphase flow and high demands on efficiency require a very detailed analysis of flows in pores all starting from Darcy's law. Darcy's law has been shown to accurately describe the global flow through a homogeneous porous medium under an applied pressure difference as long as the flow rate is low enough such that the flow in the pores stays laminar.

In this chapter we measure the pressure difference over a sand bed after it has been perturbed in three different ways. The initial pressure difference is set up by applying a constant air flow rate, tapping the container or by letting an object impact and penetrate the bed. All perturbation methods generate a pressure difference over the bed, but the homogeneity for each procedure varies, ranging from very homogeneous (constant flow method) to very localized (impact and cavity collapse). The pressure measurements are directly related to the airflow inside the sand bed and we will use Darcy's law to calculate the value for the permeability and compare the flows for the different initial pressure profiles. We find that the airflow in all three cases can be described by Darcy's law. The method of perturbation and the resulting initial pressure distribution is different which reflects in the long time-scale pressure relaxations.

5.2 Experimental setup

The three different methods of creating a pressure difference over the bed share the same basic setup (see figure 5.1). It consists of an airtight container with a cross-sectional area A of 14×14 cm^2, filled with very fine sand to a height H. A porous plate in the container allows us to blow air into the setup from below while keeping a horizontal support for the sand. By blowing air through the bed, the sand is decompactified, homogenized, and fluidized. The flow comes from the 4 bar dry air supply in the lab, controlled using a reduction valve. When the inflow of air is slowly turned off (the end of the fluidization process), the sand

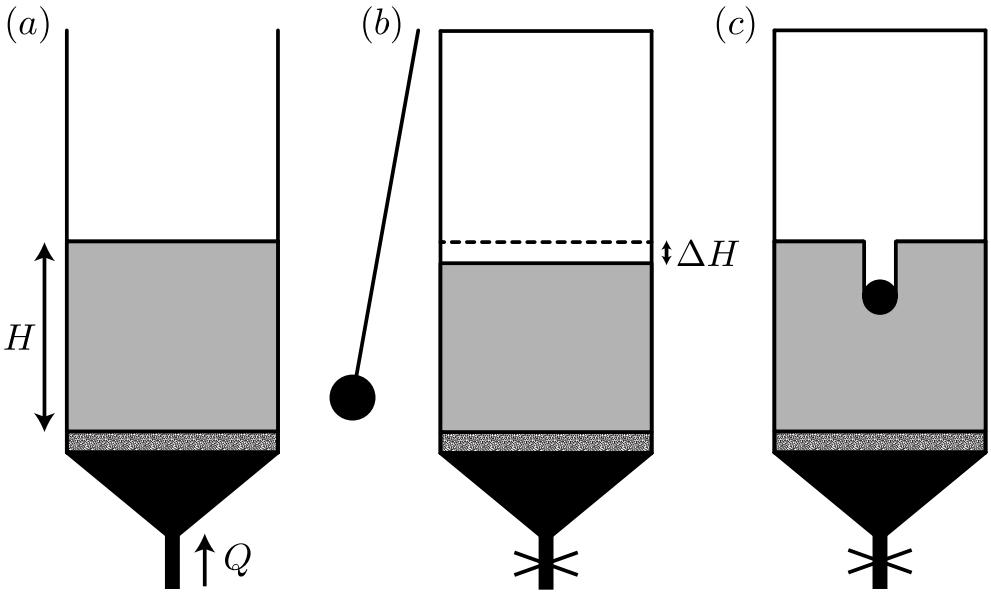

Figure 5.1: The setups used in the three different type of experiments. All three experiments are carried out in the same container (dimensions $14 \times 14 \times 100$ cm) with the same sand (sizes 20-60 μm). An initially loose sand bed (fill height $H = 40$ cm) is formed on top of a porous plate allowing for air to flow in and out of the sand both at the top and the bottom. (a) A constant air flow Q is blown into the container from below, increasing the pressure below the bed and initializing a pressure difference over the bed. The top is left open such that above the bed we have atmospheric pressure. (b) A metal ball attached to a pendulum impacts on the wall of the closed container. This shock will compactify the sand and therefore cause a higher pressure inside the bed and a reduced pressure above the sand. (c) After the impact of a ball on the sand surface the object will penetrate the sand. During this penetration air is being trapped inside the sand, increasing the pressure in the bed and lowering the pressure above the bed. The setup can be brought to low ambient pressures by slowly pumping out air from below and above the sand.

settles in a loosely packed state, with a volume fraction of around 40%. The sand is poly-disperse with sand grains ranging in size from 20-60 μm. The grains are not round, but have eccentricities between 0.2 and 0.6. The density of the sand grain material is 2.21 $\pm$ 0.04 g/cm^3 [3]. The pressure above and below the sand bed is measured using two WIKA TRONIC absolute pressure gauges. A McMILLAN mass flow meter (model 50D-7) measures the incoming flow at the bottom of the setup. The data from the pressure sensors and the flow sensor is collected simultaneously. The closed container can be vacuum pumped to perform experiments at low ambient pressures. Air is pumped out of the container at the same time from the top and the bottom. The outflow is slow (resulting in a rate of change of the pressure of 5 mbar/s) such that the loose packing of the bed is not disturbed.

5.3 Constant flow

The most straightforward method for determining the permeability κ of a porous bed uses a constant flow of air through the sand bed. When the flow through the sand and the pressure drop over the bed are measured, Darcy's law provides the permeability of the sand bed. Darcy's law describes the flow of a fluid through a porous medium [1]. It relates the flow Q, the viscosity of the fluid μ and the pressure drop ΔP over a certain distance L by:

$$Q = -\frac{\kappa A}{\mu}\frac{\Delta P}{L}. \tag{5.1}$$

At a small rate (Q=1500 mL/min) dry air is blown through the pre-fluidized sand bed from below, as shown in figure 5.1a. This flow rate is small enough to not disturb the sand packing and an equilibrium state with a constant flow through the bed and a constant pressure difference over the bed is reached. The actual flow rate and the pressure difference are measured for 10 minutes at a rate of 1000 Hz (600000 data points). From these measurements κ can be calculated using equation (5.1), and the results are plotted in figure 5.2. The combined permeability, of both the porous plate and the sand, is measured for varying bed heights, see the purple circles in figure 5.2. We observe that κ is constant for all heights, except for very small bed heights, where we probably did not fulfill the requirements of a completely stationary bed: If the grains are moving slightly this will compactify the bed and change the measured permeability.

The setup used in the experiments effectively consists of two porous media in series (see figure 5.1): A porous plate (with permeability κ_p and thickness H_p),

and the sand bed (with permeability κ_s and a height denoted by H_s). Darcy's law for these two porous media is given by:

$$Q = -\frac{\kappa_p A}{\mu}\frac{\Delta P_p}{H_p}, \text{ and} \tag{5.2}$$

$$Q = -\frac{\kappa_s A}{\mu}\frac{\Delta P_s}{H_s}. \tag{5.3}$$

Clearly, the flow rate must be constant through both materials, and the total pressure drop must be the sum of the drop over the plate and the drop over the sand bed,

$$\Delta P = \Delta P_p + \Delta P_s = -\frac{Q\mu H_p}{A\kappa_p} - \frac{Q\mu H_s}{A\kappa_s} = -\frac{Q\mu}{A}\left(\frac{H_p}{\kappa_p} + \frac{H_s}{\kappa_s}\right), \tag{5.4}$$

from which we obtain:

$$Q = -\frac{\Delta P A \kappa_p \kappa_s}{\mu\left(H_s\kappa_p + H_p\kappa_s\right)}. \tag{5.5}$$

The permeability of the sand κ_s is found by rewriting equation (5.5):

$$\kappa_s = -\frac{Q\mu H \kappa_p}{\Delta P A \kappa_p + Q\mu H_p}. \tag{5.6}$$

κ_p is measured in the same setup, but without a sand bed. The permeability of the plate is shown in figure 5.2 as the green stars. The value we found for κ_p is $(3\pm1)\cdot10^{-13}\text{m}^2$.

The permeability of the sand alone (κ_s) is plotted in black in figure 5.2. For a standard bed height of 40 cm, the difference between the combined permeability and the permeability of the sand alone is small ($\approx 10\%$), thus, the plate lowers the effective permeability, but this is within the experimental error.

5.4 Relaxation

The second method to determine the permeability makes use of the relaxation of a pressure difference over a porous bed. In order to obtain the permeability from the relaxation time we first need to know the relation between these two quantities, which we can obtain using Darcy's law and the ideal gas law.

When both sides of Darcy's law (equation (5.1)) are multiplied with the density of air ρ_0 at standard temperature and pressure, the mass flow rate through the porous medium is obtained:

$$\frac{dm}{dt} = \rho_0 Q = -\frac{\rho_0 \kappa A}{\mu L}\Delta P, \tag{5.7}$$

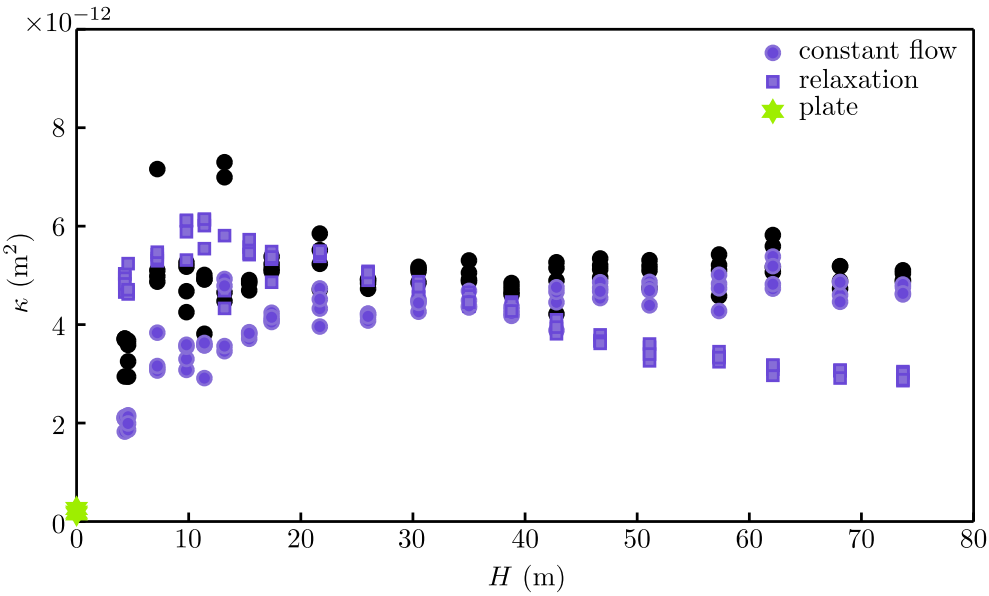

Figure 5.2: Permeability κ of the combination of bed and plate as a function of the bed height measured using two different methods: The constant flow method (circles) and the relaxation method (squares). The black circles give the permeability of the sand alone κ_s, *i.e.*, corrected for the presence of the plate. The green stars indicate the measurement of the permeability of the plate κ_P

or to write it in terms of pressure, $\rho_0 = P_0 M / RT_0$, where P_0 is the ambient pressure, M the molar mass of air, R the universal gas constant and T_0 the temperature:

$$\frac{dm}{dt} = -\frac{P_0 M \kappa A}{RT_0 \mu L} \Delta P. \tag{5.8}$$

By looking at a closed amount of air of volume V at pressure $P = P_0 + \Delta P$ (see figure 5.1a), dm/dt can be related to $\Delta P(t)$ using the ideal gas law:

$$PV = nRT_0, \tag{5.9}$$

where n is the number of moles gas, which is equal to $n = m/M$, with m the mass of air. Inserting these relations in equation (5.9) yields:

$$(P_0 + \Delta P)V = \frac{mRT_0}{M}. \tag{5.10}$$

Differentiating with respect to time gives:

$$\frac{dm}{dt} = \frac{VM}{RT_0} \frac{d\Delta P}{dt}. \tag{5.11}$$

Combining equation (5.11) and equation (5.8) results in the following differential equation:

$$\frac{d\Delta P}{dt} + \frac{P_0 \kappa A}{\mu LV} \Delta P = 0. \tag{5.12}$$

Solving this differential equation, we obtain an exponential equation for ΔP as a function of time :

$$\Delta P = \Delta P^* e^{-\frac{P_0 \kappa A}{\mu LV} t} = \Delta P^* e^{-\frac{t}{\tau}}, \tag{5.13}$$

with ΔP^* the initial pressure difference and τ the relaxation time given by:

$$\tau = \frac{\mu LV}{P_0 \kappa A}, \tag{5.14}$$

where the length-scale L can be identified with the bed height H.

From the above analysis we find that the pressure difference over the bed ΔP decreases exponentially with time. The relaxation time τ depends on the system parameters, the ambient pressure and the permeability. By measuring the relaxation of a pressure difference we therefore are able to calculate the permeability of the bed.

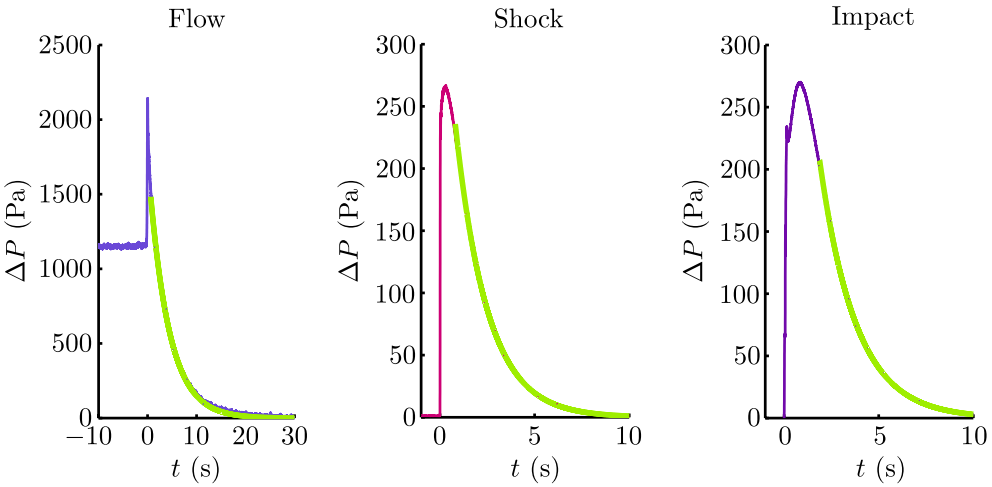

Figure 5.3: The signals for the three different relaxation experiments used to determine the permeability. (a) When, after the constant flow experiment, the inflow valve is closed, the buildup pressure difference decays in time until there is no pressure difference over the bed. An exponential fit is plotted in green. (b) The container wall is hit by an object. This shock collapses the bed and air is trapped inside the sand, while the pressure above the bed is decreased. The pressure difference over the sand bed relaxes exponentially with time. (c) If an object is released above the bed it will impact and penetrate the sand. During the penetration air is trapped inside the sand, increasing the pressure in and below the sand bed. The pressure above the bed decreases during the impact event, creating a pressure difference over the bed. Measuring this pressure difference as a function of time gives an exponential decay.

5.4.1 Flow

The first method to initiate a pressure difference over the bed starts from the equilibrium state described in the constant flow section. When the inflow of air is suddenly turned off, by manually closing the valve at the bottom of the container, the buildup pressure difference will decay in time. The pressure signal around this turn-off is visible in figure 5.3a. The peak is caused by the sudden closure of the inflow valve and for the long time-scale behavior we only look at that part of the signal where it is again below the initial constant value. When the pressure is plotted on a log-scale the result is a straight line, indicating exponential decay, as expected from equation (5.13). The relaxation time of the decay τ is found by fitting the signal and the fit is shown as a green line in figure 5.3a. Using the equation found above (5.14) for the relaxation time, we calculate the permeability of the sand bed from the relaxation experiments. The results from this analysis are shown in figure 5.2 (purple squares) as a function of the height of the sand bed. κ varies a bit with the bed height, but the main value is similar to the results from the constant flow experiment. It was not possible to determine the permeability of the plate using the same measurement technique. Here the pressure difference is so small that the part of the decay we are able to measure is too short to perform a good exponential fit.

5.4.2 Shock

In the second set of experiments the bed is perturbed by an object hitting the wall of the container, as described in chapter 3 of this thesis [4]. We again start with a very loose pre-fluidized bed, and the container is completely closed. At the moment of impact the bed collapses, which happens so fast that air has no time to move out of the bed. This air entrapment causes an initial pressure increase inside the bed. If the bed collapses homogeneously, this would also result in a homogenous pressure increase throughout the bed. At the same time, the volume above the bed is suddenly increased leading to a decrease in the local pressure. Due to the newly formed overpressure inside the bed air moves out of the sand into the upper and lower container. This continues until the pressure in the lower container is equal to that in the lower part of the sand bed and we are, again, left with a pressure difference over the sand bed. In time, all excess air will move to the upper container until the pressure in the entire container is back to the equilibrium state, just as before the shock. The pressure difference over the bed is plotted as a function of time in figure 5.3b. The long time-scale variation in the signal is an exponential decay, shown with the green fitted line.

Since the generated pressure differences in the experiment are much smaller than in the previous experiments, a different, more sensitive, pressure sensor is used (SENSIRION SPD600). Two pressure sensors measure the pressure above and below the bed with respect to an external reservoir, which initially is brought to the same ambient pressure as the container and then sealed off. To measure the pressure difference a small air flow goes through the sensor from the upper *c.q.* lower container to the reservoir. This flow is proportional to the measured pressure differences ΔP_1 and ΔP_2: $Q_{\text{leak}} = \sigma \Delta P_{1,2}$, where σ is the flow rate due to leakage $\sigma = 5.0 \cdot 10^{-9} \text{m}^3/\text{Pa·s}$. The total equation for the change in the pressure difference over the bed $\Delta P = \Delta P_2 - \Delta P_1$ then becomes:

$$\frac{d(\Delta P_2 - \Delta P_1)}{dt} = -\frac{P_0 \kappa A}{\mu H}\left(\frac{1}{V_1} + \frac{1}{V_2}\right)\Delta P - \frac{P_0 \sigma}{V_2}\Delta P_2 + \frac{P_0 \sigma}{V_1}\Delta P_1. \quad (5.15)$$

Since the total amount of air inside the container stays constant: $V_1 \Delta P_1 + V_2 \Delta P_2 = K$, with K very close to zero, we can rewrite equation (5.15) into

$$\frac{d(\Delta P)}{dt} = -\frac{P_0 \kappa A}{\mu H}\left(\frac{1}{V_1} + \frac{1}{V_2}\right)\Delta P - \frac{P_0 \sigma}{V_1 + V_2}\left(\frac{V_2}{V_1} + \frac{V_1}{V_2}\right)\Delta P + \frac{P_0 \sigma}{V_1 + V_2}\left(\frac{1}{V_1} - \frac{1}{V_2}\right)K. \quad (5.16)$$

This last term is independent of ΔP_1 and ΔP_2 as well as small, which means that it will show up as a deviation from the exponential decay at large times. The permeability is now given by

$$\kappa = \frac{\mu H}{A}\left(\frac{1}{P_0 \tau}\frac{V_1 V_2}{V_1 + V_2} - \sigma\right). \quad (5.17)$$

The relaxation time in the shock experiment is measured, and the permeability is calculated using (5.17). The shock experiments are performed for different impact strengths (denoted with the amount the bed has collapsed ΔH) and at various ambient pressures P_0. The permeabilities for all different experiments are calculated and plotted in figure 5.4a and b. The relaxation time in figure 5.4a (and therefore κ, see inset) is found to be almost independent of the shock strength which we will discuss in more detail later in this chapter. According to equation (5.17) the relaxation time depends on the ambient pressure, which is exactly what we see in figure 5.4b. τ is inversely proportional to the ambient pressure, but the permeability κ should be a constant, which is shown in the inset of the figure.

The permeabilities measured in the shock experiments are a bit lower than in the constant flow measurements. A lower κ indicates that it is more difficult for

air to flow through the bed. In the shock experiment the sand bed is compactified, in contrast to the constant flow measurements, leading to larger packing fraction ϕ and thus smaller pores for the air to move through, which results in a lower permeability.

Another possible difference between the two perturbation methods is the initial pressure profile in the bed. For the stable constant flow measurements we can safely assume that the pressure changes linearly from high pressure below the bed to low pressure above the bed. The relaxation analysis assumes that such a profile is also present in the shock measurements at the long time scale. Since we observe that the relaxation here is truly exponential a similar profile must have been created along the way. These two effects (the changing packing fractions and the influence of the initial pressure profiles) will be discussed in more detail in the next section.

5.4.3 Impact

When a ball impacts on compactified sand it might cause some sand to shoot away from the impact site, and the ball will come to a rest on top of the sand surface. However, a ball impacting on pre-fluidized sand will penetrate the bed and come to rest several ball diameters below the surface [5, 6]. During such an event a pressure difference over the bed is generated, which can be attributed to air being trapped inside the compactified sand in front of the ball and a more global bed collapse (resembling that of the shock experiments) this time caused by the violent collapse of the cavity that is created behind the ball. For more details see chapter 4 of this thesis [7]. This method of creating a pressure difference is the third and last setting in which we measure the permeability of the sand bed, and it is the least homogeneous: The first pressure increase in the bed is very local, in which air is compressed in front of the ball trapping air inside the sand, and the cavity collapse that causes the bed to compactify happens in the center of the container.

The pressure signal as a function of time in figure 5.3c shows a fast increase in the pressure difference followed by a much slower decrease. The absolute pressure difference depends on the impact speed of the ball (v), which is given by the Froude number:

$$\mathrm{Fr} \equiv \frac{2v^2}{gD} = \frac{4h}{D}, \tag{5.18}$$

where g is the acceleration due to gravity and D the ball diameter. The last step is valid if the air drag on the impacting object is neglected, such that the impact velocity can be calculated from the release height above the bed h, $v = \sqrt{2gh}$.

The time it takes for the pressure signal to become of the order of the noise depends on the initial pressure difference and the ambient pressure. If the pressure difference is higher, such as for stronger impacts (higher Froude number), the total measurable decay time is longer, but the relaxation time τ, calculated with equation (5.17), stays constant, which can be seen in figure 5.4c. Lower ambient pressures result in a much longer relaxation time, just as predicted by equation (5.17), and the measured values are shown in figure 5.4d. The calculated permeability of both the sand bed and the plate is independent of the Froude number and the ambient pressure.

5.5 Comparison

We have three different experiments in which the permeability is calculate using a relaxation analysis with different methods of creating the initial pressure difference. How do the measured permeabilities of these experiments compare to each other and the theoretical values? And what do the relaxation profiles tell us about the air inside the sand?

5.5.1 Carman-Kozeny

First, as mentioned in the introduction, Carman and Kozeny related the permeability of a porous bed with its porosity. Thus, if the properties of the sand grains and the sand bed are known we can calculate the theoretical value for the permeability:

$$\kappa = \frac{d^2(1-\phi)^3}{180\phi^2}. \tag{5.19}$$

The packing fraction ϕ, a measure for the porosity of a granular medium, is the fraction of the total volume that is occupied by the sand grains. This is measured by weighing the amount of sand m_{sand} that is put in the setup, and measuring the height of the sand bed after the fluidization process discussed previously. When the cross-sectional area of the sand bed and the density of the sand grains ρ_s are known, the packing fraction can be calculated using

$$\phi = \frac{m_{\text{sand}}}{\rho_s A H}. \tag{5.20}$$

The packing fraction of the pre-fluidized sand bed is found to be 0.40 $\pm$ 0.02, when the bed height is more than $\sqrt{A}$. This is similar to the values reported in [3]. Below $H = 14$ cm the packing fraction is higher. Because in this case the bed is

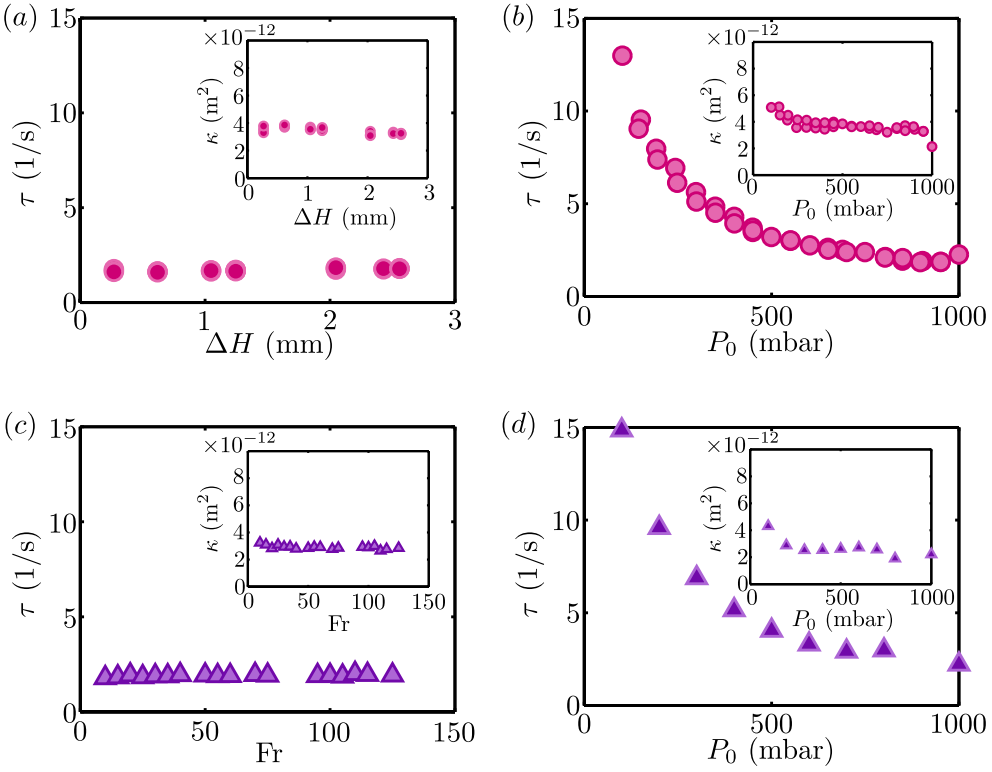

Figure 5.4: The measured relaxation times and permeabilities for the shock and impact experiments. (a) The relaxation time τ as a function of the bed height difference ΔH caused by a shock to the wall of the container of varying strength. The relaxation time time does not depend on this shock strength and (since all experiments were carried out at 1 bar) so does κ, as shown in the inset. (b) The relaxation time does depend on the ambient pressure at which the experiment is carried out. The lower the pressure the longer τ. The permeability is however constant for varying ambient pressures (inset). (c) For the impact experiments there is no dependence of the relaxation time and the permeability on the Froude number. (d) The relaxation time is inversely proportional to the ambient pressure at which an impact experiment is performed, but again with a constant permeability κ (inset).

lower than it is wide, a smaller fraction of the force chains end on the wall. This means a larger force down, resulting in a more compactified bed.

Based on the size distribution that is present in the sand, we can use equation (5.19) to obtain an apparent lower bound for the permeability: For the smallest size (d=20 μm) we calculate κ=3·10^{-12} m^2 and for the largest grain in the sample ($d = 60$ μm) we get $\kappa = 30 \cdot 10^{-12}$ m^2. Our measurements are much closer to the lower bound than the upper bound, indicating that either we have a majority of small particles in the mix, or that the size of the small particles is a key factor in permeability of the sample.

The packing fraction stays constant for the constant flow measurements, but in the shock and impact experiments it increases due to the collapse of the bed. The change in packing fraction $\Delta\phi$ is equal to

$$\Delta\phi = \frac{\phi_0 \Delta H}{H - \Delta H}, \tag{5.21}$$

Combining equation (5.19) and (5.21) and assuming ϕ_0 is close to $1/2$ gives

$$\kappa = \frac{d^2(1-(\phi_0+\Delta\phi))^2}{180(\phi_0+\Delta\phi)^2} \approx \kappa_0(1-8\Delta\phi). \tag{5.22}$$

The permeability shifts down and the total decrease depends on the bed height difference. This is indeed what we see in the insets of figure 5.4. The measured permeability for the shock and impact experiments is low compared to the constant flow measurements, whereas we start from the exact same configuration, namely a pre-fuidized bed with identical sand particles. The only difference in the granular state is that the bed is compactified in the shock and impact measurements, leading to this lower value for κ.

In the shock experiments, the packing fraction should also depend on the height change ΔH after the collapse of the bed. The values found in the experiments for different shock strengths, shown in figure 5.4a, should therefore depend on the bed height difference. A close up of the permeability data indeed shows that κ decreases for higher packing fractions. It is more difficult for air to flow through denser beds, resulting in lower permeabilities.

5.5.2 Initial pressure profile

For the shock and impact measurements we were able to measure the pressure difference below and above the bed with respect to an external reservoir and not only the total pressure difference over the bed. This allows for a more thorough

analysis of the pressure change in time and an example of both the shock and the impact data is shown in figure 5.6. In the shock experiments (pink line in figure 5.6) the pressure above the bed (lower curve) decreases immediately after perturbation. The sand bed collapses (in a typical time of 30 ms) and the volume above the bed increases, almost instantly lowering the pressure above the bed. The pressure below the bed (upper curve) begins at zero, and starts to increase at a slower pace. The pressure difference between the sand bed and the volume below the bed forces air to flow out of the sand into the lower container increasing the pressure. After a maximum is reached the excess air below the bed flows through the bed into the the upper container. The relaxation times above and below the bed do not have to be equal, but the τ of the total pressure difference over the bed only depends on the rate of compactification and the ambient pressure.

In chapter 3 [4] of this thesis we described a theoretical model for the pressure inside the bed as a function of time after an initial fast collapse of the bed [4]. It is based on a one-dimensional diffusion equation derived from Darcy's law and the ideal gas law:

$$\frac{\partial \Delta P}{\partial t} = \frac{\kappa P_0}{\mu(1-\phi_0)} \frac{\partial^2 \Delta P}{\partial z^2}. \tag{5.23}$$

The analysis provides a way to non-dimensionalize the data taken from experiments for different bed height changes and for different ambient pressures onto one master curve and the results are shown in figure 5.5. In this work we assume that the bed collapses homogeneously, and the pressure rises by the same amount in the entire bed. Here we repeat the same analysis using three different initial pressure profiles: A constant pressure rise (black solid line, as described in the chapter), a linear profile with more air near the top of the sand than near the bottom (black dashed line), and a profile in which all the air is concentrated in the top half of the bed (black dotted line). All three profiles are plotted on top of the non-dimensionalized experimental data.

It is clear from figure 5.5 that both non-uniform profiles, in comparison to the uniform one, lead to a lesser agreement with the data from the experiments. The pressure below the bed increases less for the two non-uniform pressure distributions. Since the initial model (solid black line) slightly over predicts the pressure, this could in principle improve matters, but not only the absolute value of the peak changes, it is also delayed in time and the relaxation time is increased even further. If more air is present closer to the top of the sand, either because of the linear profile (dashed black line), or because all the air is compressed in the upper half of the bed (dotted black line), the increase of the pressure above the bed will be faster than in the equally distributed air case (solid black line).

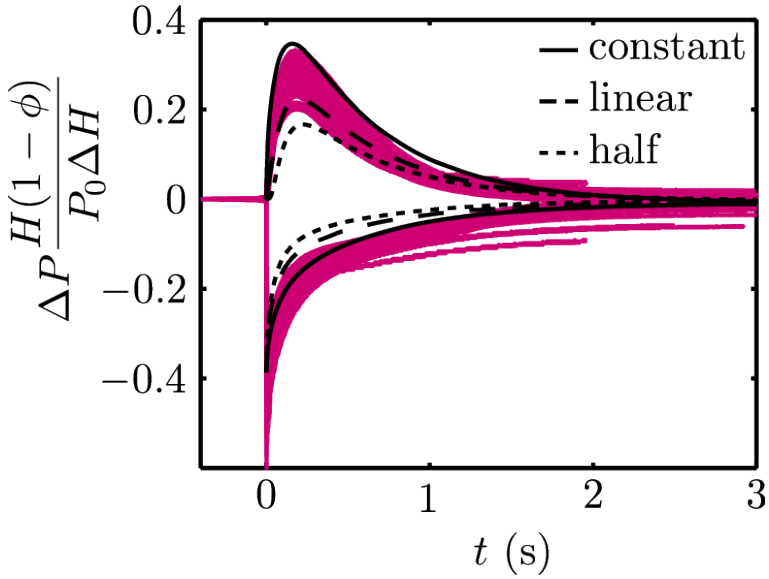

Figure 5.5: Non-dimensionalized, collapsed data for shock experiments with various shock strengths ΔH and at different ambient pressures P_0 (see main text in chapter 3 for details). The pressure above the bed drops instantly (lower curves) and then relaxes back to zero. The pressure below the bed (upper curves) first increases, reaches a maximum and also ends up at zero. The three black lines give the non-dimensionalized pressure signal calculated with the model from chapter 3, starting from three different initial conditions: A constant, uniform profile (solid black line), a linearly increasing profile (dashed black line) and a profile in which all the air is concentrated in the top half of the sand bed (dotted black line). The uniform profile result is identical to the one that was discussed in chapter 3 [4].

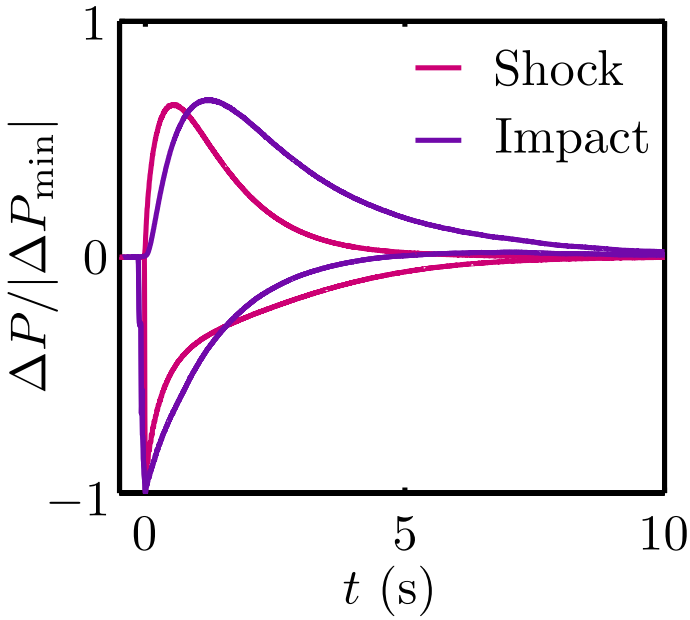

Figure 5.6: A direct comparison of a shock and an impact measurement at 1 bar. The shock (pink) caused a bed heigh difference of 1 mm, the impacting ball (purple) had a Froude number of 100. The upper curves show the change in pressure below the bed. The lower curves give the pressure in the upper container. The data is rescaled with the magnitude of the minimum pressure difference $|\Delta P_{\min}|$ above the bed. Also, $t = 0$ is defined as the time for which this minimum is reached.

From this we conclude that even though the total pressure increase below the bed is predicted more accurately by an initial pressure profile that is linear, the original description of the pressure inside the bed describes the complete signal to a greater extent.

5.5.3 Shock versus impact

In this section we investigate the difference between the pressure signals from the shock and the impact experiments. Two measurements at 1 bar are shown in figure 5.6, rescaled with the minimal pressure above the bed. The pressure decrease above the bed originates from a sudden increase in the volume when the bed collapses. We see that while the pressure is only rescaled with the values above the bed, the maximum pressure below the bed is also almost identical. Thus, proportional to the pressure difference above the bed, a similar amount of

air moves from the sand into the lower container in both experiments, but it takes more time to reach the maximum for the impact measurements, and therefore also the pressure release is slower. This indicates that the compressed air travels for a longer time before it reaches the bottom of the container. A second observation is that the pressure above the bed starts increasing slower in the impact experiments than in the shock experiments. This implies that the air is further away from the sand surface after an impact than after a shock, such that it takes longer for the air to escape.

It is clear that the distribution of the air in the shock experiments and the impact experiments is very different, which emphasizes the way in which this pressure difference is buildup. In the shock measurements a homogeneous bed collapse causes the pressure to rise evenly in the bed, whereas the events where air gets trapped in the impact experiments are very local and cause an inhomogeneous pressure distribution.

5.6 Conclusion

The permeability of a pre-fluidized sand bed is measured in various experiments. In the most direct experiment the bed is subjected to a constant flow rate, which is a method in which the bed remains very uniform and loose. The measurements are repeated for different bed heights and it is found that the permeability is independent of the bed height above a height of $\sqrt{A}$. This coincides with measurements of the packing fraction which show that below $H_s = 14$ cm the bed is more compact and has a lower permeability which makes it more difficult for air to flow through the bed.

Besides measuring the permeability from a constant flow experiment it can also be derived from the relaxation time of a buildup pressure. In this chapter three different methods of perturbing the sand and generating an initial pressure difference are discussed, derived from constant flow, shock, and impact experiments. Three methods of initializing this pressure difference all lead to the similar results. The amount of compaction, or the packing fraction after the bed collapse, is an important factor in understanding the measured values. The calculated κ is lower for the shock and impact measurements than for the constant flow experiments. The perturbation in the shock and impact experiments causes the bed to collapse, and it is more difficult for air to flow through a compactified bed, leading to a lower permeability. The permeability decreases with increasing bed height differences and thus increasing packing fraction.

For experiments at low ambient pressures we measure a longer relaxation time.

This is due to the fact that the relaxation time is inversely proportional to the ambient pressure and still results in a constant κ as a function of pressure.

We tested several initial pressure profiles in a model of the shock measurements and compared these to the experimental data. The pressure profile that best fitted the experiments is a uniform pressure increase throughout the bed. The pressure distribution in the interstitial air inside the sand is far less homogeneous for the impact experiments, here so many events happen locally and probably the air is trapped closer to the top of the sand.

The exact pressure profile in the impact experiments remains an open question and how does pressure difference originated from the events above and below the surface?

References

[1] H. Darcy, *Les Fontaines Publiques de la Ville de Dijon*, Victor Dalmont, Paris (1856).

[2] P. Carman, *Flow of gases through porous media*, Butterworths Scientific, London (1956).

[3] G. Caballero, R. Bergmann, D. van der Meer, A. Prosperetti, and D. Lohse, *Role of air in granular jet formation*, Phys. Rev. Lett. **99**, 018001 (2007).

[4] T. Homan, C. Gjaltema, and D. van der Meer, *Collapsing granular beds: The role of interstitial air*, chapter 3 of this thesis (2013).

[5] D. Lohse, R. Rauhe, R. Bergmann, and D. van der Meer, *Creating a dry variety of quicksand*, Nature **432**, 689 (2004).

[6] D. Lohse, R. Bergmann, R. Mikkelsen, C. Zeilstra, D. van der Meer, M. Versluis, K. van der Weele, M. van der Hoef, and H. Kuipers, *Impact on soft sand: Void collapse and jet formation*, Phys. Rev. Lett. **93**, 198003 (2004).

[7] T. Homan, S. Joubaud, D. Lohse, and D. van der Meer, *Air entrapment during the impact of a ball on sand*, chapter 4 of this thesis (2013).

6

Force measurements during impact with an instrumented particle *

After the impact of a solid sphere on soft and dry sand, it penetrates surprisingly deep into the bed. The collapsing walls of the cavity formed behind the sphere create two jets, one shooting upward and one downwards. In this work, we describe direct measurements of the acceleration of the impacting particle using an instrumented sphere from SmartINST*. The sphere acts as a non-invasive probe that measures and continuously transmits the acceleration as it penetrates the sand, using a radio signal. Directly measuring the acceleration of the sphere in time reveals the dynamical details that occur during the impact that can not be resolved from the position information alone. The sphere is accelerated when the jet forms and decelerated strongly just before it stops. The results are compared to the phenomenological model by Katsuragi* et al. *[1]. It is found to describe the sphere position perfectly but lacks the details in the more complex acceleration data.*

*To be submitted as: Sylvain Joubaud, Tess Homan, Yoann Gasteuil, Detlef Lohse, and Devaraj van der Meer, "Force measurements during impact with an instrumented particle".

6.1 Introduction

When an intruder is moving through a fluid it is difficult to measure the forces that act on it non-invasively, especially if the motion of the intruding object is not externally controlled. This is particularly true if the fluid is opaque and the object's trajectory cannot be followed by eye, such as in a granular medium. The drag forces exerted on an object moving in such a medium have been studied in different configurations [2]. A typical example is an object penetrating into a loosely packed sand bed. In such experiments, a granular jet can be observed [3, 4], the formation of which has been studied by looking inside the sand using X-ray radiographic measurements [5, 6]. In previous work the trajectory of the ball inside the sand has been studied using a thin thread with markers attached to the ball [7], however this method is not accurate enough to determine the acceleration of the ball, because the details of the acceleration data are smoothened out. Direct acceleration measurement of the sphere have been performed using an accelerometer [8], the signal of which was transmitted via a plug attached to the sphere, which is likely to have disturbed its motion after cavity closure. In this chapter, the idea is to send a sphere in an in-sand mission similar to an outer-space mission: In both cases measurements are done and transmitted through radio signals. In both cases new terrain is being explored and surprises are brought back from the mission.

6.2 Experimental setup

A container of a square cross section measuring 14×14 cm^2 and a height of 1.00 m is filled with sand (grain size $20 - 60$ μm) (figure 6.1a). The sand bed is then fluidized using pressurized dry air which is injected into the sand bed through a porous bottom plate. When turning off the air flow, the bed settles into a loose state with a packing fraction of approximately 0.41 and reaches a height of 41 cm [7]. A sphere of diameter $D = 2.5$ cm is then released using a pneumatic release mechanism and dropped into the sand bed. The sphere penetrates into the bed and stops at a finite depth. The initial drop height gives the impact speed velocity v_{impact} or the dimensionless Froude number $Fr = 2v_{\mathrm{impact}}^2/(gD)$. Using a vacuum pump, the (absolute) ambient air pressure, P_0, within the container and the sand bed may reach a value between 10 mbar and 1 bar without affecting the packing structure of the sand bed [7]. The effect of these two characteristic parameters, Fr and P_0, will be discussed in this chapter.

In this study, the objective is to directly measure the acceleration (and, con-

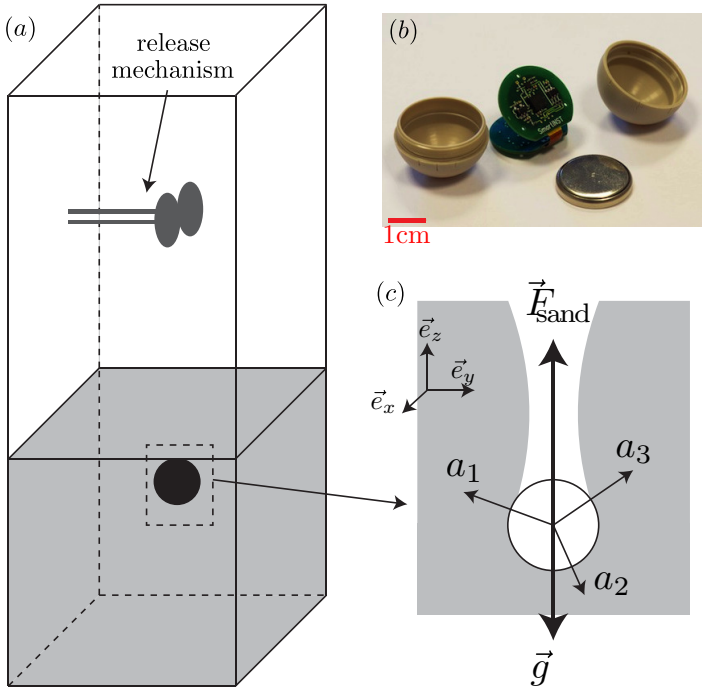

Figure 6.1: (a) Schematic of the experimental setup. Consisting of a container filled with loose sand and a pneumatic release mechanism to controllably drop the instrumented particle from various heights. (b) Picture of the instrumented sphere (taken from [9]) with a diameter of $D = 2.5$ cm. Inside the particle 3 accelerometers and the electronics to send the measurement signal are fitted. (c) The three components of the measured acceleration signal in the laboratory frame.

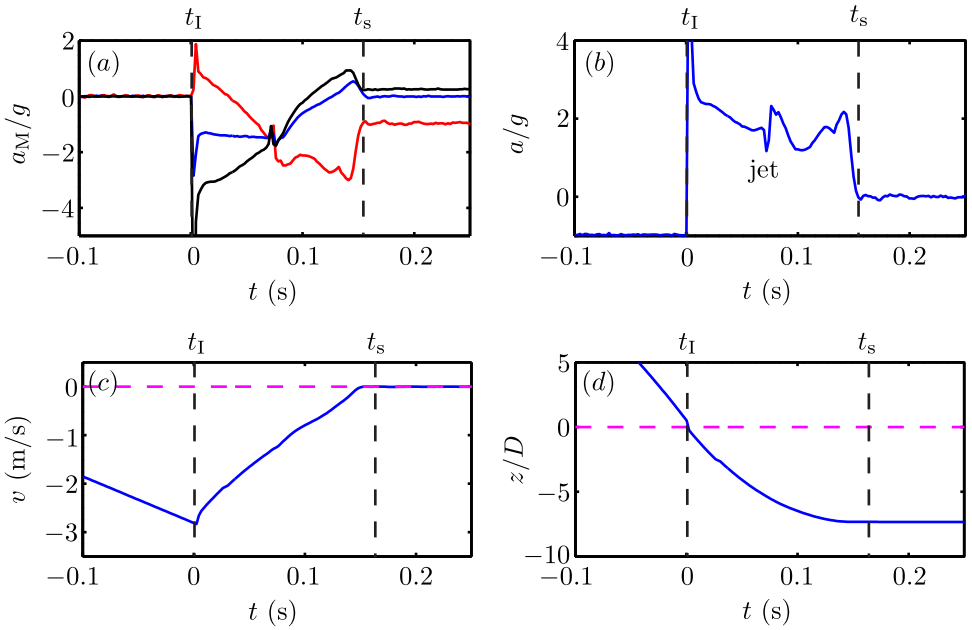

Figure 6.2: (a) Typical acceleration signal $a_{M,1}$, $a_{M,2}$, and $a_{M,3}$ of the three sensors for an impact with Froude number Fr=60 and $P_0 = 1$ bar. Accelerations are non-dimensionalized with g. (b) The dimensionless acceleration a/g, with $a \equiv ||\vec{a}_M|| - g$, as a function of time. (c) Particle velocity v as a function of time t. (d) Particle position z (non-dimensionalized with the particle diameter D) as a function of t. Note that the detailed information in $a(t)$ is smoothened out and thus lost in $z(t)$.

sequently, the force) acting on the sphere during its penetration into the sand without disturbing the features that characterize the impact experiment, namely the formation of the cavity, the granular jet and the pinched-off air bubble. The sphere consists of a device designed and built by smartINST®: The characteristics of it are described in detail in [9–11]. Let us present the basic properties of this system, depicted in figure 6.1b. A three-axis acceleration sensor, an electrical circuit, and a button cell battery are embedded into a spherical shell. The signal measured by the accelerometer is transmitted using radio waves to a data acquisition device located next to the experiment. The accelerometer measures the three components of the acceleration vector along the three perpendicular axes of the reference frame of the spherical particle. Each component ranges from $-16g$ to $+16g$ where g is the gravitational acceleration ($g = 9.8$ m/s^2). The resolution of acceleration is $0.01g$ and the acquisition frequency is 500 Hz (*i.e.*, a time resolution of 2 ms). The design of the accelerometer is such that the acceleration of the sphere at rest is equal to $-\vec{g}$ and during free fall to zero. A weight is added inside the particle to increase its density, creating an unbalance in the sphere. The weight of the particle obtained is of the order of 28 grams, which is similar to the weight of the steel ball used in the previous experiments [7, 12]. To minimize rotation, the particle is oriented such that the weight is positioned at the bottom of the particle.

6.3 Measurement signal

A typical acceleration signal measured by the three accelerometers is presented in figure 6.2a. A difficulty in the interpretation of the acceleration signal is that during the experiment the particle may rotate in the laboratory frame and therefore the orientation of the acceleration $\vec{a}$ we want to measure is not fixed in the particle reference frame. The relation between the measured acceleration $\vec{a}_M$ (*i.e.*, in the particle reference frame) and $\vec{a}$ is given by the equation

$$\vec{a}_M = \vec{a} - \vec{g} + \vec{a}_{\mathrm{rot}} + \vec{a}_{\mathrm{cor}} + \vec{a}_{\mathrm{noise}}\,. \tag{6.1}$$

The gravity term $-\vec{g}$ comes from the construction of the axis-acceleration sensors: In rest ($\vec{a} = 0$) we measure $\vec{a}_M = -\vec{g}$. Since the sensors are fixed in the particle reference frame, the Coriolis acceleration $\vec{a}_{\mathrm{cor}}$ is zero. The noise $\vec{a}_{\mathrm{noise}}$ can be seen in figure 6.2a. It is much smaller than the evolution of the acceleration signal during impact and will be neglected in the following. The magnitude of the rotational part of the acceleration $||\vec{a}_{\mathrm{rot}}||$ can be approximated by $\omega^2 r$, where ω is the angular velocity and r represents the distance of the acceleration sensor

to the center of the particle, which is of the order of 3 mm. To estimate the relevance of this term we turn to figure 6.2a: Without rotation the ratios a_i/a_j of any pair of measured acceleration components would be constant, since they would constitute the projection of $\vec{a}$ in a fixed reference frame. The time rate of change of these ratios can therefore be used to estimate the angular velocity ω, which is found to be smaller than 20 rad/s in all of our experiments. This leads to an acceleration $a_{\mathrm{rot}} \leq 0.1\ g$ which is negligible in comparison with the measured acceleration during the penetration of the sphere inside the sand. In conclusion, for the experiments discussed in this chapter equation (6.1) becomes in good approximation $\vec{a}_M = \vec{a} - \vec{g}$. Combining this expression with the equation of motion of the particle $m\vec{a} = m\vec{g} + \vec{F}_{\mathrm{sand}}$ leads to $\vec{a}_M = \vec{F}_{\mathrm{sand}}/m$, *i.e.*, the sensor measures the force $\vec{F}_{\mathrm{sand}}$ on the particle due to the sand directly (m is the particle mass). Here, it needs to be stressed that the orientation of the particle with respect to the lab frame of reference is still undetermined and (slowly) changing in time.

If we now assume that $\vec{F}_{\mathrm{sand}}$ is in the vertical direction in the lab frame of reference and use that it must always be pointing upwards since it is decelerating the particle, we can express the acceleration $\vec{a}$ of the particle in terms of the norm of the measured acceleration $||\vec{a}_M||$ as $\vec{a} = a\vec{e}_z = (||\vec{a}_M|| - g)\vec{e}_z$. The velocity of the particle can now be obtained by integration of a using the fact that the velocity needs to be zero when the particle has stopped (*i.e.*, $t > t_{\mathrm{stop}}$): $v(t) = \int_t^{t_{\mathrm{stop}}} a(t')\mathrm{d}t'$. And finally, the integration of the velocity signal gives the position z of the particle as a function of time $z(t) = \int_0^t v(t')\mathrm{d}t'$. Here, $t = 0$ is defined at the time of impact which corresponds to $z = 0$.

This procedure has been followed with the data of figure 6.2a for Fr$= 60$ and $P_0 = 1$ bar, with the norm of the acceleration signal minus gravity $a = ||\vec{a}_M|| - g$ plotted in figure 6.2b, the velocity v in figure 6.2c and the position z in figure 6.2d. We now discuss different parts of the acceleration signal. Shortly after the sphere is released the non-dimensionalized acceleration signal a/g goes to -1 indicating free fall behavior. This behavior is also observed in the velocity signal: Before the impact, the velocity decreases linearly with time with a slope equal to $-g$. The acceleration signal changes suddenly, immediately after the sphere hits the sand (defined at $t = t_I = 0$). Subsequently, the acceleration evolves during the motion of the sphere inside the sand until a/g suddenly drops to 0, indicating that the sphere has come to a stop and is experiencing a static friction force that is equal in magnitude but opposite to gravity. The time at which this happens corresponds to the stopping time of the sphere inside the sand t_{s}. Now, the sphere has reached its final depth and its velocity vanishes. The shape of the

position signal (figure 6.2d) corresponds well to that obtained directly by imaging a marker on a rod attached to the sphere [7]. Note that the position signal bears no sign of the short time irregularities visible in the acceleration signal. This is due to the double integration. In general, features that may appear significant in the acceleration signal may be hard to discern (if at all) in the time evolution of velocity and position. We want to point out the presence of a characteristic peak in the acceleration 80 ms after impact (figure 6.2b). This time coincides well with the collapse of the cavity and the formation of the granular jet. This valley followed by a peak could be interpreted as a signature of a granular jet that is directed downwards and pushes the sphere towards the bottom of the sand bed. This is the first time that the jet formation event has ever been directly resolved while measuring the trajectory of an impacting object, confirming the usefulness of the smart particle device[†].

First, the reproducibility of the experimental setup is tested and presented in figure 6.3a for four experiments done at the same conditions (Fr$= 83$ and $P_0 = 1$ bar). The signal can be devided into two parts separated by the peak around 80 ms, which is the signature of the granular jet formation. In the first part the behavior is clearly reproducible, where the smallness of the deviations between repeated experiments show that the prepared granular sand bed behaves in a defined way, as would be the case for a fluid. The cavity collapse and the granular jet formation are also well defined and reproducible since in all four cases they happened at the very same time. As the duration of the jet formation is expected to be very short (shorter than the resolution time of 2 ms), it is averaged over the resolution time of the experimental system and it is not possible to fully capture it. After the jet formation the behavior is slightly different for each experiment: There is some variation in both the deceleration magnitude and the stopping position. This discrepancy may well be due to the formation and the dragging-along of the pinched-off air bubble which is clearly a non-reproducible phenomenon, as seen in chapter 2 [6].

To investigate how the signal changes as a function of the two characteristic parameters of the experimental setup, we compare the acceleration for various Froude numbers (in figure 6.3b) and ambient pressures (in figure 6.3c). The first feature that catches the eye is the sudden deceleration of the sphere at impact ($t = 0$). The magnitude of this peak depends strongly on the Froude number:

[†]The effect of the granular jet could not be seen in previous experiments by measuring the position or by using the device of [8] in which the accelerometer was mounted on an aluminum plug. Such a device would be of no use in our experiment because the jet appears before the stopping time and would be destroyed by the presence of plug. Incidentally, this may also have been a problem in the setup of [8].

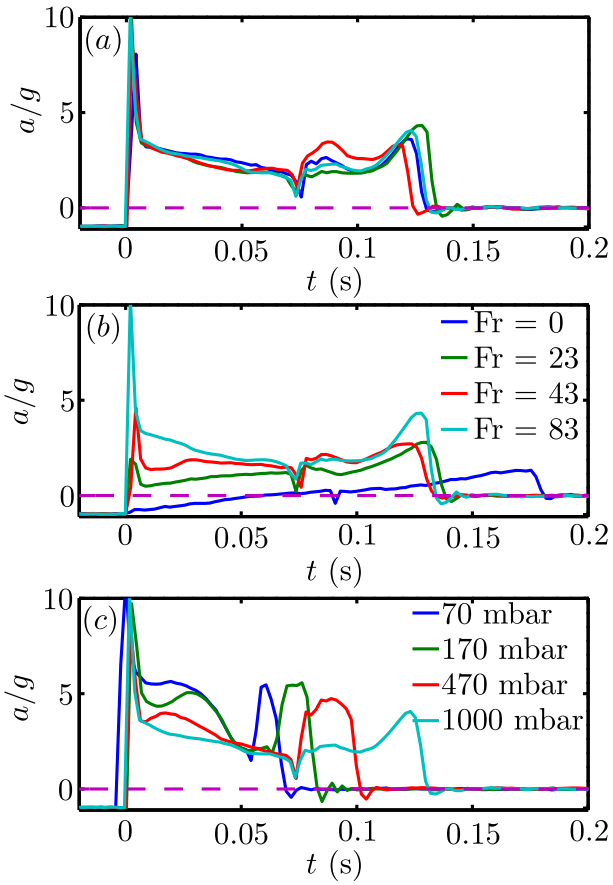

Figure 6.3: (a) Particle acceleration $a \equiv ||\vec{a}_M|| - g$ (non-dimensionalized with g) as a function of time t for four experiments done at the same experimental conditions, Fr$= 83$ and $P_0 = 1$ bar, showing the reproducibility of the experiment. (b) Acceleration as a function of time for experiments done at $P_0 = 1$ bar varying the Froude Number. (c) Acceleration as a function of time for experiments done at Fr$= 83$ varying the absolute ambient air pressure.

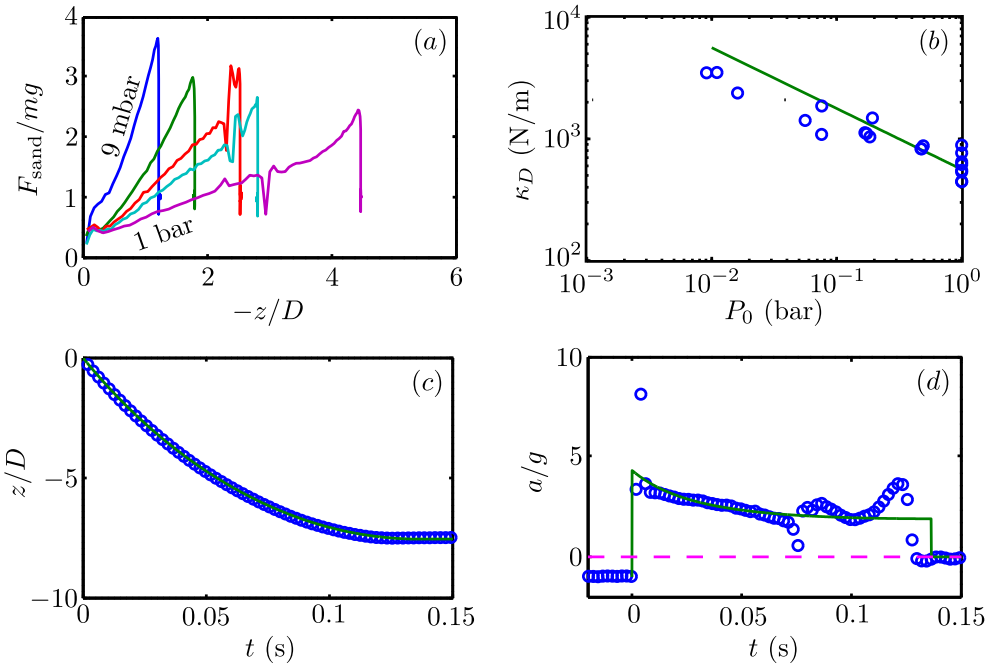

Figure 6.4: (a) Force $F_{\rm sand}$ (non-dimensionalized with mg) exerted by the sand bed on the particle as a function of the (dimensionless) position $-z/D$ within the sand bed for different ambient pressures $P_0 = 9,\ 75,\ 173,\ 472$ and 1000 mbar, for Fr$= 2$. For each pressure value, a linear fit provides the value of κ_D. (b) κ_D plotted as a function of the ambient air pressure P_0. The straight line is a power law with exponent $-1/2$. (c) The symbols $(\circ)$ represent the dimensionless experimental position z/D of the particle inside the sand bed for Fr$= 82$ and $P_0 = 1$ bar. The solid, green curve is the fit obtained using the model of Katsuragi [1] (d) Dimensionless acceleration a/g of the particle as a function of time $(\circ)$. The solid curve is the same fit to the model as in figure (c).

The higher Fr, the stronger the peak and it disappears when the impact velocity is close to zero. The strength of the peak however hardly depends on the ambient pressure, as expected since it is connected to the creation of a splash. A second feature is that the sphere stops earlier in time for smaller ambient air pressure. This is consistent with earlier experiments [12]. Thirdly one observes that for small Froude number the acceleration increases with time, whereas for large Fr it decreases with t. This is a characteristic of the drag law on which we will comment in the last part of this chapter. A final point is the strong deceleration that is visible just before the stopping time. It is more pronounced for large Froude number and for smaller ambient pressure. An interpretation of this phenomenon is the compaction of the sand in front of the sphere, which is expected to be more pronounced at high Fr and low P_0. This added mass effect is speculated to be prevented by an increase of the interstitial air pressure [13, 14] and a fluidization due to an air flow around the sphere [7].

6.4 Model

Finally, we want to compare these experimental results with various models that have been proposed to describe the evolution of the force during the evolution of the sphere inside the sand [1, 2, 4, 15–19]. More specifically, in the context of the experimental setup, the phenomenological drag law introduced by Katsuragi [1, 19] has been used to fit the evolution of the position of the sphere inside the sand bed as a function of time. This law consists of a hydrostatic term that linearly depends on the depth inside the bed, $F_{\text{hydrostatic}} = -\kappa_D z$ where κ_D is a constant dependent on the ambient air pressure [7]. The second term is a quadratic velocity-dependent drag that is independent of the depth, $F_{\text{dynamic}} = -\alpha v^2$ and becomes important for higher impact velocities[‡].

To compare the existing models to the experimental results, we first investigate the regime of low impact velocities where the drag is dominated by the hydrostatic term, *i.e.*, $F_{\text{sand}} \approx -\kappa_D z$. To verify this approximation, the force acting by the sand F_{sand} is plotted for different ambient pressures as a function of the depth z when the sphere is released as close as possible to the sand bed, which correspond to a Froude number of Fr≈ 2 (see figure 6.4a). After some initial deviations connected to the entry of the sphere into the sand bed, the measured acceleration shows a clear linear regime up to the granular jet formation (the peak in the

[‡]Using direct acceleration measurement, Goldman and Umbanhowar [8, 20] developed a drag force using a term linear with velocity as an alternative to the second term in the Katsuragi law. Such a linear term had also been proposed earlier by [17].

acceleration signal that is visible for higher pressures). Consequently, in this regime we can measure κ_D using a linear fit and plot the result as a function of P_0 (figure 6.4b). Although there is quite some scatter, the data is not inconsistent with the scaling law $\kappa_D \sim p^{-1/2}$ that was previously measured by Caballero *et al.* [7]. Beyond the point at which the granular jet is formed some deviations appear, most notably for $P_0 = 200$ and 500 mbar. These cannot be due to the $-\alpha v^2$ term since the velocity of the sphere is almost zero and it is therefore plausible that the deviations are connected to the formation of a pinched air bubble, that is dragged along with the particle.

Turning to the high Froude number regime, we find (as in [12]) that the particle position data is well fitted by the full Katsuragi force law $F_{\text{sand}} = -\kappa_D z - \alpha v^2$. As an example, in figure 6.4c we plot a typical trajectory (Fr$= 82$ and $P_0 = 1$ bar). We see that with $\kappa_D = 4.3$ N/m and $\alpha = 0.14$ kg/m the fit (solid curve) is excellent. When we turn to the acceleration however (figure 6.4d), we see that the fit is poorer than might have been expected based on the position data. Before the cavity collapse and jet formation (the dip in the signal) the agreement is reasonable, but after that there are large discrepancies. This is consistent with the accelerometer measurements of [8] where it was also concluded that the Katsuragi model was inaccurate for large depths. We now tentatively attribute these discrepancies to the pinch-off and subsequent dynamics of the air bubble that is observed to be attached to the particle. And, of course, even if the acceleration data is poorly fitted by the model after jet formation, the effect of this on the trajectory of the particle is hardly noticeable.

6.5 Conclusion

In this chapter, we provide a direct measurement of the acceleration of a sphere impacting on a granular bed, for the first time using a non-invasive technique. The signal reveals very complex dynamics including a signature of the jet formation which had not been observed previously. The model of Katsuragi [1] predicts the measured acceleration well up to the formation of the jet. Beyond this point the acceleration data deviates considerably, although the effects of this on the trajectory of the sphere are hardly discernible. The smart particle device used in these measurements proved to be an invaluable tool and could be employed for acceleration measurement in many other applications where this type of Lagrangian measurements are otherwise hardly feasible. It is especially useful in applications where the particle is not visible and can not be traced from the outside, such

as avalanches, and there where acceleration (and indirect force) measurements provide much more detailed and small time scale information than position data alone, such as in turbulent flows in liquids.

References

[1] H. Katsuragi and D. J. Durian, *Unified force law for granular impact cratering*, Nat. Phys. **3**, 420 (2007).

[2] F. Guillard, Y. Forterre, and O. Pouliquen, *Depth-independent drag force induced by stirring in granular media*, Phys. Rev. Lett. **110**, 138303 (2013).

[3] S. Thoroddsen and A. Shen, *Granular jets*, Phys. Fluids **13**, 4 (2001).

[4] D. Lohse, R. Rauhe, R. Bergmann, and D. van der Meer, *Creating a dry variety of quicksand*, Nature **432**, 689 (2004).

[5] J. R. Royer, E. I. Corwin, A. Flior, M.-L. Cordero, M. L. Rivers, P. J. Eng, and H. M. Jaeger, *Formation of granular jets observed by high-speed X-ray radiography*, Nat. Phys. **1**, 164 (2005).

[6] T. Homan, R. Mudde, D. Lohse, and D. van der Meer, *High-speed X-ray imaging of a ball impacting on loose sand*, chapter 2 of this thesis (2013).

[7] G. Caballero, R. Bergmann, D. van der Meer, A. Prosperetti, and D. Lohse, *Role of air in granular jet formation*, Phys. Rev. Lett. **99**, 018001 (2007).

[8] P. Umbanhowar and D. I. Goldman, *Granular impact and the critical packing state*, Phys. Rev. E **82**, 010301 (2010).

[9] R. Zimmermann, L. Fiabane, Y. Gasteuil, R. Volk, and J.-F. Pinton, *Characterizing flows with an instrumented particle measuring Lagrangian accelerations*, New J. Phys. **15**, 015018 (2013).

[10] R. Zimmermann, L. Fiabane, Y. Gasteuil, R. Volk, and J.-F. Pinton, *Measuring Lagrangian accelerations using an instrumented particle*, Phys. Scr. **T155**, 014063 (2013).

[11] R. Ni, S.-D. Huang, and K.-Q. Xia, *Lagrangian acceleration measurements in convective thermal turbulence*, J. Fluid Mech. **692**, 395 (2012).

[12] S. von Kann, S. Joubaud, G. A. Caballero-Robledo, D. Lohse, and D. van der Meer, *Effect of finite container size on granular jet formation*, Phys. Rev. E **81**, 041306 (2010).

[13] J. R. Royer, E. I. Corwin, B. Conyers, A. Flior, M. L. Rivers, P. J. Eng, and H. M. Jaeger, *Birth and growth of a granular jet*, Phys. Rev. E **78**, 011305 (2008).

[14] J. R. Royer, B. Conyers, E. I. Corwin, P. J. Eng, and H. M. Jaeger, *The role of interstitial gas in determining the impact response of granular beds*, Eur. Phys. Lett. **93**, 28008 (2011).

[15] J. Uehara, M. Ambroso, R. Ojha, and D. Durian, *Low-speed impact craters in loose granular media*, Phys. Rev. Lett. **90**, 194301 (2003).

[16] M. Ciamarra, A. Lara, A. Lee, D. Goldman, I. Vishik, and H. Swinney, *Dynamics of drag and force distributions for projectile impact in a granular medium*, Phys. Rev. Lett. **92**, 194301 (2004).

[17] J. de Bruyn and A. Walsh, *Penetration of spheres into loose granular media*, Can. J. Phys. **82**, 439 (2004).

[18] M. Hou, Z. Peng, R. Liu, K. Lu, and C. Chan, *Dynamics of a projectile penetrating in granular systems*, Phys. Rev. E **72**, 062301 (2005).

[19] L. Tsimring and D. Volfson, *Modeling of impact cratering in granular media*, Powders and Grains 1215 (2005).

[20] D. I. Goldman and P. Umbanhowar, *Scaling and dynamics of sphere and disk impact into granular media*, Phys. Rev. E **77**, 021308 (2008).

7

Drag reduction due to interstitial air in a granular bed *

An intruder is controlled by a linear motor and is connected to a load cell to measure the drag it experiences while moving through a very loose sand bed. By varying the intruder velocity and the pressure of the interstitial air we investigate the role of air inside the bed. We find that for velocities of the order of 100 mm/s and larger the presence of air reduces the drag experienced by the ball. At very low penetration velocities we observe no dependence of the measured force on the ambient pressure, here air has enough time to move away from the ball and does not affect the drag, similar to when no air is present in the setup.

7.1 Introduction

It is well known that the interstitial air may crucially affect the dynamics in a granular material. A striking example comes from the countertop experiment where an upside down container is pushed into a granular bed [1]. Counterintuitively, this is considerably easier than pushing down a container with an open top (*i.e.*, a cylinder). The pressure buildup inside the container wants to escape and in doing

*To be submitted as: Tess Homan and Devaraj van der Meer, "Drag reduction due to interstitial air in a granular bed".

so it locally fluidizes the sand just below the edges of the container, the *blown air effect*. This decreases the compaction, easing the downward motion of the container.

A possibly similar effect is found in a pre-fluidized granular bed, where the drag on an impacting object is observed to crucially depend on the ambient pressure [2, 3]. Surprisingly, these experiments reveal that the drag on the ball reduces when the air pressure is higher resulting in a deeper penetration for high ambient pressure than for low ambient pressure. Caballero *et al.* [2] propose a mechanism where compressed air in front of the ball locally fluidizes the sand effectively lowering the drag from the sand on the ball. Royer *et al.* [3] measured an area of compacted sand in front of the ball, and describe a layer of compressed air cushioning the ball to account for the shallow penetration when less air is present.

The drag force can be determined from measurements of the acceleration on an impacting intruder [4, 5]. This work reveals the rich behavior of the dynamics including the initial impact and the force caused by the cavity collapse, and compare the response with phenomenological models, that have been proposed in literature [6–11]. In this work the trajectory of the impactor itself is a function of the drag force it aims to measure.

To directly and accurately measure the influence of air on the drag force we therefore perform measurements where a ball is pushed into a sand bed by a linear motor. This way the trajectory of the ball is completely controllable and a load cell can be mounted into the setup to measure the applied force on the ball simultaneously. A similar setup has been used to measure the drag on an object in a medium consisting of larger grains, where the effects of air may be assumed to be negligible. There the focus lies on the effects of the nearby bottom [12, 13], and the influence of the packing fraction [14].

In this chapter we focus on the influence of the interstitial air. To do so we will measure the drag force as a function of the (controlled) velocity of the intruder. For extremely low velocities we expect that we retrieve the quasi-static limit [15, 16]: In this regime the motion of the object is so slow that the air can flow freely on the time scale of the penetration and consequently has no influence on the drag force. When this velocity is increased the influence of the air pressure will become measurable. To affect the importance of the interstitial air we in addition change the pressure, where we expect that at reduced ambient pressures due to the lower air density the ability of the air to influence the dynamics is diminished.

7.2 Experimental setup

The two main parts of the setup are a linear motor and a rectangular container ($14 \times 14 \times 100$ cm^3), see figure 7.1. The container is partially filled with sand (bed height H=30 cm) and the bottom of the container is made of a porous material. A metal chamber connected to the bottom closes off the container except for an air inlet. A flow controller regulates the airflow through the sand: First the sand is completely fluidized and then the airflow is slowly turned off to allow the sand to settle in a very loose packing ($\phi \approx 0.41$). The flow controller ensures the bed is prepared in a very reproducible way, such that the sand bed height variation between experiments is less than 1 mm, which corresponds to 0.3% of the bed height and is therefore neglected. The top of the container is closed as well, and both the bottom and the top lids of the container are connected via a second flow controller, which regulates the removal of air from the container for low ambient pressure measurements, to a vacuum pump. The air is pumped out of the container at a constant low mass flow rate of 6.3 l/min at P_0=1 bar, for which has been verified that the settled bed is not affected during the vacuum pumping process. In order to precisely control the impact conditions, a PVC ball with diameter $D = 3.17$ cm is connected to a rod which in turn is attached to a linear motor (COPLEY CONTROLS ServoTube 2506 Module). With the linear motor the ball can be positioned very precisely (with an accuracy of 1 μm). The ball is located inside the container and the rod moves through a vacuum seal in the top. A load cell (HONEYWELL model 31) is attached to the rod and is also located within the container, such that the friction generated in the seal does not contribute to the force measured by the load cell. During an experiment the ball is prescribed to penetrate the sand surface and move down to a certain predefined depth with a constant velocity. While the ball moves down, the forces exerted on the ball are measured simultaneously with the position of the ball. In this chapter we describe experiments done for various penetration velocities $\dot{z}$ and at different ambient pressures P_0.

7.3 Measurement signal

The magnitude of the drag force F_D on an object penetrating into a granular medium is known to be quite accurately described by the phenomenological drag law [4, 6–12]

$$F_D = \kappa_D z + \alpha \dot{z}^2. \tag{7.1}$$

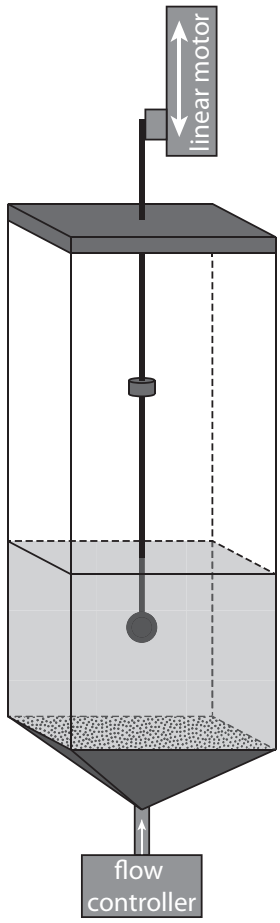

Figure 7.1: The setup consist of a container partly filled with fine sand (grain size ranges from 20-60 μm). A linear motor controls a rod to which a ball with diameter $D = 3.17$ cm is attached. A controlled air flow from the bottom first fluidizes the sand and subsequently lets it settle in a very loose packing while the airflow is slowly turned off. The ball starts above the bed and is accelerated downwards to its final velocity. It enters the bed with a constant velocity, penetrates to a certain predefined distance and then stops. During this movement the force exerted on the ball by the linear motor is measured using a load cell which is attached to the rod. With a vacuum pump the whole setup can be brought to a low ambient pressure, and a seal in the top lid ensures that the rod is able to move up and down without losing the reduced pressure state.

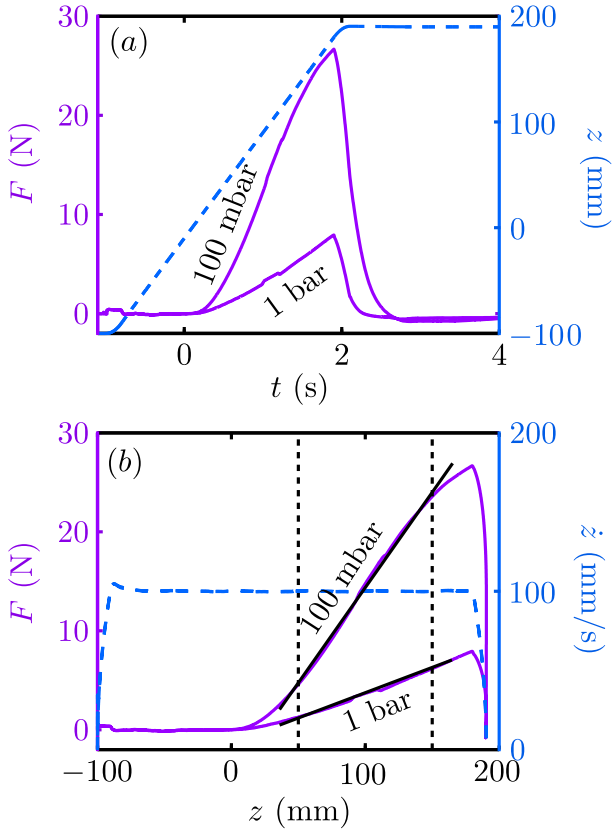

Figure 7.2: (a) The blue dashed line (right axis) gives the measured position of the ball as a function of time. Starting above the bed it is accelerated and enters the bed with a constant velocity $\dot{z} = -100$ mm/s. It then slows down and stops at a predetermined depth $z_{\text{final}} = 190$ mm below the surface. The purple plot (left axis) shows the measured force while the ball moves down at two different ambient pressures: 1 bar and 100 mbar. It starts at a constant value and increases as soon as the ball enters the bed. After the ball has stopped the force decays towards a constant. (b) Here the blue dashed line (right axis) shows the velocity as a function of the depth. The velocity is constant when the ball moves into the sand, and stays constant until it decelerates to stop. The purple lines (left axis) represent the same force data as in (a), but now as a function of depth, both for 1 bar and 100 mbar. Here we see a linear region that is consistent with a Coulomb drag after which the force starts changing due to the deceleration. The black line is a linear fit through the data in the measurement range (pointed out by the vertical dashed lines) from which we find the drag force constant κ_D.

The first term is a Coulomb drag where the upward force linearly increases with the depth z below the surface, with proportionality constant κ_D, indicating that work is being done against the hydrostatic (or lithostatic) pressure inside the sand. The second term is a drag force that scales quadratic with the velocity. For the low impact velocities ($\dot{z}$ =1-200 mm/s) used in this chapter the last term is much smaller than the Coulomb drag such that the total drag on the object should be linear with depth [17].

In figure 7.2a the signal of a single experiment is shown. The blue line gives the position of the ball as a function of time. The ball starts 10 cm above the surface of the bed and rapidly accelerates to its final target velocity. The force acting on the load cell before the experiment is equal to the mass of the rod plus the ball times the acceleration due to gravity and has been subtracted from the signal to get the drag force in figure 7.2a. Before the object hits the sand bed the airdrag is negligible compared to the forces measured in the sand which is why the measured force stays constant until the ball reaches the sand surface, apart from the small increase in measured force during the acceleration of the ball. As soon as the ball enters the bed the measured force increases. Two experimental curves are shown for the same impact velocity, $\dot{z} = 100$ mm/s, but for different ambient pressures of 1 bar and 100 mbar. In both experiments the force increases with time, but that measured for the low ambient pressure experiment is much larger. Close to the final depth the ball starts to decelerates and comes to a stop, the force decreases towards a constant.

In the second plot (figure 7.2b) the force is plotted as a function of depth. According to (7.1) the increase should be linear with depth if we do not accelerate or decelerate the ball. The blue line gives the velocity of the ball as a function of the depth. First the ball accelerates and it reaches a constant velocity before it enters the bed (at $z = 0$). The velocity changes when the ball is decelerated to stop at the desired final depth. Clearly the force is not linear for the entire trajectory inside the bed: Initially there is an entry effect where the object is not completely in contact with the bed. And towards the end of the trajectory, the object starts to decelerate which significantly alters the force measured by the load cell. To be in the constant velocity regime for all measured velocities (1-200 mm/s) only the data between the vertical black dashed lines is fitted to a straight line to find the slope and thus the drag force constant, κ_D.

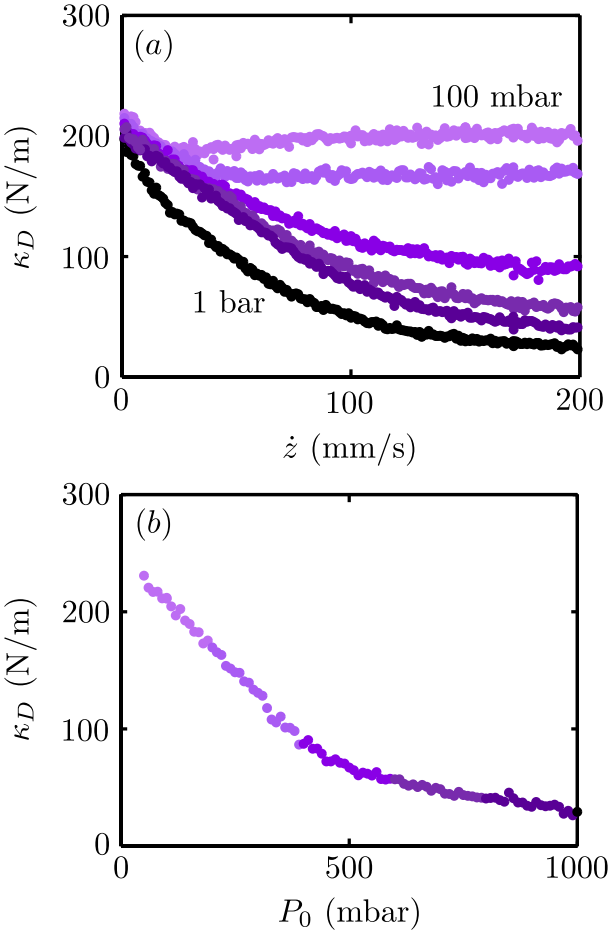

Figure 7.3: (a) *bottom (black) curve*: The drag force constant κ_D measured for experiments where the ball moves to a fixed final depth ($z_{\text{final}} = 210$ mm) at varying (constant) velocities (1-200 mm/s), at 1 bar. The measured drag is the highest for very low velocities where air has enough time to flow out of the sand. At higher velocities air is trapped in front of the ball, surprisingly lowering the measured drag. *other curves*: The drag force constant κ_D as a function of the intruder velocity for experiments at different ambient pressures $P_0 =$ 800, 600, 400, 200 and 100 mbar. The amount with which the drag force constant is lowered is reduced when less and less air is left in the container, and eventually, for the upper curve at $P_0 = 100$ mbar, there is hardly any dependence on the velocity. (b) The measured drag constant κ_D as a function of the ambient pressure P_0 for experiments performed at a penetration velocity $\dot{z}$ of 200 mm/s.

7.4 Impact velocity

In the first set of experiments the velocity with which the ball moves through the bed is varied. Here we confine ourselves to the regime where the contribution of the second term in equation (7.1), which is proportional to the velocity squared, is negligible, namely $\dot{z} < 200$ mm/s. To be able to compare experiments at different intruder speeds we determine κ_D as described above.

The result of these experiments are plotted in the lowest (black) curve of figure 7.3. Surprisingly we see a drag reduction for increasing intruder velocity. At very low velocities the drag force constant is high and it decreases with increasing intruder velocity. Above $\dot{z} = 150$ mm/s κ_D no longer decreases and becomes constant. Thus, for the very same trajectory the intruder experiences a larger drag force while it is moving slower.

For the interpretation of these results we turn to the interstitial air in the sand bed. Inside a porous medium the air cannot move freely, but it needs a certain amount of time to cover a particular distance, according to Darcy's law. While the ball is moving through the bed, sand in front of the ball is being compressed, as is also seen in chapter 2 of this thesis [18] and [19]. Air that was initially in-between the grains that now belong to this compressed region has no time to move out, and is therefore trapped in this area in front of the ball, as was concluded in chapter 4 of this thesis [20]. When the intruder moves at a very low speed, air has ample time to move out of the sand in front of the ball into the rest of the bed. On the other hand, when the ball is moving at a higher velocity, air has no time to diffuse out, effectively being trapped in front of the ball. It seems like trapped air is a key factor in the drag reduction measured for higher velocities. An obvious way to check this mechanism is to repeat the experiments without air, which is done in the next section.

7.5 Low ambient pressure

If it is really the presence of air that reduces the drag above a certain velocity, the drag constant κ_D should not change when varying the velocity, if there is no air present in the system. Therefore, to test this hypothesis in the second set of experiments the intruder is pushed to the same constant depth with various intruder velocities at 5 different reduced values for the ambient pressure: 800 mbar, 600 mbar, 400 mbar, 200 mbar and 100 mbar. The result of these experiments are given in figure 7.3a. We observe similar behavior as described in the previous section. The drag force constant κ_D is high for very low speeds and decreases

towards a constant above a velocity of about 150 mm/s. The lower the ambient pressure, the less extreme the difference becomes: At higher velocities the drag force is reduced, but by a lesser amount than we found at 1 bar. At the lowest ambient air pressure (100 mbar) we measure almost no change in the drag force with velocity. Most significantly, at low penetration velocities the measured drag force constant κ_D coincide for all ambient pressures P_0. This is consistent with our interpretation that this is the quasi-static regime where air does not influence the drag on the object.

Finally, the relation between the drag force constant and the ambient pressure is measured at a constant velocity (200 mm/s), which has been chosen such that we are in the regime where the drag reduction has saturated. The results are given in figure 7.3b and indicate two distinct regimes. In both regimes the drag decreases with increasing pressure, and we measure a significant drag reduction due to the influence of interstitial air.

7.6 Conclusion

In conclusion, in this work we measured the drag force exerted on a ball while it is being pushed into a sand bed. In these experiments the influence of air on the behavior of the sand bed is very prominent and leads to drag reduction: The force that is needed to push the ball into the sand is a combination of the force needed to push away the sand grains and a force due to the air pressure buildup in the bed in front of the ball.

Although at a first glance it may seem that the pressurized air could only increase the force, the opposite turns out to be true. When the velocity of the intruder is very low, no air pressure is accumulated in front of the ball since it has enough time to diffuse out of the way. As soon as the intruder moves faster, air is being trapped in front of the ball and we observe a surprising drag reduction: The total measured drag force goes down. Reducing the ambient air pressure we observe that the *drag reduction* becomes less pronounced, and completely disappears for $P_0 = 100$ mbar.

Two possible explanations for this observation come from the work of Caballero *et al.* [2] and Royer *et al.* [3]. The first of the two hypotheses a local fluidization mechanism in front of the ball caused by the trapped air. If the air pressure just in front of the ball is increased enough it will be able to locally fluidize the sand. This fluidization will reduce the local packing fraction and therefore reduce the drag from the sand grains on the intruder. Royer *et al.* predict a layer of compressed air in front of the ball, cushioning the ball and reducing the effective

drag. Both mechanisms disappear when there is no interstitial air, so the drag reduction is only present when there is interstitial air.

References

[1] R. Clement, S. C. du Pont, M. Ould-Hamouda, D. Duveau, and S. Douady, *Penetration and blown air effect in granular media*, Phys. Rev. Lett. **106**, 098001 (2011).

[2] G. Caballero, R. Bergmann, D. van der Meer, A. Prosperetti, and D. Lohse, *Role of air in granular jet formation*, Phys. Rev. Lett. **99**, 018001 (2007).

[3] J. R. Royer, E. I. Corwin, P. J. Eng, and H. M. Jaeger, *Gas-mediated impact dynamics in fine-grained granular materials*, Phys. Rev. Lett. **99**, 038003 (2007).

[4] D. I. Goldman and P. Umbanhowar, *Scaling and dynamics of sphere and disk impact into granular media*, Phys. Rev. E **77**, 021308 (2008).

[5] S. Joubaud, T. Homan, and D. van der Meer, *Force measurements during impact with an instrumented particle*, chapter 6 of this thesis (2013).

[6] J. Uehara, M. Ambroso, R. Ojha, and D. Durian, *Low-speed impact craters in loose granular media*, Phys. Rev. Lett. **91**, 149902 (2003).

[7] D. Lohse, R. Rauhe, R. Bergmann, and D. van der Meer, *Creating a dry variety of quicksand*, Nature **432**, 689 (2004).

[8] H. Katsuragi and D. J. Durian, *Unified force law for granular impact cratering*, Nat. Phys. **3**, 420 (2007).

[9] P. Umbanhowar and D. I. Goldman, *Granular impact and the critical packing state*, Phys. Rev. E **82**, 010301 (2010).

[10] H. Katsuragi and D. J. Durian, *Drag force scaling for penetration into granular media*, Phys. Rev. E **87**, 052208 (2013).

[11] Y. F. F. Guillard and O. Pouliquen, *Depth-independent drag force induced by stirring in granular media*, Phys. Rev. Lett. **110**, 138303 (2013).

[12] M. Stone, D. Bernstein, R. Barry, M. Pelc, Y. Tsui, and P. Schiffer, *Stress propagation: Getting to the bottom of a granular medium - A surprising*

resistance would be put up by sand grains hiding a buried treasure chest, Nature **427**, 503 (2004).

[13] M. Stone, R. Barry, D. Bernstein, M. Pelc, Y. Tsui, and P. Schiffer, *Local jamming via penetration of a granular medium*, Phys. Rev. E **70**, 041301 (2004).

[14] M. Schroter, S. Nagle, C. Radin, and H. L. Swinney, *Phase transition in a static granular system*, Eur. Phys. Lett. **78**, 44004 (2007).

[15] G. Tardos, M. Khan, and D. Schaeffer, *Forces on a slowly rotating, rough cylinder in a Couette device containing a dry, frictional powder*, Phys. Fluids **10**, 335 (1998).

[16] J. Socolar, D. Schaeffer, and P. Claudin, *Directed force chain networks and stress response in static granular materials*, Eur. Phys. J. E **7**, 353 (2002).

[17] S. von Kann, S. Joubaud, G. A. Caballero-Robledo, D. Lohse, and D. van der Meer, *Effect of finite container size on granular jet formation*, Phys. Rev. E **81**, 041306 (2010).

[18] T. Homan, R. Mudde, D. Lohse, and D. van der Meer, *High-speed X-ray imaging of a ball impacting on loose sand*, chapter 2 of this thesis (2013).

[19] J. R. Royer, B. Conyers, E. I. Corwin, P. J. Eng, and H. M. Jaeger, *The role of interstitial gas in determining the impact response of granular beds*, Eur. Phys. Lett. **93**, 28008 (2011).

[20] T. Homan, S. Joubaud, D. Lohse, and D. van der Meer, *Air entrapment during the impact of a ball on sand*, chapter 4 of this thesis (2013).

8 Conclusions and Outlook

When a ball impacts on a very loose bed of sand it penetrates the sand and stops several ball diameters below the surface. The final depth depends on the drag the ball experiences during the penetration and this is found to depend on the presence of air. If air is present in-between the sand grains the drag is lowered compared to the case where no interstitial air is present. In this thesis we describe both experimental and theoretical work to investigate this air influence in more detail.

8.1 Conclusions

In chapter 2 we studied the granular impact experiment using a high-speed X-ray setup. Because of the reproducibility of the experiment, several measurements to image the sand at different heights could be stitched together to form a complete reconstruction of the cavity formed behind the penetrating ball. The dynamics of this cavity inside the bed shows a large resemblance to impacts in water, of which we already knew that the events above the surface were very similar. The rising air bubble that is detached after the cavity has collapsed is, in contrast to the experiment at earlier times, not very reproducible. Measuring the shape using only one measurement height and the bubble velocity shows that it is rather oblate with a concave bottom, similar to bubbles that rise in continuously gas-fluidized beds.

In the last part of this chapter we focused on the density of the sand bed. During the whole impact experiment the sand is found to compactify: From an initially very loose bed the surface level drops several millimeters, leading to an increase in the bed density, and the distribution of the compaction depends on the impact events. We find a compacted front traveling in front of the ball with a decreasing density as a function of the distance from the ball. A strong compression is found below and next to the ball indicating that sand is pushed away while it is moving down. The collapsing cavity creates a second very compacted region around the pinch-off height, but at later times the rising air bubble will rearrange the sand in its path resulting in region with a relatively loose center and compressed sides.

To be able to more precisely study the effect of air during the compaction of the sand bed we start with a simpler geometry. In chapter 3 a metal ball hits the sidewall of the container which uniformly compactifies the sand bed and the resulting pressure differences above and below the bed are measured. The pressure above the bed decreases immediately due to the increase in volume above the bed and the pressure inside the sand must therefore increase. The collapse of the sand bed (measured with a high-speed camera) happens so fast that air is trapped inside the pores of the granular material and is not able to flow out of the bed instantly. Due to the formation of a pressure difference inside the setup air will start to flow out of the sand into the volumes above and below the bed. This temporarily increases the pressure below the bed, and eventually all the air is transported through the bed into the upper container and the pressure inside the setup is equal again. A one-dimensional diffusion model based on Darcy's law is used to describe the airflow in the container after the formation of the initial pressure difference. Starting from a uniform distribution of excess air inside the bed due to a homogeneous bed collapse, where all the air that was originally in the bed stays in the bed, a solution is calculated numerically and the pressure above and below the bed are found, to be able to compare the model to the experiments. From the theory a way to non-dimensionalize the data for experiments with different shock strengths and at different ambient pressures is found, which collapses all the experimental data and the theoretical model onto one master curve.

Similar measurements of the pressure above and below the sand are performed during the impact of a ball on the sand bed, which are described in chapter 4. The shape of the pressure curve above the bed has some very specific characteristics which we were able to relate to the events that take place below the surface. While the ball impacts the sand bed and the cavity behind the ball is formed, the pressure in the top of the container decreases. This happens when air is being trapped inside the sand by the moving ball and the volume above the bed expands due to

the formation of the cavity. Air is only trapped in the sand when it is not able to flow out of the pores fast enough, a process that is limited by diffusion. After around 25 ms a plateau is visible in the signal, which can only exist when there is a balance between the amount of air that gets trapped in the sand, and air that flows out of the pressurized region in front of the ball. How fast the pressure decreases until the plateau is reached depends on the rate of change of the cavity volume and the ambient pressure. The amount of air that is trapped inside the bed by the ball in this initial impact stage increases with the dimensionless impact velocity (the Froude number) and decreases with increasing ambient pressure, whereas the trapped mass of air of course increases with pressure. After the plateau we see a sharp increase of the pressure above the bed when the cavity collapses and now also the pressure below the bed starts increasing. The signal from this point on is very similar to the signal found in chapter 3.

A comparison of these two different experiments is made in the next chapter, chapter 5. Here we characterize one of the crucial sand bed parameters, namely the permeability. The permeability indicates how easy air flows through a porous medium after a pressure difference is applied, described by Darcy's law, and is measured in this chapter in various ways. The first basic method is to apply a constant flow through the bed and measure the pressure difference. We found no clear dependance of the permeability on the amount of sand above a bed height of $H = \sqrt{A} = 14$ cm. The permeability is also inversely proportional to the relaxation time, thus the decay of a pressure difference over the bed gives a second opportunity to measure the permeability. This initial pressure difference is set up in three different ways. The first method starts from the equilibrium state of the constant flow measurements and the relaxation time of the pressure difference is found after the flow is stopped. The resulting permeability is very similar to one calculated before, indicating that the relaxation process is indeed governed by Darcy's law. The other two pressure differences are generated in the shock experiments (chapter 3) and the impact experiments (chapter 4). The permeabilities measured here are a bit lower, indicating that it is more difficult for air to move through the bed. This is consistent with the higher packing fraction of these experiments; the constant flow measurements are performed on a very loose bed, and the shock and impact beds have already been compactied when the permeability is measured. A slight dependence of the permeability on the amount of bed compaction is found, and, as expected, the permeability does not depend on the ambient pressure, in contrast to the relaxation time. A direct comparison between the shock and the impact experiments reveals that the initial pressure distribution in the bed is very different in the impact case. The uniform method

of perturbation of the shock experiments leads to a homogeneous initial pressure profile, and the very local perturbation method of the impacting ball also has a more inhomogeneous initial pressure distribution.

In chapter 6 measurements on an impacting ball are performed using an instrumented particle. With this particle the acceleration is measured in time revealing very complex dynamics (invisible in the position data): Very short strong forces that act on the ball during the impact events are clearly visible in the acceleration data, but do not survive when integrated twice to find the particle position, which is what has been measured up till now. For increasing impact speeds a strong deceleration is found as soon as the ball impacts the sand. A distinct acceleration peak indicates the moment the jet is formed. Just before the ball completely stops it is decelerated strongly, which may be due to compaction in front of the ball. The last oscillations in the signal are a sign of local rearrangements of the sand around the ball. This data is compared to various models that describe the forces experienced by the ball during the penetration. A linear dependence of the force on the depth is found for the low Froude number experiments, indicating a Coulomb type drag law. The drag force constant as a function of the ambient pressure is found to resemble a power law with exponent -1/2 . This is consistent with earlier measurements where the drag force was derived from a fit to the position data of the ball.

If the ball is attached to a linear motor it is possible to directly measure the drag experienced by the ball using a load cell. In chapter 7 we focussed on the air influence while pushing a ball through sand. The ball is accelerated above the bed and impacts with a constant velocity. Subsequently, there is a measurement zone in which no acceleration or deceleration takes place, after which the ball is stopped. We measure a linear increase in the force experienced by the ball as a function of the depth in the bed, and the slope of this line gives the drag force constant. If (at atmospheric pressure) the ball moves very slowly we are certain not to have an air pressure buildup in front of the ball, because air has ample time to move out of the way. Increasing the velocity surprisingly decreases the measured drag force constant until, above a certain threshold value, the drag force stays constant. A definitive answer to the influence of air in this problem can be obtained by repeating the experiment at low ambient pressures. The drag reduction for higher velocities decreases with decreasing ambient pressure, and eventually completely disappears below 200 mbar.

8.2 Outlook

In this thesis we gained insight into the places where air is present inside the sand and the pressure profiles that are set up by perturbing the sand bed for instance with an impacting ball. The direct influence of interstitial air on the drag experienced by the ball was measured both for low and high ambient pressure and for varying intruder velocity. However, a lot of unanswered questions regarding the influence of interstitial air on sand remain.

A first interest comes from the air bubble that is pinched off during the cavity collapse. This air bubble rises to the surface where it forms into an eruption. The shape of the bubble and the rising velocity are very similar to bubbles rising in continuously fluidized beds where the sand is transported along the perimeter of the bubble giving it a net upward velocity [1]. This bubble velocity depends on the velocity of the airflow creating the fluidized bed and thus there is a clear effect of the airflow on the grain dynamics. An interesting question is how and if a bubble would rise if no air was present in the pores, is air pressure inside the bubble necessary to keep the bubble's shape? To answer this, two type of measurements can be done, both involving X-ray imaging. If experiments as described in chapter 2 are repeated in a setup at reduced pressure, they would give a direct answer about the bubble shape. Luckily, only a few measurements where the bubble (if it exists) passes the measurement plane are necessary to describe the bubble shape, since a full reconstruction at low ambient pressure would not be feasible. The rising air bubble also has a large influence on the final packing state of the sand bed. This could be measured using an X-ray setup where the final bed density distribution is compared between high and low pressure experiments [2].

It would be very interesting to elaborate the simple but very elegant experiment from chapter 3, where a very loose sand bed is collapsed by a shock to the container wall. This chapter solely focusses on the pressure signal during one collapse cycle, but the bed can be compactified many times [3–9] before it reaches a steady state. Previous research shows that the bed density as a function of the number of shocks changes in a non-trivial way and performing such experiments in the presence of air and with the ability to measure the pressure above and below the bed would give a lot of insight into role of air in this process.

The linear motor setup from chapter 7 has the potential to generate a lot more interesting data than could be described in this thesis. The onset of the fluidization mechanism reducing the drag at high ambient pressures seems to depend on the ball diameter in a non-trivial way [10]. The velocity needed for a full advantage of the airflow around the ball is higher for smaller ball diameters, and the total

decrease in drag force that can be generated is less, counterintuitively leading to a higher drag on a smaller ball for similar conditions.

Lowering the packing fraction by blowing a small amount of air through the system or, in contrast, compacifing it with several shocks is experimentally a rather simple step. However, the dynamics that we can expect from such a bed is very interesting [11]. Reducing the drag by fluidizing the sand in front of the ball will be increasingly more difficult for more compacted beds, thus a higher intruder velocity is necessary for this mechanism to work, until at some bed density there is no drag reduction measured at all. At lower packing fractions we could go into a state similar to the state reached in [12] where there is no depth-dependent drag force, and comparisons to the force needed for penetration in water can be made.

In this regime we also know that multiple intruders interact, they repel and attract each other while they move down [13]. Would a part of this behavior disappear if the experiment was carried out under vacuum, indicating an influence of air in this problem and if so, how exactly would this look?

Until now in this thesis no attention has been given to the initial forces generated upon impact. From chapter 6 we know that there is a strong deceleration upon impact at higher impact velocities. And it is possible to further test the drag law that describes this initial phase best [14].

A last and very important open question lies in the connection between macroscopic and microscopic behavior [15–19]. In this thesis the measured quantities are macroscopic, whereas the influence of the air starts at the micro scale. From granular studies at the micro scale we know how important phenomena like force chains and jamming are in understanding the global behavior of a granular bed [20, 21]. The coupling between experiments at the two different scales is not trivial, which is why this is a point where computer simulations can make a huge difference. In the group of Kuipers *et al.* research is being done on the interplay between air and granular matter in fluidized beds [22–24]. Their code combines a hydrodynamic description of the interstitial fluid with the grain-grain interaction and is therefore capable of simulating what kind of effect changes on the micro scale have on the macro scale. Experiments that can be directly compared to these type of simulations are in preparation and will be executed in the near future. Then, in the simulations, the influence of air on the micro scale can be changed, and the resulting macro scale dynamics will teach us invaluable information about the influence of interstitial air.

The most valuable piece of information out of this thesis that can be applied directly in technology is the drag reduction. We found that the drag experienced by an object moving through a granular material greatly depends on the presence

of air. Because of this air influence also the velocity at which the intruder moves is important for the force that needs to be applied. A lower velocity can lead to a higher experienced drag, whereas a higher velocity can reduce this drag and reduce the total force needed to move the object through the granular matter. One can even think of help setting up or intensifying this mechanism by blowing air out of the nose of the intruder. A possible application is the drilling of holes in the earth for example for poles to stabilize houses or to bring down pipes for oil and gas recovery. A lower drag can make a huge difference in the amount of time and money these projects ask.

References

[1] J. Davidson and D. Harrison, *Fluidized Particles*, Cambridge University Press (1963).

[2] J. R. Royer, B. Conyers, E. I. Corwin, P. J. Eng, and H. M. Jaeger, *The role of interstitial gas in determining the impact response of granular beds*, Euro Phys. Lett. **93**, 28008 (2011).

[3] J. B. Knight, C. G. Fandrich, C. N. Lau, H. M. Jaeger, and S. R. Nagel, *Density relaxation in a vibrated granular material*, Phys. Rev. E **51**, 3957 (1995).

[4] E. Nowak, J. Knight, M. Povinelli, H. Jaeger, and S. Nagel, *Reversibility and irreversibility in the packing of vibrated granular material*, Powder Techn. **94**, 79 (1997).

[5] T. Boutreux and P. deGennes, *Compaction of granular mixtures: A free volume model*, Physica A **244**, 59 (1997).

[6] E. Ben-Naim, J. Knight, E. Nowak, H. Jaeger, and S. Nagel, *Slow relaxation in granular compaction*, Physica D **123**, 380 (1998).

[7] S. Linz and A. Dohle, *Minimal relaxation law for compaction of tapped granular matter*, Phys. Rev. E **60**, 5737 (1999).

[8] P. Richard, M. Nicodemi, R. Delannay, P. Ribiere, and D. Bideau, *Slow relaxation and compaction of granular systems*, Nat. Mater. **4**, 121 (2005).

[9] P. Ribiere, P. Philippe, P. Richard, R. Delannay, and D. Bideau, *Slow compaction of granular systems*, J. Phys. Condens. Matter **17**, S2743 (2005).

[10] A. H. Clark and R. P. Behringer, *Granular impact model as an energy-depth relation*, Euro Phys. Lett. **101**, 64001 (2013).

[11] J. O. Marston, J. P. K. Seville, Y.-V. Cheun, A. Ingram, S. P. Decent, and M. J. H. Simmons, *Effect of packing fraction on granular jetting from solid sphere entry into aerated and fluidized beds*, Phys. Fluids **20**, 023301 (2008).

[12] F. Pacheco-Vazquez, G. A. Caballero-Robledo, J. M. Solano-Altamirano, E. Altshuler, A. J. Batista-Leyva, and J. C. Ruiz-Suarez, *Infinite Penetration of a Projectile into a Granular Medium*, Phys. Rev. Lett. **106**, 218001 (2011).

[13] F. Pacheco-Vazquez and J. C. Ruiz-Suarez, *Cooperative dynamics in the penetration of a group of intruders in a granular medium*, Nat. Comm. **1**, 123 (2010).

[14] M. Ambroso, R. Kamien, and D. Durian, *Dynamics of shallow impact cratering*, Phys. Rev. E **72**, 041305 (2005).

[15] G. Ben-Dor, A. Dubinsky, and T. Elperin, *Some inverse problems in penetration mechanics*, Mech. Design Struct. Mach. **38**, 468 (2010).

[16] J. P. Borg, M. P. Morrissey, C. A. Perich, T. J. Vogler, and L. C. Chhabildas, *In situ velocity and stress characterization of a projectile penetrating a sand target: Experimental measurements and continuum simulations*, Int. J. Impact Eng. **51**, 23 (2013).

[17] A. V. Vooren, J. Borg, H. Sandusky, and J. Felts, *Sand Penetration: A Near Nose Investigation of a Sand Penetration Event*, Proc. Eng. **58**, 601 (2013).

[18] K. N. Nordstrom, M. H. E. Lim, and W. Losert, *Granular dynamics during impact*, submitted to Phys. Rev. Lett. (2013).

[19] L. Kondic, X. Fang, W. Losert, C. S. O'Hern, and R. P. Behringer, *Microstructure evolution during impact on granular matter*, Phys. Rev. E **85**, 011305 (2012).

[20] B. Chakraborty and B. Behringer, *Jamming of Granular Matter*, Encyclopedia of Complexity and Systems Science 4997 (2009).

[21] J. C. Ruiz-Suarez, *Penetration of projectiles into granular targets*, Rep. Prog. Phys. **76**, 066601 (2013).

[22] M. Van der Hoef, R. Beetstra, and J. Kuipers, *Lattice-Boltzmann simulations of low-Reynolds-number flow past mono- and bidisperse arrays of spheres: Results for the permeability and drag force*, J. Fluid Mech. **528**, 233 (2005).

[23] S. Sarkar, M. A. van der Hoef, and J. A. M. Kuipers, *Fluid-particle interaction from lattice Boltzmann simulations for flow through polydisperse random arrays of spheres*, Chem. Eng. Sci. **64**, 2683 (2009).

[24] S. H. L. Kriebitzsch, M. A. van der Hoef, and J. A. M. Kuipers, *Fully resolved simulation of a gas-fluidized bed: A critical test of DEM models*, Chem. Eng. Sci. **91**, 1 (2013).

Summary

The events that are visible above a very loose sand bed after the impact of a metal ball are very similar to the ones seen after impact on a deep water layer. Upon impact a splash is formed and some time later a jet shoots up out of the sand. The last visible event is a granular eruption. In chapter 2 of this thesis X-ray experiments visualize the events below the surface. After impact the ball penetrates the sand creating an air cavity behind it. The walls of the cavity start moving towards each other and when they touch a jet shoots up and an air bubble is entrained, the bubble rises to the surface where it causes the eruption. Both the shape of the bubble and the cavity dynamics are very similar to those in continuously fluidized beds and water. The setup also allows for measurements of minute changes in the packing fraction, from which we learn that the sand in front and to the sides of the ball is compactified while the ball moves down. Subsequently, the collapse of the cavity accounts for a strongly compactified region whereas the rising bubble deposits the sand in a relatively loose fashion.

Inside the bed air can be clustered in cavities or bubbles as happens during the impact experiments, but air is also always present in-between the grains. What happens with the interstitial air when the sand is compactified? In the experiments described in chapter 3 the whole sand bed is made to collapse using a shock against the wall of the container. This process is so fast that air has not enough time to diffuse out of the bed and is therefore pressurized inside this compactified region. The amount the bed collapses depends on the shock strength, and interestingly, also on the ambient pressure: For lower air pressures in the container the bed collapses less, indicating that air has a lubricating effect on the friction between the grains. The pressure differences that originate from the collapse relax to zero in accordance with Darcy's law and the whole process is well described by a one-dimensional diffusion model.

The pressure differences that occur in the setup during an impact experiment are, just as in the shock experiments, for a large part caused by a compactifying bed. Only this time the compactification is due to the violent collapse of the cavity (see chapter 4). However, already before the entire bed collapses the pressure

above the bed is decreasing, which is attributed to air that is trapped in the compressed region around the ball. The existence of a phase in which the ball is still moving but no pressure changes are measured, points to an equilibrium between air being trapped and air flowing from this region out of the bed. This process is limited by the diffusion time of air in the granular medium. The maximum amount of air that is trapped in the bed depends both on the impact velocity of the ball and on the ambient pressure.

The rate at which air flows through a porous medium due to a pressure difference is governed by the permeability of the medium, which is described in chapter 5 for a very loose sand bed. The permeability is obtained in two ways: First by applying a constant flow and measuring the resulting pressure difference, and secondly by measuring the relaxation time of an initial pressure difference. For the relaxation time measurements three different initial pressure profiles are used and we found that the permeability depends on the porosity of the bed: A more compactified bed gives a lower value for the permeability. The exact shape of the measured pressure signal depends on the initial pressure distribution, *i.e.*, the signal of a uniform bed collapse is different than the pressure changes during the inhomogeneous impact events.

The drag that is experienced by the ball while it moves through the sand slows it down and will eventually stop it at a certain depth below the surface. In the experiments in chapter 6 sensors inside the impacting object measure the acceleration of the ball as a function of time, which is proportional to the drag force. This signal shows details, *e.g.*, at the moment of impact and at the time of the jet formation, that would not be measurable from the position data, because these events change the motion of the ball only for a very short time. The amount of deceleration depends on the impact velocity and the ambient pressure, at lower pressures the deceleration is clearly higher, stopping the ball higher in the bed and pointing towards a larger drag force at lower ambient pressures.

To directly measure the drag force the ball is attached via a load cell to a linear motor (chapter 7). The force that needs to be applied increases linearly with depth. However, its magnitude depends strongly on the intruder velocity: For low velocities a *larger* force is needed to push the ball into the sand. This can be explained by the air that is trapped in the compactified region in front of the ball at higher velocities, which locally increases the air pressure and reduces the drag experienced by the ball. Comparing quasi-static experiments, where air has ample time to move out of the way, with experiments done at reduced pressures indeed show the same value for the measured force, indicating that trapped air causes drag reduction.

Samenvatting

Wanneer je een metalen bal op het strand laat vallen zal er weinig gebeuren. Misschien dat er wat zandkorrels opspatten, maar de bal blijft gewoon boven op het zand liggen. Als het zand nu zo geprepareerd wordt dat er heel veel lucht tussen de zandkorrels zit, dan zijn de gevolgen van de inslag heel anders. Zo'n luchtige pakking kan worden gemaakt maken door van onder lucht door het zand te blazen, dit vergroot het totale volume van het bed en er ontstaan grote luchtbellen die door het bed omhoog bewegen. Als deze luchtstroom heel langzaam uit wordt gezet eindigen de deeltjes in een pakking met zo veel mogelijk lucht tussen de deeltjes, kortom, een zeer los zandbed.

Op het moment van inslag spat een hoeveelheid zand de lucht in de vorm van een kroon. Vervolgens zinkt de bal weg in het zand en verdwijnt uit het zicht. De volgende direct waarneembare gebeurtenis is een straal zand die met hoge snelheid uit het bed omhoog schiet en een hoogte haalt die zelfs hoger kan zijn dan die waarvan de bal is losgelaten. Het laatste zichtbare voorval is een kleine uitbarsting waarbij zand omhoog stuift. De gevolgen van de inslag op zand heeft veel overeenkomsten met die van de inslag van een object op water. Bij diepe penetratie vormt zich ook hier een kroon en schiet er een straal water omhoog. Het grote voordeel van water is dat je ook kunt zien wat er onder het wateroppervlak gebeurd.

Om erachter te komen of naast de gebeurtenissen boven het zand ook de onzichtbare gebeurtenissen onder het zand op die van water lijken, kijken we in hoofdstuk 2 van dit proefschrift door het zand heen met röntgen straling. Per meting brengen we de luchtruimtes in één horizontale doorsnede in kaart. Om deze verschillende metingen aan elkaar te kunnen plakken moet het experiment erg reproduceerbaar zijn. In het eerste deel van de penetratie is dit het geval en kunnen we een reconstructie maken van waar de lucht zich in het zandbed bevindt. De bal beweegt naar beneden door het bed en er vormt zich een luchtholte achter de bal. De wanden van deze holte bewegen naar elkaar toe en op het moment dat ze elkaar raken schiet er een straal zand omhoog uit het bed. De resterende holte, beneden de plek waar de luchtholte sloot, beweegt met de bal mee naar

beneden totdat de bal tot stilstand komt. Daar laat hij los en deze bel stijgt naar het zand oppervlak waar hij de kleine uitbarsting veroorzaakt. Het experiment is heel erg reproduceerbaar tot aan de vorming van de jet, tot hier kan de vorm van de luchtholte worden gereconstrueerd en een directe vergelijking met de luchtholte gevormd in water laat zien dat de dynamica erg op elkaar lijkt. Het stijgen van de bel is minder reproduceerbaar en om meer te leren over deze bel moeten we een andere analyse methode toepassen. Hier kijken we hoe één bel langs een bepaalde meethoogte komt en we bepalen de vorm aan de hand van de gemeten snelheid van de bel. Het blijkt dat de vorm van de bel erg lijkt op de vorm van bellen in een continu gefluïdiseerd bed en de bel stijgt dan waarschijnlijk ook met hetzelfde mechanisme: Zand wordt langs de wand van de bel van boven naar beneden getransporteerd wat de bel een netto opwaartse snelheid geeft. Als laatste hebben we in dit hoofdstuk gekeken naar de pakkingsdichtheid van het zand tijdens de voorvallen in het bed. Wanneer de bal door het bed beweegt wordt het zand onder en naast de bal gecomprimeerd. Op het moment dat de holte sluit is ook daar een sterke samendrukking van het zand te zien. Tijdens het stijgen van de bel, de laatste gebeurtenis in het bed, wordt het zand heel losjes gedeponeerd onderaan de bel. Dit zorgt voor een relatief ongecomprimeerde zone in het pad van de bel.

Nu we weten dat de lucht zich zowel tussen de zandkorrels als in luchtholtes in het bed bevindt is het interessant om wat meer naar de invloed van lucht in het bed te kijken. Er wordt gedacht dat de aanwezige lucht verantwoordelijk is voor de verrassende diepte die de bal haalt na de inslag op het zandbed en dus dat de lucht in het zand een grote invloed heeft op de dynamica. In hoofdstuk 3 onderzoeken we de reactie van een luchtig zand bed op een schok. Om zeer gecontroleerd zo'n schok te kunnen geven is er een metalen bal gemonteerd aan een slinger die van variabele afstand tegen de container met zand aan botst. We meten de hoogte van het bed voor en na de botsing hetgeen ons een maat geeft voor de instorting van het bed. Hoe groter de afstand waarvan we de bal laten slingeren hoe groter de schok en hoe groter het resulterende bedhoogteverschil. Dit experiment is ook uitgevoerd bij lage luchtdrukken in de container, waarbij er (wat massa betreft) minder lucht tussen de zandkorrels zit. We zien dat hoe minder lucht er in de bak aanwezig is voor het experiment (hoe lager de druk), hoe minder ver het bed instort. Deze verassende uitkomst kan worden verklaard als de aanwezigheid van lucht de wrijving tussen twee zanddeeltjes verlaagt: De lucht zorgt er dan voor dat de snelheid van de deeltjes in het instortende bed minder afneemt tijdens botsingen met andere deeltjes waardoor het bed verder in kan storten. Dit effect verdwijnt als je bijna alle lucht uit de opstelling weghaalt. We meten ook de luchtdrukverandering boven en onder het bed tijdens het instorten

van het zandbed. Boven het bed neemt de druk sterk af op het moment dat het bed instort, wat komt doordat het volume boven het bed plotseling toeneemt, onder het bed verandert er in eerste instantie niets. De lucht die oorspronkelijk in het zandbed zat blijft ook na de instorting in het bed, omdat het instorten zo snel gaat dat de lucht niet de tijd heeft om uit het bed te ontsnappen. Dit resulteert in een druktoename in het bed en de drukverschillen tussen het bed en de ruimtes boven en onder het bed zorgen ervoor dat er lucht naar boven en onder uit het bed stroomt. De druk onder het bed neemt hierdoor tijdelijk toe, maar uiteindelijk zal alle lucht door het bed naar het volume erboven stromen zodat de druk overal weer gelijk is. Het maximale drukverschil boven en onder het bed is evenredig met het bedhoogteverschil en met de luchtdruk in de bak voor de schok; een groter bedhoogteverschil of een hogere druk leidt tot een hoger maximum in de druksignalen. Een dimensieloos theoretisch model, dat gebaseerd is op een eendimensionale diffusievergelijking afkomstig van de wet van Darcy, voorspelt het verloop van de druksignalen. Als beginconditie gaan we er vanuit dat een uniforme instorting van het bed een uniforme druktoename in het bed veroorzaakt. Als het lek door de druksensoren mee wordt genomen geeft het model een zeer goede overeenkomst met de experimenten en kunnen we dus concluderen dat het drukprofiel in het begin en de stromingsbeschrijving uit de diffusievergelijking het probleem erg goed beschrijven.

Tijdens de inslag van de bal op zand neemt de bedhoogte af en wordt het zand samengedrukt. Dit moet ook een drukverschil over het zandbed veroorzaken en dus is het interessant om de druk boven en onder het bed te meten tijdens een inslag experiment (hoofdstuk 4). Globaal lijken de signalen erg veel op de resultaten uit het schok experiment en het verschil zit in de manier waarop de druk boven het bed veranderd: De druk neemt eerst af en blijft na ongeveer 25 ms even constant voordat hij snel daalt op het moment dat de holte sluit (na ongeveer 50 ms). De bal stopt na ongeveer 120 ms met bewegen en dus zijn al deze karakteristieke signaaleigenschappen gemeten terwijl de bal door het zand beweegt. Uit hoofdstuk 2 weten we dat het zand rond de bal gecomprimeerd wordt en uit hoofdstuk 3 blijkt dat er lucht gevangen kan blijven zitten tijdens het samendrukken van het zand. De eerste druktoename is dus waarschijnlijk veroorzaakt doordat de luchtholte achter de bal het volume boven het bed vergroot en daardoor de druk verlaagd terwijl er lucht in het samengedrukte zand voor de bal zit opgesloten. Dat de druk constant wordt en niet blijft toenemen totdat de luchtholte niet meer groter wordt is alleen te verklaren met een evenwicht tussen de hoeveel lucht die in het bed wordt opgesloten en de hoeveel lucht die uit het bed in de ruimte erboven kan stromen. De tijd die de opgesloten lucht erover doet om

langs de bal in de luchtholte erachter te stromen is volgens de diffusietijd ongeveer gelijk aan 25 ms, wat dus overeenkomt met de start van het constante druk signaal. De maximale hoeveelheid lucht die wordt opgesloten in het bed (evenredig met de waarde van de druk in het constante gedeelte) is gemeten voor verschillende inslag snelheden van de bal en voor verschillende luchtdrukken in de container aan het begin van het experiment. Hoe hoger de inslag snelheid hoe groter het volume lucht dat is opgesloten, dit komt doordat bij deze hogere snelheden de luchtholte groter is op het moment dat het evenwicht met de diffusie van lucht is opgezet. Bij lagere drukken wordt er een groter volume lucht opgesloten dan bij hogere drukken, de massa van het totaal ingesloten volume is natuurlijk wel kleiner bij lage drukken. De luchtholte sluit na ongeveer 50 ms, deze sluiting is zo hevig dat daarbij het hele bed instort en de druk boven het bed dus nog lager wordt. Dit wordt bevestigd doordat de druk onder het bed pas begint toe te nemen vanaf deze 50 ms, lucht zou seconden nodig hebben om door het hele bed te stromen, dus het lijkt erop dat de instorting van het bed bij de sluiting van de luchtholte een globaal effect is waarbij ook de lucht dicht bij de bodem een hogere druk krijgt en graag het bed uit stroomt naar het volume onder het bed.

In het volgende hoofdstuk (hoofdstuk 5) vergelijken we de manier waarop het opgebouwde drukverschil weer afneemt na metingen met een constante luchtstroming door het bed en na de metingen uit hoofdstuk 3 en 4. De relatie tussen het drukverschil over een poreus materiaal van een bepaalde dikte en de stroomsnelheid van lucht (of een ander gas of vloeistof) door dit materiaal wordt beschreven door de wet van Darcy, en de belangrijke parameters zijn de porositeit en de permeabiliteit van het materiaal. In dit hoofdstuk is de permeabiliteit van ons zandbed bepaald aan de hand van constante luchtstroming metingen en het verval van een drukverschil in tijd. Bij de eerste set metingen laten we een constante hoeveelheid lucht door het bed stromen waarbij de stroomsnelheid zo laag is dat de zandkorrels hierdoor niet verplaatsen en het zandbed dus niet wordt verstoord. Vervolgens meten we de druk over het zandbed en gebruik makend van de wet van Darcy kunnen we de permeabiliteit van het zandbed berekenen. Een tweede methode om de permeabiliteit van ons zandbed te bepalen komt van de drukverandering over het bed nadat de luchtstroom is stopgezet: De druk neemt exponentieel af en de relaxatietijd is afhankelijk van hoe makkelijk de lucht door het bed kan stromen. De permeabiliteit berekend uit relaxatie metingen na de schok en inslag metingen is wat lager dan bij de constante stroming meting, maar dit is logisch omdat het bed na een schok of een inslag wat is ingestort waardoor de porositeit lager is geworden: Het zandbed is meer samengedrukt en het is moeilijker voor de lucht om door het bed te stromen. Uit een vergelijking met het model uit

hoofdstuk 3 met verschillende beginvoorwaarden voor het drukprofiel blijkt dat de hoeveelheid extra lucht waarschijnlijk gelijkmatig over het bed verdeeld was na de schok. Vergelijkingen van het profiel van de schok en de inslag metingen laat duidelijk zien dat de lucht oorspronkelijk heel anders verdeeld zit: Bij het inslag experiment zijn veel locale gebeurtenissen en de lucht zit ook veel minder globaal verdeeld over het bed dan bij de schok metingen.

Een andere manier om meer te weten te komen over de processen in het bed is door meer informatie te verzamelen over het inslagobject. In plaats van de metalen bal gebruiken we in hoofdstuk 6 een bal waar drie versnellingsmeters in gemonteerd zijn. Hiermee kunnen we de exacte versnelling van de bal tijdens de beweging in het zand direct meten en daaruit afleiden welke krachten er op de bal worden uitgeoefend. Het voordeel van deze methode is dat het non-invasief is; er zit geen snoer of staaf aan de bal om het signaal door te vervoeren, en het zand rond de bal gedraagt zich dus hetzelfde als in de voorgaande experimenten. De vorm van het signaal hangt af van de inslagsnelheid en de omgevingsdruk, en we kunnen een paar karakteristieke elementen onderscheiden. De bal ondergaat een vrije val en wordt op het moment van inslag sterk maar kort afgeremd. Tijdens de beweging in het bed wordt de bal verder vertraagd en vlak voordat hij stil komt te staan wordt hij nog een keer sterk afgeremd. In het signaal is het moment dat de holte sluit duidelijk te zien als een korte versnelling van de bal, veroorzaakt door de impact van de zandstraal op de bal of door de druktoename in de holte als een gevolg van de sluiting. Hogere inslagsnelheden leiden vooral in het eerste deel van de beweging door het zand tot een grotere vertraging. Metingen bij verschillende omgevingsdrukken laten zien dat de vertraging van de bal in het zand aanmerkelijk groter is bij lagere druk, en de bal komt dan dus ook eerder tot stilstand. Het model van Katsuragi is gebruikt om het gemeten vernellingssignaal te beschrijven. Het voorspelt het globale gedrag van de versnelling goed, maar mist details zoals de sterke vertragingen aan het begin en eind van de beweging in het bed en de versnelling door de sluiting van de holte. Ondanks dit is de overeenkomst tussen het model en de positie van de bal (verkregen door de experimentele data tweemaal te integreren) perfect.

Het is duidelijk dat het meten van de versnelling meer details laat zien over de gebeurtenissen in het zand dan het meten van alleen de positie. In het laatste hoofdstuk (hoofdstuk 7) duwen we een bal met een lineaire motor met constante snelheid in het losse zand, en focussen we opnieuw op de invloed van de lucht tussen de zandkorrels. In deze experimenten zit de bal vast aan een staaf en in de staaf is een krachtsensor gemonteerd. Omdat er geen versnellingen of vertragingen plaatsvinden terwijl de bal door het zand beweegt komt alle gemeten kracht van de

weerstand van het bed op de bal. Voor niet al te hoge snelheden neemt de kracht die moet worden uitgeoefend op de bal om hem door het zand te duwen lineair toe met de diepte; vervolgens kan uit de helling de weerstandsconstante worden bepaald die we kunnen vergelijken voor de verschillende experimenten. Als we de snelheid waarmee de bal beweegt opvoeren zien we dat de kracht die we moeten uitoefenen verrassend afneemt, totdat hij boven een bepaalde snelheid constant blijft. Wanneer de bal heel erg langzaam door het zand wordt geduwd heeft de lucht tussen de korrels alle tijd om weg te stromen en zal dus geen invloed hebben op de weerstand die de bal ondervind. Zodra we sneller bewegen blijft er lucht opgesloten zitten in het zand dat voor de bal wordt samengedrukt en dit verlaagt de weerstand die de bal ondervind tijdens de beweging in het zand. Eenzelfde set experimenten is ook uitgevoerd bij lagere omgevingsdrukken. Het verschil in de weerstandsconstante tussen metingen bij hoge en lage snelheden neemt af en verdwijnt uiteindelijk voor lage drukken helemaal. De weerstandsvermindering bij hogere snelheden is dus duidelijk een effect van de lucht tussen de deeltjes en ontstaat doordat de lucht niet voldoende tijd heeft om weg te stromen uit het samengedrukte zand voor de bal.

Acknowledgements

I would not have been able to write this thesis without the help and support of many people and I would like to take this opportunity to thank them. During my internship in Denmark I received an email from Detlef in which he proposed that I would to stay in his group for my master project and PhD. This turned out to be a really nice and valuable time and I'm still very grateful to Detlef for the opportunity. Detlef, you've created an ideal environment composed of very skilled people in which doing research is as easy as it will ever be.

The topic of my PhD is granular matter, and obviously my project would be supervised by Devaraj. I'm happy that I worked with sand, both for the intriguing problems that the granular nature of the material generates and for the people I got to work with. Devaraj, you taught me a lot about all the aspects of doing research. You seem to have knowledge about everything and can help solve every problem that can be encountered in the lab, while doing data analysis, figuring out the right derivation of equations, or when trying to make sense of the results. Doing research is comprised of so many things and some parts turned out to be rather challenging. I really appreciate that you've been there for me for the past five years.

A part that I liked a lot about doing a PhD were the student projects and the teaching. I hope Jorrit, Carolien and Lieke enjoyed their OTNW project just as much as I liked mine in my first year and I enjoyed working with you. I want to thank Christa for doing her Bachelor assignment with me, I think you did an excellent job and I hope our paper (chapter 3 of this thesis) will be published soon. Teaching the working classes of *Advanced Fluid Mechanics* for two years was one of the best parts of my PhD. Both Devaraj and Jacco showed a different but excellent way of teaching the course, and I enjoyed working with them and Theo and Claas-Willem very much. Teaching is difficult and there is still a lot left to learn, but it is something I hope to keep doing in the future.

I know that there is a story going around that if you cannot find Bas he will probably be fixing something for Tess. This is kind of true and I want to thank Bas for all his hard work for me, especially with trying to get the new setup working

and let it run fully automatic. Gert-Wim and Martin, this setup would have never existed without you, thanks for building it and for helping with the tons of other questions I fired at you the past five years. Joanita, you are really one of the main reasons the group runs so smoothly and I want to thank you for your help.

I've worked in the Physics of Fluids group on a lot of occasions, first during the OTNW project, then for my bachelor assignment, a short stay for the course experimental techniques and eventually for my masters project and PhD. I have always enjoyed it here and this is of course because of the people, thanks everybody for the nice coffee breaks and lunches (indoors or outside by the pond). At PoF you can always find someone that is willing to help with anything, this is why we are a group and not just a bunch of people working in adjoining labs. Working with sand in stead of water puts you in the somewhat different "granular people" category, and it was a pleasure to share the status and the lab with Stefan, Ceyda, Rianne and Loreto. Sylvain, we worked together before you moved to Lyon and we stayed in contact after that: Finishing the papers we wrote together and doing the very nice experiments for chapter 6. You have taught me a lot, and you are such a nice person to work with, I would like to thank you. I'm also very happy that I always had nice people around me in the office: Jeroen, Wim, James, Kristjan, Mark-Jan, Antonin, and Sander, next to the small talk it is nice to know that there is always someone around if you need input on more important things like for instance color schemes. Office 251, Hanneke and Oscar, I know I have been dropping in quite a bit, but it is hard not stop in an office full of nice people on your way to the printer.

Besides work there is a lot going on in a persons life, and therefore there are so many more people that were important to me the past years. Juggling is an amazing hobby, not just because the juggling itself is fun, but also because it comes with a huge group of friends. Thanks everybody for traveling with me to juggling festivals and for all the passing that we did. Menno, thanks for the nice morning passing sessions, I'm glad we both stayed in Enschede after our studies. Willemein, you have been such a good friend to me the past years and I want to thank you for standing next to me during my defense.

The past four years I've spent a lot of time playing volleyball, and all of this time was definitely worth it. When I started I had no idea that joining a team meant that you gained around ten friends instantly. Harambee dames 5 2009-2010, dames 2 2010-2011, dames 2 2011-2012, and dames 2 2012-2013, I want to thank you for all the nice trainings, matches, eating cake and team evenings. I love indoor volleyball, but nothing can top standing with your feet in the sand. Thanks Nienke, Maarten and Stefan for playing beachvolleyball with

me, especially for the “first beach of the season”. Carmen, I want to thank you for being my beachvolleyball partner, together we played better than I ever imagined I could. I also want to thank you for every time we had a cup of tea, worked on the beachprogram, and all the other times we spent together, it was really very special to me.

Harry, Carolien and Casper, I want to thank you for welcoming me in your family and I very much enjoyed our holidays together and the holiday feeling I have every time I visit Zoelen.

Mom and Dad I loved living so close to you: Having diner on saturday and still having you around for all the questions and doubts that I had. Knowing how proud you are of me is a good reason to keep working even when it is hard. Thanks for everything.

Lotte, having a sister means that someone will always be there for you, I don’t have to pretend to be better than I am, because you already know me and you will always be my sister. I loved seeing you around campus, in the sports center just bumping into each other and of course at home in the weekends. But even now you’ve been away for most of the year, we still talk a lot and share everything and I’m glad that you will be home and standing next to me during my defense.

Joost, I often think back of the moment that I chose the “bestuursbengels” doegroep during our introduction period, would we have ever met if I had joined another one? I’d like to think that we did, because I cannot image life without you. Being with you is so easy, together life is just better in every way. You’ve meant so much to me during our studies and during the PhD, I know I’m a stresskip sometimes, but it would have been much worse without you. If work is difficult or hard it is very important that someone is there for you, and you are always there when I need you. I don’t like changes and I know life after the defense will be entirely different, but with you I even look forward to moving away to wherever we are going to end up, together.

Tess Homan
August 2013

About the author

Tess Homan was born on October 4th, 1986 in Oldenzaal, and lived most of her youth in Hengelo. There she attended the first few years of high school at the OSG Montessori and graduated from the OSG Bataafse kamp in 2004. In the same year she started to study Applied Physics at the University of Twente in Enschede, including a minor in Human Movement Sciences at the Vrije Universiteit in Amsterdam. In 2008 she spent time in Denmark for an internship at the Danish Technical University in the group of Prof. Tomas Bohr working on surface shapes in a rotating tank, and she did an internship at the University of Maryland in the United States of America studying the movement of the single cellular organism Dictyostelium in the group of Prof. Wolfgang Losert. In 2009 she graduated cum laude on the airflow through a granular bed and the impact of a ball on soft sand at the Physics of Fluids group. She continued as a PhD student in the same group with Prof. Detlef Lohse and Prof. Devaraj van der Meer.